COLLECTIVITY OF EXOTIC SILICON ISOTOPES

By

Andrew Ratkiewicz

A DISSERTATION

Submitted to
Michigan State University
in partial fulfillment of the requirements
for the degree of

DOCTOR OF PHILOSOPHY

Physics

2011

ABSTRACT

COLLECTIVITY OF EXOTIC SILICON ISOTOPES

By

Andrew Ratkiewicz

The determination of the strength of the electric quadrupole transition between the ground state and first excited state with spin-party $J^{\pi} = 2^{+}$ (the $B\left(E2; 0^{+} \rightarrow 2^{+}\right)$ value) in an even-even nucleus provides a measurement of the low-lying quadrupole collectivity. The $B(E2)$ values for the Z=14 nuclei ^{34,36,38,40,42}Si were measured via intermediate-energy Coulomb excitation at the National Superconducting Cyclotron Laboratory in East Lansing, Michigan.

The secondary beams were produced by the fragmentation of a ^{48}Ca primary beam guided onto a high-Z secondary target. De-excitation γ-rays, indicative of the inelastic process, were detected with the high-efficiency scintillator array CAESAR, located around the secondary target position of the S800 Spectrograph, in coincidence with scattered particles tracked on an event-by-event basis in the Spectrograph. The results comprise the first measurements of the quadrupole collectivity of ^{40,42}Si.

The measured $B(E2)$ values are compared to large-scale shell model calculations and provide insight into the evolution of shell structure and deformation in this region.

my teachers

ACKNOWLEDGMENTS

I owe an immense debt to the people who have been kind enough to mentor me in graduate school, to no one more than Dr. Alexandra Gade. Dr. Gade is the best advisor I could have had. She steered my professional development by sending me to schools and conferences and by introducing me to her colleagues. She guided me through the work discussed in this dissertation, always allowing me to learn by doing, while holding me to a high standard. I am very grateful for the support Dr. Gade gave me while I was searching for a postdoctoral position; I would have been lost without her advice and letters of recommendation. Dr. Gade is an exceptional scientist and it has been my privilege to learn from her for the past five years.

Dr. Dirk Weisshaar is perhaps best described as my *Doctoronkel*[1]. I have yet to find a topic in experimental nuclear physics about which he does not seem to know everything and can explain concisely. Dr. Weisshaar played a critical role in my graduate education and I will always be grateful to have had the benefit of his experience. Dr. Gade and Dr. Weisshaar read this dissertation several times and it is much better for their comments.

When I began graduate school I worked for Dr. Thomas Glasmacher, whose idea it was to measure the quadrupole collectivity of ^{40}Si. When Dr. Glasmacher became busy planning FRIB, Dr. Gade was kind enough to take me on as her student. I only worked for Dr. Glasmacher for about two years, but I have never had a conversation with him in which I did not learn something.

I would like to thank the other members of my guidance committee, Drs. Carlo Piermarocchi, Wayne Repko, first Alex Brown and later Scott Pratt for the conversations we

[1] Dr. Mathias Steiner, *private communication* (2011).

had about my academic progress and their input on my research over the last several years.

Dr. Geoffrey Grinyer was responsible for assembling the electronics for CAESAR. I am grateful for his assistance in conducting the experiments discussed in this work, as well as for his advice on the analysis and my subsequent career plans.

Dr. Daniel Bazin tuned the S800 Spectrograph for each of the secondary beams used in my experiments. During the experiments he worked very long hours to ensure their success and after the experiments he answered all of my questions about the Spectrograph. I'm grateful to have had the benefit of his expertise for the analysis of these experiments. It is a pleasure to work with Dr. Bazin because he is an excellent scientist and is continually cheerful, even when called at three in the morning.

Dr. Jorge Pereira led the development of the secondary beams for my experiments. This was a technically challenging task, first because the experiments required five different secondary beams and second because the rate of ^{42}Si was very low. It is thanks to the excellent work done by Dr. Pereira and by the rest of the A1900 group (Drs. Tom Ginter, Thomas Baumann, Marc Hausmann, Mauricio Portillo, and Andreas Stoltz) that these measurement were possible.

Dr. David Morrissey was kind enough to take an interest in my progress and to give me career advice. This means a great deal to me; Dr. Morrissey is a role model for me because he has a pragmatic approach to physics and he is quite good at it.

Dr. Mathias Steiner was the interface between the operations department and my experiments. He made sure that problems with the beams were fixed in short order and that we ran at the high intensities necessary to perform the experiments successfully. On a personal note, Dr. Steiner taught me the best card game of ever (skat), showed me the best canoing in Michigan, as well as giving me practical advice on how the world works (usually I nodded

and pretended to already know it — if he ever reads this acknowledgment he will say that this explains a lot). Dr. Steiner has been a good friend and I will miss him.

The Operations group at NSCL provided essential support for my experiments. I am grateful for the effort Jon Bonofiglio, Randy Rencsok, Shannon Krause, Tom Beal, Andrew Loucks, Gene Battin, Ken Galbraith, David Schaub, Genevieve West, Dallas Cole, and Larry Tobos made to make the experiments discussed in this work a success.

My colleagues helped me survive graduate school, especially Rhiannon Meharchand, David Miller, and Philip Voss (both of whom also read my dissertation). Without Rhiannon and Phil the first years would have been much more difficult. Karl Smith, Krista Meierbachtol, Travis Baugher, Ragnar Stroberg, Sean McDaniel, Jill Berryman, and Jenna Smith kept me sane.

I would like to thank the past and current members of the Gamma Group for their friendship and contribution to these projects: Jon Cook, Kyle Siwek, Chris Campbell, Sean McDaniel, Travis Baugher (who wrote the GEANT4 simulations used in this work), Ragnar Stroberg, and Aimee Shore are my friends, as well as a fantastic group of people to work with.

My roommates for the past three years, Josh and Sara Vredevoogd, made the hard parts so much easier. I will remember the good times and dinners we shared for the rest of my life. I will miss Josh and Sara.

The people who got together Sunday made Mondays better: Bryan, Christina, Eric, Stacy, Cris, Anna, Randy, Steve, Arnau, Jeff, Dean, Katie, Alisha, and Steff — thanks for your friendship, it has meant a lot to me. Rico, as per usual, you are correct: I am a standard.

I would like to thank the NSCL cycling group (too many people to list) for two and a

half memorable DALMACs. I will miss preparing for DALMAC every summer and riding with you all.

I would like to thank the Council of Graduate Students, especially the members of the Peace and Reconciliation Committee: Shannon, Amanda, Shannon Demlow, Matt, Adam, and Stefan for helping me learn how academic government can work.

I would like to thank the other Wagon Brothers for their support during a particularly difficult year.

Finally, I would like to thank the professors who mentored me during my undergraduate career. These people, especially Drs. Ann Grens, Jerry Hinnefeld, Ilan Levine, Monica Lynker, Rolf Schimmrigk, Henry Scott, and Lyle Zynda taught me that, no matter how much you know, there are still things worth learning.

This section was difficult to write, because I have spent the happiest years of my life so far at NSCL and in Lansing. This is completely due to the people here (I know I have left some out), to whom I cannot do justice in three pages or so. I do not feel that I am being nostalgic; graduate school was very hard. However, every day I got to come to the lab to work on interesting problems with very smart people who were excited about finding solutions. It was a wonderful experience.

Thank you.

TABLE OF CONTENTS

LIST OF TABLES

LIST OF FIGURES

Chapter 1

Introduction

An atomic nucleus is a many-body Fermionic quantum system made of neutrons and protons (called *nucleons*). Nuclear systems are extremely small, with typical radii on the order of 10^{-14} meters. Protons have a positive electric charge and interact with one another through the Coulomb force, which repels protons from one another and decreases in strength with $1/r^2$, where r is the radial coordinate. Neutrons have no electric charge, and since nuclear systems exist, there must be attractive forces stronger than the Coulomb force at play on the length scale of nuclear existence. The interaction between the protons and neutrons in the nucleus is called the *strong nuclear force*: it is about 100 times stronger than the Coulomb force on the length scale of a nucleus but is negligible for longer distances.

Around 3000 nuclei have been observed, either in nature or in a laboratory. All but about 250 of these nuclei are unstable and will eventually decay into stable nuclei. The consequences of the interplay between the strong nuclear force and the Coulomb force are clear from Fig. 1.1: there are more neutron-rich nuclei than there are proton-rich nuclei, and the boundary on the neutron-rich side of the nuclear chart is much less well determined than it is on the proton-rich side, as it is more difficult to reach experimentally.

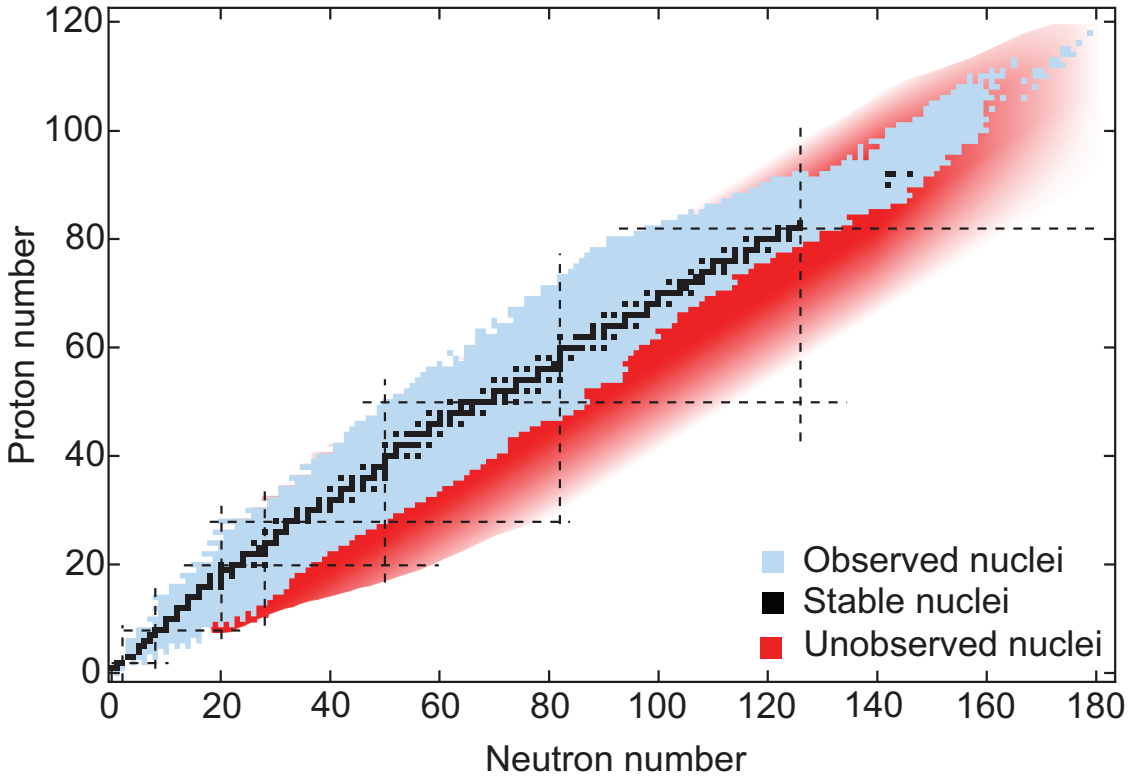

Figure 1.1: Plot showing the nuclear landscape. The number of neutrons (N) is plotted versus the number of protons (Z). Stable nuclei are shown as black boxes, observed unstable nuclei as blue boxes, and unstable nuclei predicted to exist, but not yet observed in red. Magic numbers (discussed in the text) are shown as dashed lines. For interpretation of the references to color in this and all other figures, the reader is referred to the electronic version of this dissertation. Fig. modified from [1]

There is a wealth of experimental evidence suggesting that nuclei have internal structure. Two such observables are the one- and two-neutron separation energies, given here in terms of the binding energy of the nucleus ($BE(N,Z)$), which describes the amount of energy required to dissociate a nucleus into the nucleons of which it is composed [2]:

$$BE(N,Z) = \left(ZM_p + NM_n - M(N,Z)\right)c^2 \tag{1.1}$$

here, $M(N,Z)$ is the mass of an atom with N neutrons and Z protons, $M_{p(n)}$ is the mass of a proton (neutron) and c is the speed of light. The one-neutron separation energy ($S_n(N,Z)$) is the energy required to remove a single neutron from the nucleus, and is the difference between the binding energy of the nucleus and that of the nucleus with one fewer neutron:

$$S_n(N,Z) = BE(N,Z) - BE(N-1,Z) \tag{1.2}$$

The difference between separation energies for neighboring nuclei (ΔS_n) can illustrate interesting changes in structure:

$$\Delta S_n = BE(N,Z) - BE(N-1,Z) - \left(BE(N+1,Z) - BE(N,Z)\right). \tag{1.3}$$

These values are plotted in Fig. 1.2 for even-even isotopic chains. The two-neutron separation energies are enhanced relative to their neighbors at neutron numbers 8, 20, 28, 50, 82, and 126. These numbers of neutrons or protons are called "magic numbers" and nuclei with a magic number of nucleons are called "magic" nuclei. This enhancement in the amount of energy required to removed nucleons from a magic nucleus suggests that magic nuclei are more tightly bound than their neighbors, and that the internal structure of a nucleus has

observable effects on its properties.

1.1 Nuclear Shell Model - Near Stability

In common with other quantum systems, the energy levels available to a nucleus are quantized. These energy levels are referred to by their radial quantum number, $n = 0, 1, 2...$, which counts the number of times the wave function of the particle changes sign, the orbital angular momentum of the state, $\ell = 0, 1, 2...n$ (it is common to refer to the $\ell = 0, 1, 2, 3...$ states by the letters $s, d, p, f...$) and the total angular momentum, $\vec{j} = \vec{\ell} + \vec{s}$, where $\vec{s}$ is the spin of a nucleon. Nucleons are Fermions and must obey the Pauli exclusion principle, so no two like nucleons can have the same three quantum numbers $(n\ell j)$. Thus, each orbital (j) has $2j + 1$ magnetic sub-states (m) and can contain $2j + 1$ nucleons, one in each sub-state.

In order to understand the mechanisms that create nuclear structure it is necessary to have nuclear models which predict observable features. One such picture is the *Single Particle Nuclear Shell Model*, which describes the interaction between nucleons in a nucleus in terms of a mean field potential, and treats the motion of a single nucleon in a potential created by all of the other nucleons in the nucleus. In such a framework the energy of the orbital occupied by a nucleon is referred to as the *single-particle energy*.

In the framework of the shell model, the magic numbers are explained as arising from the clustering of the energy levels available to the nucleons in the nucleus — some energy levels are close together, with large gaps between the cluster of levels (or single level) and the next higher energy level. If all the available levels in a cluster (or shell) have been filled, the shell is said to be closed.

A nucleus can be described as a system of A nucleons, whose Hamiltonian can be written

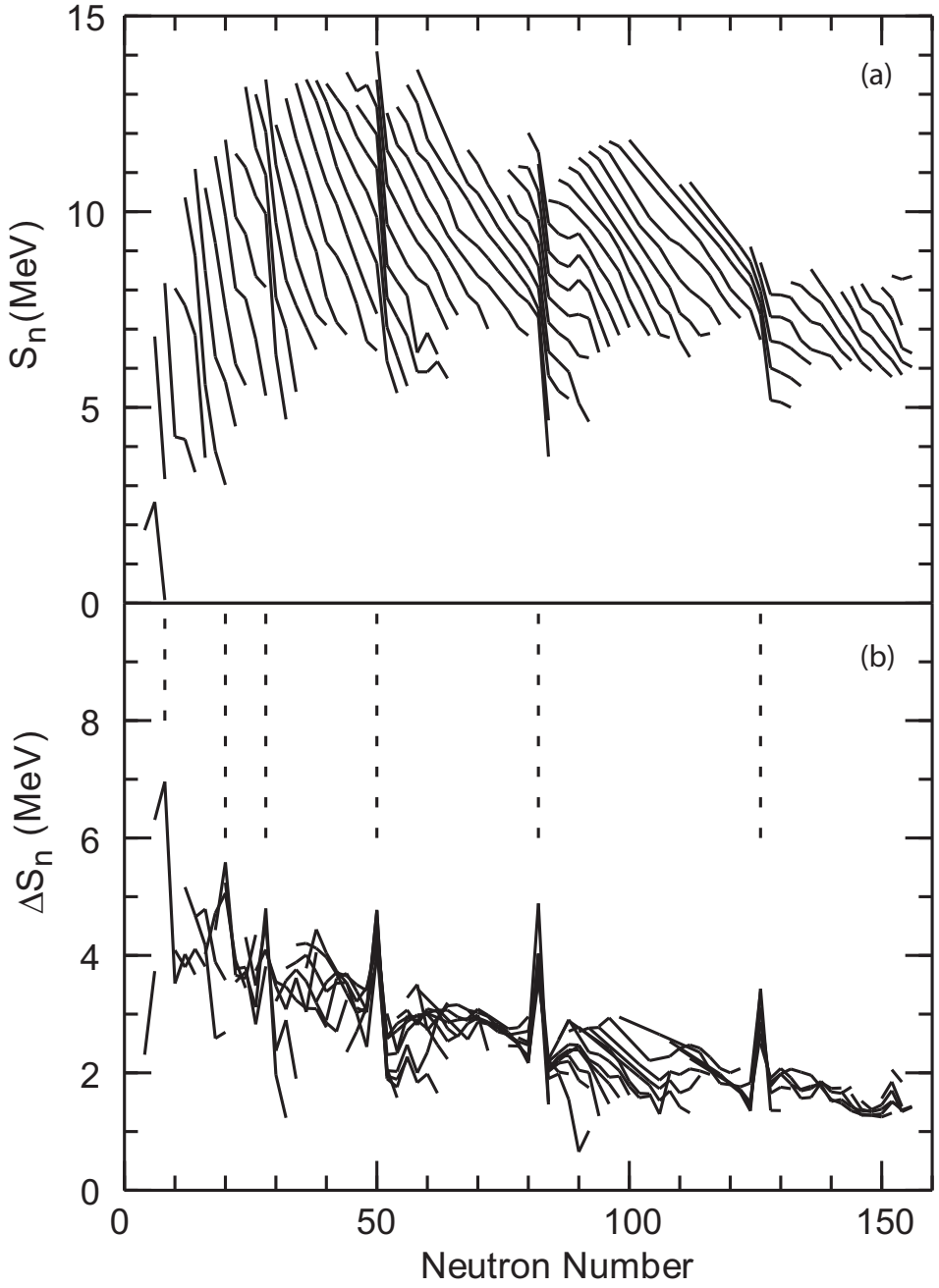

Figure 1.2: Panel (a) shows the one-neutron separation energies (see Eq. 1.2) plotted versus the neutron number (N) for even-even nuclei with more neutrons than protons. Nuclei with the same number of protons are indicated by connected lines. Panel (b) shows the two-neutron separation energies (see Eq. 1.3), again as a function of the neutron number for the same nuclei. The dashed lines correspond to the "magic numbers" of 8, 20, 28, 50, 82 and 126. Fig. from B. A. Brown [2].

in terms of the interaction between individual nucleons (see [3]):

$$H = \sum_{i=1}^{A} \frac{\mathbf{p}_i^2}{2m_i} + \sum_{i>k=1}^{A} V_{ik}\left(\mathbf{r}_i - \mathbf{r}_k\right) \tag{1.4}$$

here, the V_{ik} potential describes the two-body interaction between two nucleons and neglects the Coulomb interaction as being negligible on the length scale in question. The momentum and mass of each nucleon is described by $\mathbf{p}_i$ and m_i. The problem can be simplified by framing it in terms of the Hamiltonian of A particles which do not interact with one another very strongly, but move in a common mean field. The Hamiltonian can then be written as the unperturbed Hamiltonian (equation 1.4) plus a term due to the residual interaction between the particles and the mean field. In the simplest models using residual interactions, a nucleus is treated as a few-body system: a tightly bound *core*, in which no excitations are allowed, and one or more less tightly bound *valence nucleons*. The Hamiltonian of such a system is:

$$H = \sum_{i=1}^{A} \left[\frac{\mathbf{p}_i^2}{2m_i} + U_i\left(\mathbf{r}\right)\right] + \sum_{i>k=1}^{A} V_{ik}\left(\mathbf{r}_i - \mathbf{r}_k\right) - \sum_{i=1}^{A} U_i\left(\mathbf{r}\right) \tag{1.5}$$

the first term in this expression describes the motion in an independent mean field, and the second two terms are referred to as the residual interaction. This interaction can be modeled as the unperturbed Hamiltonian (H_0, Eq. 1.4) and a slightly perturbative potential describing the residual interactions (V_{res}):

$$H = H_0 + V_{res}. \tag{1.6}$$

One choice of the mean field potential is that of a harmonic oscillator:

$$U(r) = \frac{1}{2}\mu\omega^2 r^2 \ , \tag{1.7}$$

where the reduced mass of the system is μ and the level spacing depends on the oscillator frequency ω. The energy spectrum of such a system depends on the radial and orbital angular momentum quantum numbers and is given by:

$$E_{n\ell} = \left(2n + \ell - \frac{1}{2}\right)\hbar\omega \tag{1.8}$$

This three-dimensional harmonic oscillator potential predicts shell closures for N or $Z = 2$, 8, 20, 40, and 70. The lowest three numbers agree with the experimentally observed magic numbers of N or $Z = 2$, 8, 20, 28, 50, 82, and 126 — the others clearly do not. It is also possible to use a Woods-Saxon potential:

$$U(r) = \frac{V_0}{1 + e^{(r-R)/a}} \tag{1.9}$$

which, like the harmonic oscillator potential, successfully predicts magic numbers up to 20 and fails afterwards. For medium mass nuclei, the depth of the potential well is usually taken to be $V_0 = -50$ MeV, the nuclear radius is given by $R = r_0 A^{1/3}$, with $r_0 = 1.2$ fm. The diffusivity is usually fixed at $a = 0.6$ fm (c.f. [2]).

In 1949 Maria Goeppert-Mayer [4] and Otto Haxel, Hans Jensen, and Hans Suess [5] showed that adding a spin-orbit coupling term:

$$V_{s.o.}(r, \vec{\ell}, \vec{s}) = V_{s.o.}(r)\vec{\ell} \cdot \vec{s} \tag{1.10}$$

to the central potential reproduces the experimentally observed magic numbers. The shell closures predicted by the harmonic oscillator potential, the Woods-Saxon potential, and the Woods-Saxon potential plus a spin-orbit term are shown in Fig.1.3 for neutron single-particle states in ^{208}Pb [2].

The wave function of each single-particle energy level can be expressed as a having radial and spherical components:

$$\psi_{nlm}(r) = R_{n\ell}(r) Y_{\ell m}(\theta, \phi) \tag{1.11}$$

the radial wave function ($R_{n\ell}(r)$) does not depend on the sign of r, but if the spherical harmonic is reflected, the sign of the reflected spherical harmonic depends on ℓ: $Y_m^\ell(\theta, \phi) \rightarrow Y_m^\ell(\pi - \theta, \pi + \phi) = (-)^\ell Y_m^\ell(\theta, \phi)$, so each single-particle level will have parity ($\pi_{n\ell m} = (-)^\ell$). The total parity is then the product of all parities of the occupied single-particle levels:

$$\pi = \Pi_i^A (-)^{\ell i} = (-)^{\sum_i^A \ell_i}. \tag{1.12}$$

Although the extreme single-particle model of a nucleon moving in a mean field potential successfully reproduces the experimentally observed magic numbers, it does not accurately describe more detailed nuclear structure. In order to accomplish this, more complicated models which include two-body matrix elements deduced from fits to data are necessary. A discussion of such effective interactions can be found in [6].

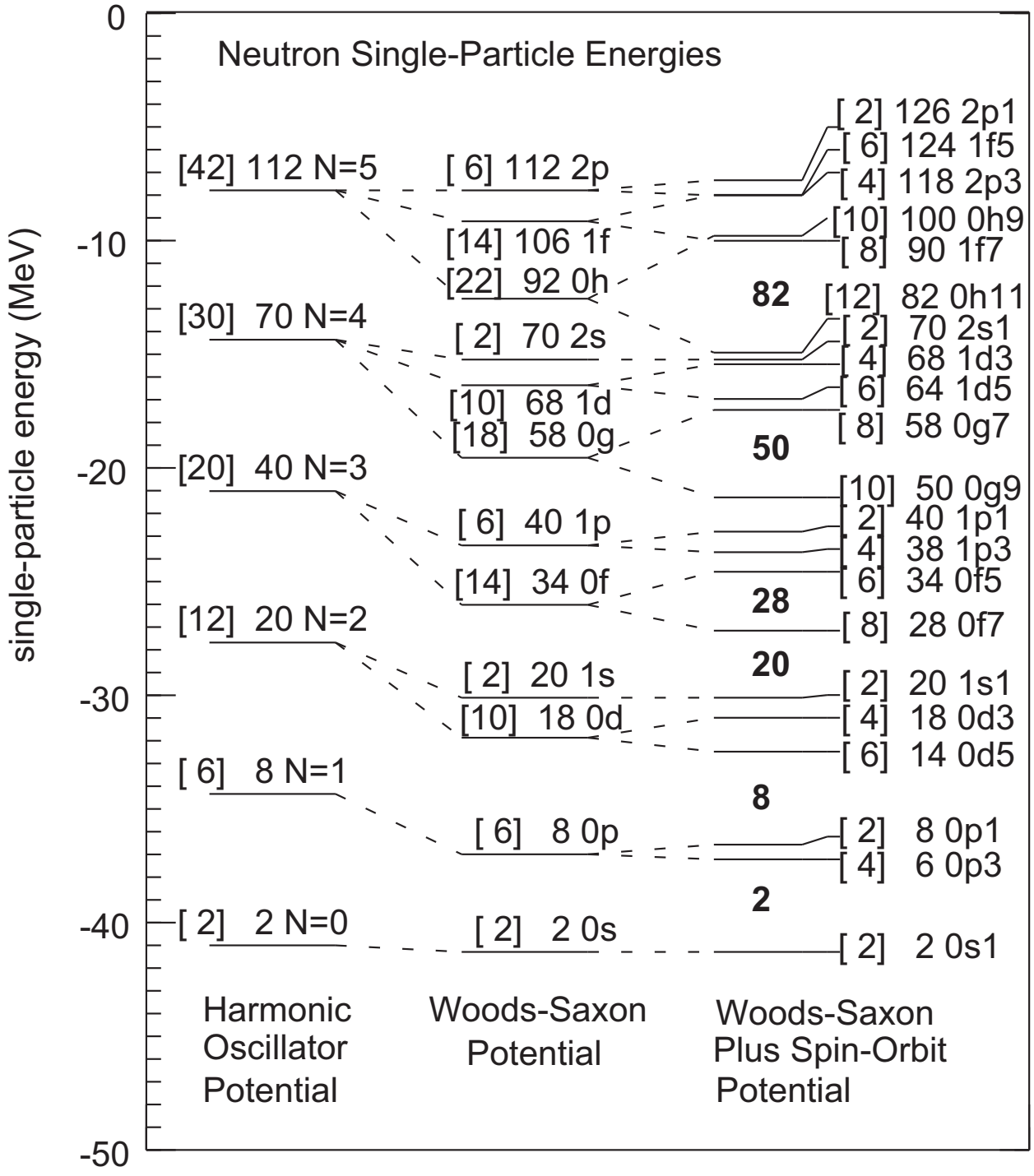

Figure 1.3: Schematic of neutron single-particle energies created by different potentials. From the left, the potentials shown are a 3D harmonic oscillator, a Woods-Saxon, and a Woods-Saxon plus a spin-orbit term. Each energy level is labeled in brackets by the number of nucleons it can contain, followed by the total number of nucleons in the system if the level is filled, followed by the quantum number(s) of the state. The magic numbers are noted in the gaps between levels for the potential with spin-orbit coupling. Fig. from [2].

1.1.1 Nuclear Shell Model - Away from Stability

Away from stability the arrangement of the single-particle energy levels in a nucleus has been shown to change for large isospin projection (T_z):

$$T_z = \frac{N - Z}{2} \tag{1.13}$$

This dependance of the ordering of the single-particle energy levels on the neutron to proton ratio of a nucleus causes some of the shell closures present at stability to disappear and new ones to develop in exotic nuclei with large T_z. An example of this behavior can be found in the appearance of a shell gap at $N = 32$ for ^{54}Ti, with $Z = 22$ [7]. These exotic nuclei thus provide the most stringent tests available for our models of nuclear structure.

One mechanism shown to drive this change in structure is the spin-isospin dependent part of the nucleon-nucleon interaction [8]. This monopole component of the tensor force affects the *effective single particle energy* (ESPE) of an orbital j, which describes the mean effect from all of the other nucleons on a nucleon in the particular single-particle orbital.

The single-particle energy of the orbital j is determined by its kinetic energy and the effects of the closed shell on this orbital [9]. The addition of nucleons to a different orbital, j', will affect the energy of the orbital j. The monopole component of this interaction is given by [9]:

$$V^T_{j,j'} = \frac{\sum_J (2J+1) \langle jj' | V | jj' \rangle_{JT}}{\sum_J (2J+1)} \tag{1.14}$$

here, $\langle jj' | V | jj' \rangle_{JT}$ is the diagonal matrix element related for the state with two nucleons which are coupled to an isospin (T) and angular momentum (J). The result ($V^T_{j,j'}$) is the monopole component of the nucleon-nucleon residual interaction between nucleons in the

orbital j' in the orbital j.

As nucleons fill the j' orbital, the single-particle energy of the j orbital is changed. If neutrons are in the j' orbital, protons are in the j orbital, and $j \neq j'$, then the single-particle energy of the proton orbital, j, is changed due to the monopole effect of Eq. 1.14 [9]:

$$\Delta\epsilon_\pi(j) = \frac{1}{2}\left\{V^{T=0}_{j,j'} + V^{T=1}_{j,j'}\right\} n_\nu\left(j'\right). \tag{1.15}$$

Here, $n_\nu\left(j'\right)$ is the number of neutrons in the orbit j' and $\Delta\epsilon_\pi(j)$ gives effective single particle energy of the orbital j. The expression for the shift in single-particle energy for neutrons instead of protons can be obtained by swapping π for ν.

The potential $V^T_{j,j'}$ is *attractive* between nucleons with opposite isospin and anti-aligned spins $(j_>, j'_<)$ and *repulsive* between nucleons with aligned spins $(j_>, j'_>)$. The proton in the j orbital will also influence the energies of neutrons in the j' orbital, but the $T = 0$ term is more attractive than is the $T = 1$ term [10].

This effect has been used to explain the modification of nuclear structure found in exotic nuclei across the nuclear landscape, for instance in the "Island of Inversion" [44] nuclei, with $20 \leq N \leq 22$ and $10 \leq Z \leq 12$, where the attraction between the $\pi 0d_{5/2}$ orbital and $\nu 0d_{3/2}$ orbital is decreased as the $\pi 0d_{5/2}$ orbital is depopulated [8]. This reduction in attraction between these two proton and neutron orbitals causes the $\nu 0d_{3/2}$ orbital to become less bound, narrowing the $N = 28$ gap between the $\nu 0d_{3/2}$ orbital and the neutron pf shell.

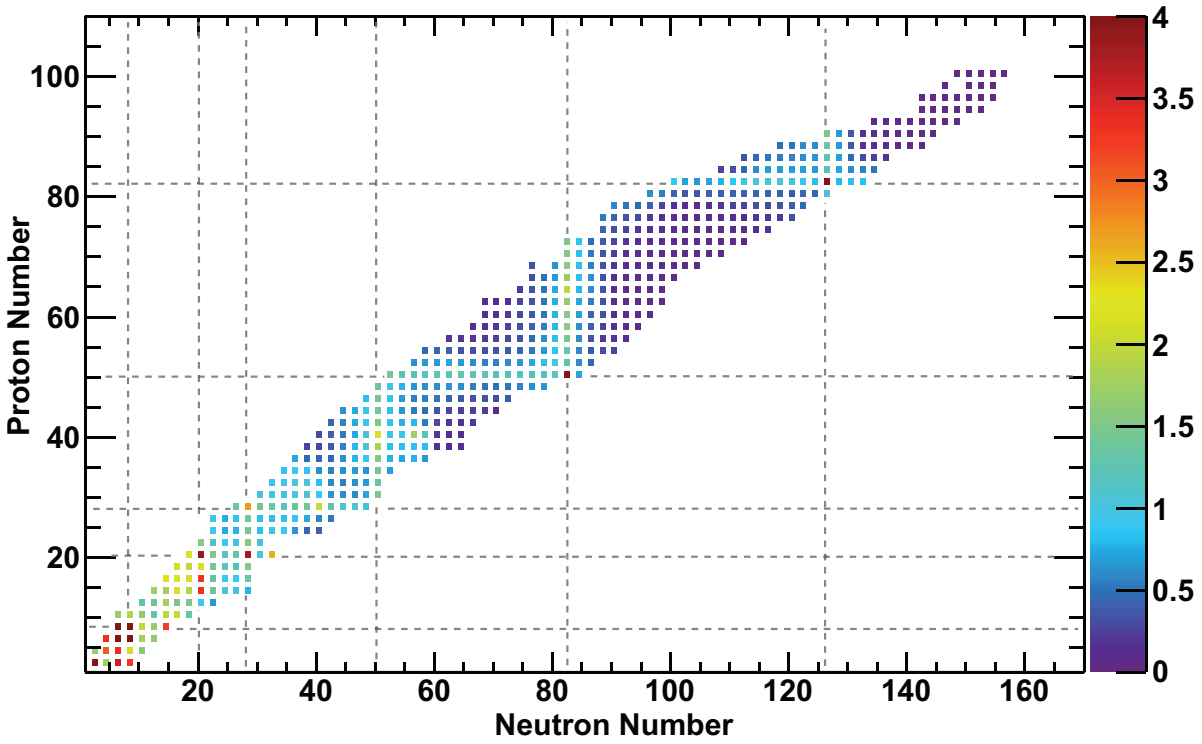

Figure 1.4: Energies of the first excited states with spin-parity $J^{\pi} = 2^{+}$ for even-even nuclei. The traditional magic numbers (2, 8, 20, 28, 50, 82, and 126) are noted by dashed lines - the enhancement of the energy of the first excited states follows the magic numbers and highlights the effect of shell closures. Data from [15, 16].

1.2 Signatures of Shell Closures

This work will focus on two indicators of shell closure: the energies of excited states in nuclei and on the probability of a transition between the ground state (the $B(E2; 0^{+}_{g.s.} \rightarrow 2^{+}_{1})$ value) and the energy of the first excited state with spin-parity 2^{+} ($E\left(2^{+}_{1}\right)$).

1.2.1 Excited State Energies

Even-even nuclei (nuclei with even numbers of protons and neutrons) have a ground state with spin-parity of $J^\pi = 0^+$ and typically[1] have a first excited state with spin-parity of $J_1^\pi = 2^+$. In magic nuclei near stability there tends to be a large energy gap between the ground state of the nucleus and the first excited state. As Fig. 1.4 shows, this behavior occurs broadly over the nuclear chart. It is clear that the enhancement in the energy of the first excited state is greatest near a shell closure, but decreases mid-shell before increasing again toward the next shell closure.

1.2.2 Quadrupole Collectivity

Geometric collective models of nuclei attribute low-lying excited states to the coherent motion of valence nucleons. These models describe two main excitation modes, *rotational* and *vibrational*, taking their names from the classical systems which approximate their excitation pattern.

1.2.2.1 Rotational and Vibrational Nuclei

A vibrational even-even nucleus has evenly-spaced energy levels. The ground state has spin-parity 0^+, the first excited state 2^+, then follows an ideally degenerate triplet of states, $4^+, 2^+$, or 0^+, and an ideally degenerate quintet of states $6^+, 4^+, 3^+, 2^+$, or 0^+. The energy of the n^{th} excited state in an even-even vibrational nucleus is given by:

$$E_{vib}(n) = nE\left(2_1^+\right). \tag{1.16}$$

[1] Some exceptions are ^{14}C, with $J_1^\pi = 1^-$, and ^{4}He, ^{16}O, ^{40}Ca, and ^{72}Kr which have $J_1^\pi = 0^+$

A rotational nucleus has an energy spectrum like a rigid rotor:

$$E_{rotor}(J) = \frac{\hbar^2}{2I} J\left(J+1\right), \tag{1.17}$$

where I is the moment of inertia of the nucleus. One can determine which collective model most closely describes an even-even nucleus by measuring the energies, spins and parities of the low-lying excited states.

1.2.2.2 B(E2) Values

The low-lying excited states of an even-even nucleus are indicative of its structure. The first of these excited states with spin-parity of 2^+ can only decay to the ground state (with spin-parity 0^+) by an electric quadrupole transition (which is discussed in Chapter 2). The strength of such an electric quadrupole (or $E2$) transition is of interest and can be used to illuminate properties of nuclear structure. The reduced transition probability between an initial state j_i and a final state j_f, the $B(E2)$ value, is given by:

$$B\left(E2; j_i \rightarrow j_f\right) = \frac{1}{2j_i+1} \left|\langle j_f| \left|\mathcal{O}(E2)\right| |j_i\rangle\right|^2. \tag{1.18}$$

here, $\mathcal{O}(E2)$ is the operator mediating the electric quadrupole transition and will be defined in Chapter 2. Because the strength of this observable depends on how strongly the initial and final states are connected through $\mathcal{O}(E2)$, it is a robust probe for measuring the collectivity of a nucleus. Nuclei with large $B(E2; 0^+_{g.s.} \rightarrow 2^+_1)$ values are said to be collective — for the example of the vibrational model, low-lying states are ascribed to the coherent excitation of nucleons, so a higher transition probability means that the motion of contributing nucleons is more in phase.

1.3 Evolution of Quadrupole Collectivity

Two probes for shell closures are the energy of the first excited state and the reduced transition strength. The first is expected to be enhanced at shell closures relative to mid-shell and the latter is expected to be reduced at shell closures relative to mid-shell. Both behaviors can be understood as the result of the separation between available energy levels at the shell closures.

1.3.1 The Calcium Isotopic Chain

A canonical example of the behavior discussed in Sec. 1.2 can be found in the calcium isotope chain. With $Z = 20$ all calcium isotopes are magic nuclei, but ^{40,48}Ca also have magic numbers of neutrons ($N = 20, 28$) and are called *doubly-magic* for this reason. As shown in Fig. 1.5, the magic nature of ^{40}Ca is driven by the large energy gap between the filled $\pi, \nu 0d_{3/2}$ orbitals and the unfilled $\pi, \nu 0f_{7/2}$ orbitals. The energy of the first 2^+ state in ^{40}Ca is 3.904 MeV, while that of the first 2^+ excited states in its neighbors with two less neutrons (^{38}Ca) and two more neutrons (^{42}Ca) are 2.213 and 1.524 MeV, respectively. This behavior continues towards ^{48}Ca; the first 2^+ excited state energies are all lower than 1.6 MeV, while the energy of the first 2^+ excited state in the $N = 28$ nucleus ^{48}Ca is, at 3.8 MeV, dramatically enhanced relative to mid-shell. This behavior is illustrated in the lower panel of Fig. 1.6.

The $B(E2)$ values for the calcium isotopic chain are enhanced at mid-shell relative to the shell closures at $N = 20, 28$, as shown in the upper panel of Fig. 1.6. These features make the even-even $^{40-48}$Ca isotopic chain an excellent reference for the persistence of shell closures in the neighboring $sd - pf$ shell nuclei, such as for the silicon (with $Z = 14$), sulfur

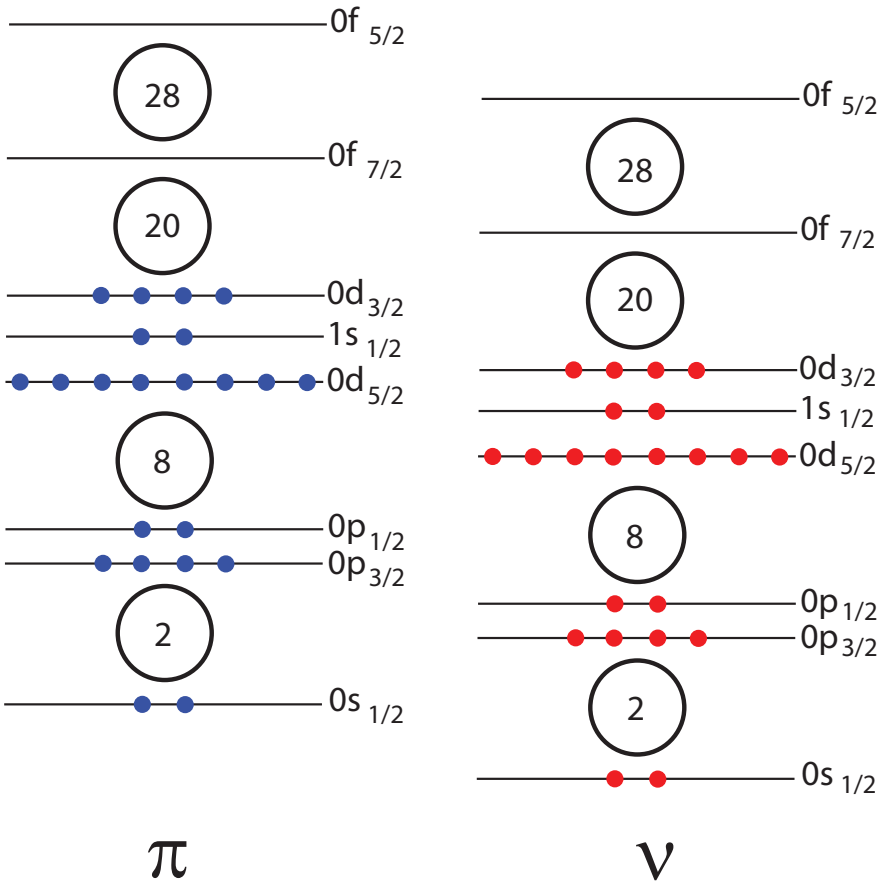

Figure 1.5: Schematic of the occupation of proton (left, π) and neutron (right, ν) orbitals in ^{40}Ca. The doubly-magic nature of the nucleus is shown to arise from the energy gaps between the filled proton and neutron $0d_{3/2}$ orbitals and the unfilled $0f_{7/2}$ orbitals. The relative positions of the proton and neutron energy levels are not to scale — the offset from the Coulomb force to the proton energy levels is only schematically included.

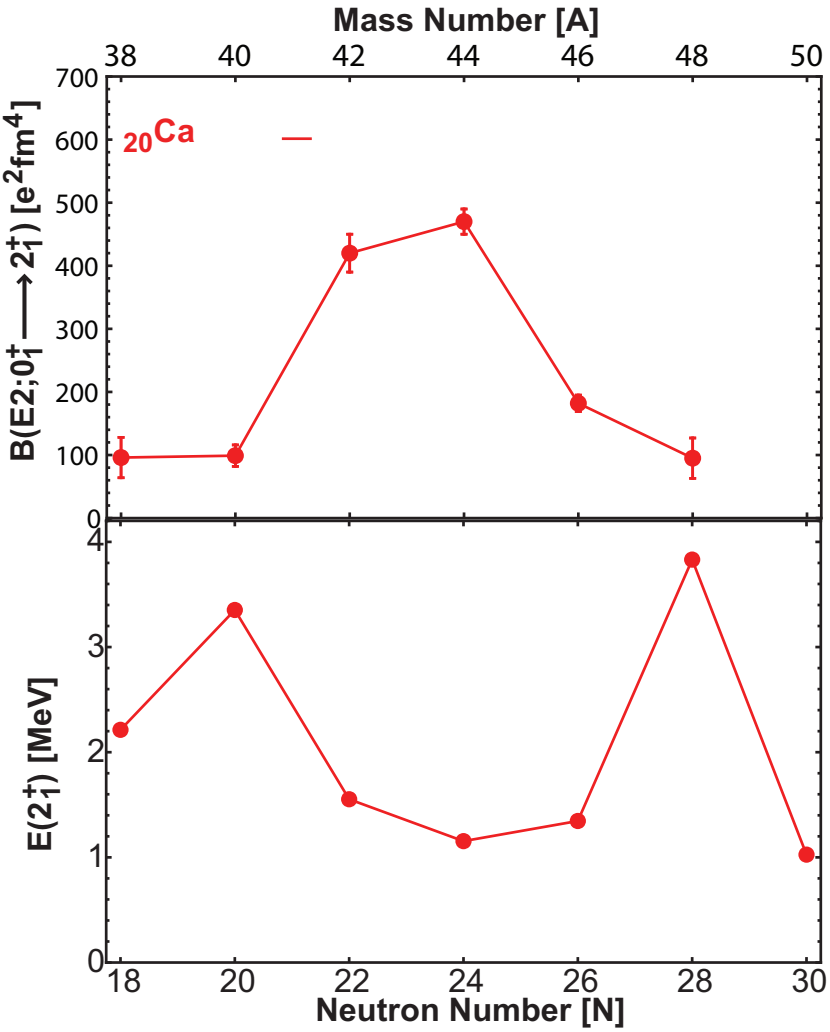

Figure 1.6: Evolution of collectivity for even-even Ca isotopes ($Z = 20$) as a function of the number of neutrons. The top panel shows the reduced transition probability to the first excited state and is enhanced mid-shell relative to the shell closures at $N = 20, 28$, as expected. The lower panel shows the energies of the first excited states, which are enhanced at the neutron shell closures relative to mid-shell. Data are from ENSDF [14].

($Z = 16$) and argon ($Z = 18$) isotope chains.

1.3.2 The Neutron SD-PF Shell: The Silicon Isotopic Chain

In order to investigate the persistence of shell closures it is necessary to investigate the structure of exotic nuclei. The even-even isotopic chain $^{34-42}$Si, with $Z = 14$ are an ideal site for such a study, as they intersect $N = 20, 28$ and are experimentally accessible with the current generation of accelerators. The persistence of the $N = 28$ shell closure is of particular interest, as it is the first shell closure attributed to the spin-orbit interaction.

1.3.2.1 A Selected Experimental History of the Silicon Isotopic Chain

In 1998, Ibbotson *et al.* [17] measured the first excited state energies and $B(E2)$ values for $^{32-38}$Si via intermediate-energy Coulomb excitation at NSCL. Ibbotson's measurements of the B(E2) values have uncertainties on the order of 30%.

In 2006 Campbell *et al.* [18, 19, 20] measured the energy of excited states in ^{40}Si via proton inelastic scattering at NSCL (this measurement and technique will be discussed in the next chapter). This measurement showed a slightly lower excited state energy ($E(2_1^+) =$ 986(5) keV) than the neighboring $N = 26$ calcium nucleus ^{46}Ca ($E(2_1^+) = 1346.0(3)$ keV), suggesting an increase in collectivity. However, matrix elements deduced from proton inelastic scattering cannot be directly compared to the electromagnetic transition strength.

In 2005, Fridmann *et al.* [22, 23] probed the persistence of the $Z = 14$ sub-shell gap for $N = 28$ via the 2-proton knockout reaction ^{44}S-2p and, from the low-lying levels in ^{43}P, concluded that the $Z = 14$ sub-shell gap is still present at ^{42}Si. Subsequently, Bastin *et al* [21] measured the energy of the first excited state in ^{42}Si to be $E\left(2_1^+\right) = 770(19)$ keV, suggesting that the $N = 28$ shell closure collapses for $Z = 14$.

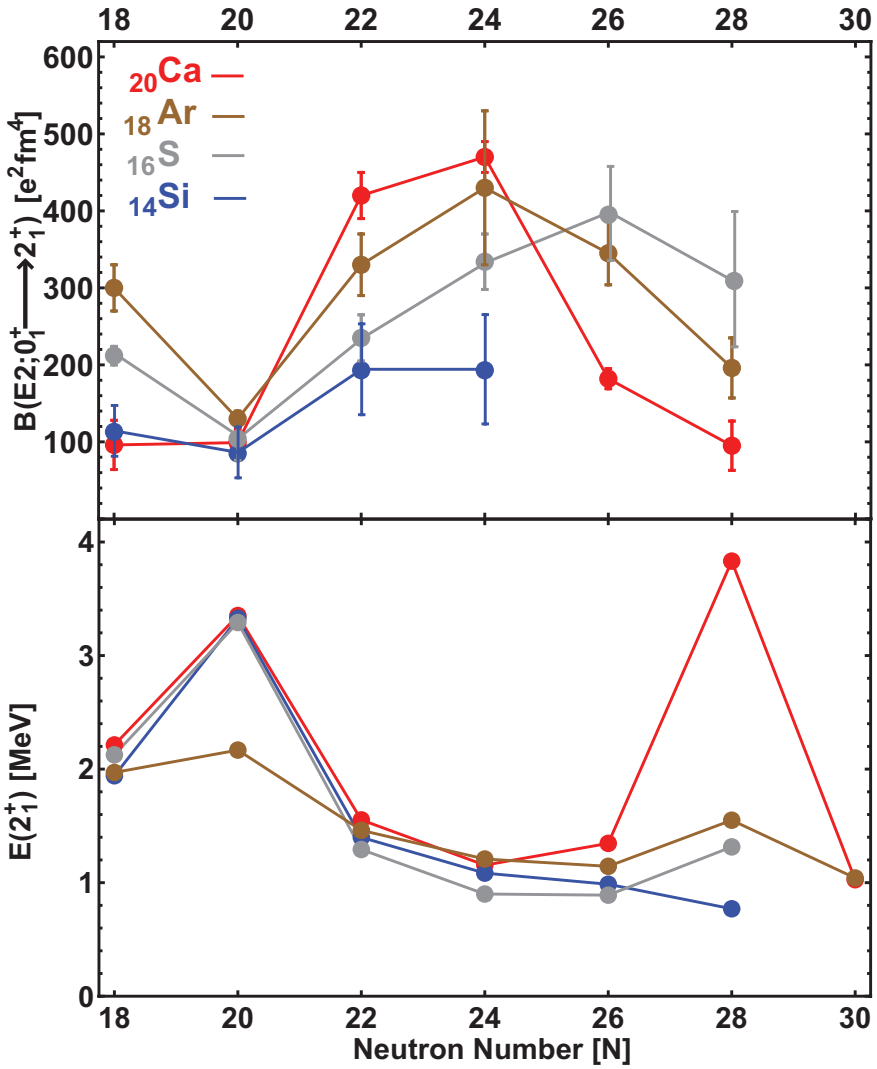

Figure 1.7: Evolution of collectivity in the $sd-pf$ shell. The erosion of the N=28 shell closure is apparent at Z=16 due to the large $B(E2)$ value and low $E(2_1^+)$ for ^{44}S, which is still slightly enhanced relative to the $E(2_1^+)$ for ^{42}S. However, the $N=28$ shell closure collapses for Z=14, as is apparent from the reduction in $E(2_1^+)$ for ^{42}Si. Data from ENSDF [14].

1.3.2.2 Other Nuclei in the Neutron SD-PF Shell

The $N = 28$ shell closure persists for the other even-even *sd-pf* shell nuclei — the sulfur (S, $Z = 16$) and argon (Ar, $Z = 18$) isotopes. As Fig. 1.7 shows, the sulfur isotopes exhibit characteristics collectivity. The $Z = 16$ sub-shell gap corresponds to the filling of the $\pi 1s_{1/2}$ orbital. The argon isotopes, with $Z = 18$, are produced by half-filling the $\pi 0d_{3/2}$ orbital, and are not expected to behave like doubly-magic nuclei. The persistence of the $N = 28$ shell closure for $Z = 16, 18$, although reduced at $Z = 16$, is seen by the enhancement of $E(2_1^+)$ relative to mid-shell and reduction in $B(E2; 0_{g.s.}^+ \rightarrow 2_1^+)$ value relative to mid-shell. The dramatically different behavior of the silicon isotope chain is highlighted by the *reduction* of $E(2_1^+)$ at $N = 28$ relative to mid-shell, in contrast to all of the other $sd-pf$ nuclei discussed. Even more striking is that the energy of the first excited state in ^{42}Si is the lowest in the region.

The collapse of the $N = 28$ shell closure for $Z = 14$ needs further investigation so that the mechanisms driving it can be understood. In particular, the value of electric quadrupole transition matrix element must be measured in order to constrain the theories predicting structure in this region. The focus of this work is to measure for the first time the $B\left(E2; 0_{g.s.}^+ \rightarrow 2_1^+\right)$ values for ^{40,42}Si and to reduce the uncertainty in this value for $^{34-38}$Si. These measurements will describe the evolution of quadrupole collectivity along $Z = 14$ in a coherent way and will shed light on the collapse of the $N = 28$ shell closure.

Chapter 2

Measuring Quadrupole Collectivity

Gamma-ray spectroscopy is an experimental technique to probe the structure of low-lying excited states in nuclei by measuring the γ rays emitted in their decay. This chapter discusses different spectroscopic techniques, with a focus on those that probe collective behavior by measuring the strength of an electric quadrupole transition between an excited state and the ground state of a nucleus.

A magnetic transition of multipolarity λ between an initial state ($J_i^{\pi_i}$) and a final state ($J_f^{\pi_f}$) in a nucleus is mediated by an magnetic transition operator, given by [2]:

$$\mathcal{O}(M\lambda) = \left[\vec{\ell}\frac{2g_{t_z}^{\ell}}{(\lambda+1)} + \vec{s}\, g_{t_z}^{s}\right] \vec{\nabla}\left[r^{\lambda}Y_{\mu}^{\lambda}(\theta,\phi)\right]\mu_N \ . \tag{2.1}$$

Here, $Y_{\mu}^{\lambda}(\theta,\phi)$ are spherical harmonics, μ is the projection of λ, $g_{t_z}^{\ell}$ is the orbital g-factor for a nucleon, $g_{t_z}^{s}$ is the spin g-factor for a nucleon, and μ_N is the nuclear magneton. The orbital g-factor for a free proton is $g_p^{\ell} = 1$, the orbital g-factor value for a free neutron is $g_n^{\ell} = 0$, and the spin g-factor values for a free proton or neutron are $g_p^{s} = 5.586$ and $g_n^{s} = -3.826$,

respectively [2].

The electric transition operator is given by [2]:

$$\mathcal{O}(E\lambda) = e_{t_z} e r^{\lambda} Y^{\lambda}_{\mu}(\theta, \phi) \ , \tag{2.2}$$

where $e_{t_z} e$ are the electric charges for the proton or neutron. the proton (e_π) and neutron (e_ν) electric charges can either be taken to be the values for free nucleons, in which case $e_\pi = 1$ and $e_\nu = 0$, or effective charges, which compensate for the truncation of the model space in shell model calculations. The focus of this work is on electric quadrupole ($E2$) transitions. This operator is given by (Eq. 2.2):

$$\mathcal{O}(E2) = e_{t_z} e r^2 Y^2_{\mu}(\theta, \phi) \ . \tag{2.3}$$

Recall that the reduced electric quadrupole transition probability (as given in Eq. 1.18) is:

$$B\left(E2; J_i \to J_f\right) = \frac{1}{2J_i + 1} \left| \langle j_f | \left| \mathcal{O}(E2) \right| | j_i \rangle \right|^2 \ , \tag{2.4}$$

where j_i is the spin of the initial state and j_f is the spin of the final state. The $B(E2)$ value can also be expressed in terms of effective charges (c.f. [24]):

$$B(E2) = \frac{1}{2J_i + 1} e^2 \left(e_\pi A_\pi + e_\nu A_\nu \right)^2 \ , \tag{2.5}$$

where $A_{\pi(\nu)}$ are the proton (neutron) electric quadrupole transition matrix elements.

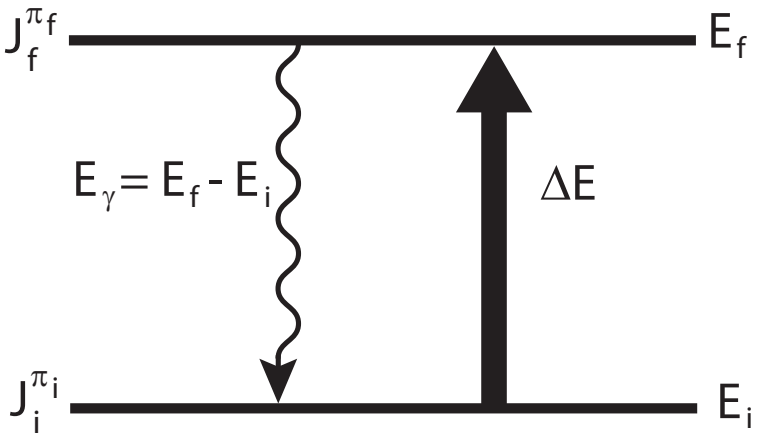

Figure 2.1: Schematic of the excitation of a nucleus (solid arrow) resulting the emission of a de-excitation γ ray (squiggly arrow).

2.1 Accessible States

Electromagnetic transitions conserve parity, thus the parities of initial and final states accessible through electromagnetic transitions are given by:

$$\begin{aligned} \pi_i\pi_f &= (+1) \text{ for } M1, E2, M3, E4... \\ \pi_i\pi_f &= (-1) \text{ for } E1, M2, E3, M4.... \end{aligned} \tag{2.6}$$

Conservation of angular momentum requires that, if a γ ray is emitted, it have λ units of angular momentum:

$$\left| j_i - j_f \right| \leq \lambda \leq j_i + j_f \ . \tag{2.7}$$

Gamma transitions with $\lambda = 0$ are forbidden[1]. If they were not, the de-excitation photon would have angular momentum of $0\hbar$.

To estimate orders of magnitude and relative strengths of transitions with different mul-

[1] M0 transitions are forbidden for the obvious reason that magnetic monopoles do not exist; E0 transitions proceed via internal conversion, in which the excited state in the nucleus de-excites by transferring its energy to an atomic electron [25].

tipolarity, the transition from the state j_i to the state j_f can be modeled as resulting from the excitation of a single proton (this is called a "Weisskopf estimate"). The probability for such a transition can then be expressed in *Weisskopf* or *single-particle* units for magnetic transitions as [25]:

$$\begin{aligned}
\lambda(M1) =& 5.6 \times 10^{13} E^3 \\
\lambda(M2) =& 3.5 \times 10^{7} A^{2/3} E^5 \\
\lambda(M3) =& 16 A^{4/3} E^7 \\
\lambda(M4) =& 4.5 \times 10^{-6} A^2 E^9 \ .
\end{aligned} \tag{2.8}$$

Here λ is the probability per second of the transition, A is the number of nucleons in the nucleus and E is the energy of the de-excitation photon in MeV.

The probability per second for the lowest-order electric multipole transitions are [25]:

$$\begin{aligned}
\lambda(E1) =& 1.0 \times 10^{14} A^{2/3} E^3 \\
\lambda(E2) =& 7.3 \times 10^{7} A^{4/3} E^5 \\
\lambda(E3) =& 34 A^2 E^7 \\
\lambda(E4) =& 1.1 \times 10^{-5} A^{8/3} E^9 \ .
\end{aligned} \tag{2.9}$$

In the case of a transition between the first 2^+ excited state and the 0^+ ground state in an even-even nucleus, the only allowed transition is $\pi\lambda = E2$. For transitions between 2^+ states, e.g. $2_2^+ \rightarrow 2_1^+$, $\pi\lambda = M1$, $E2$, $M3$, and $E4$ are allowed, but due to the relative probability of the different multipolarities, these transitions proceed by a mixture of $M1$ and $E2$ only.

2.2 Techniques

There are many techniques to measure the strength of the electric quadrupole transition in a nucleus. Two will be noted here briefly, a third in greater detail.

2.2.1 Excited-State Lifetime Measurements

The probability for the transition per unit time, $W_{if}^{(\pi\lambda)}$, between an initial and final state is related to $B(\pi\lambda)$ value in the following way [2]:

$$W_{i\to f}^{\pi\lambda} = \left(\frac{8\pi\,(\lambda+1)}{\lambda\,[(2\lambda+1)!!]^2}\right)\left(\frac{k^{2\lambda+1}}{\hbar}\right)B\left(\pi\lambda; j_i \to j_f\right). \tag{2.10}$$

With $k = E_\gamma/\hbar c$, where E_γ is in MeV, and the $B(E2)$ value is in units of $\mathrm{e}^2\mathrm{fm}^4$. The lifetime of the excited state is $\tau_{if} = 1/W_{if}$, so a measurement of the lifetime of an excited state can be used to extract its $B(\pi\lambda)$ value.

A detailed description of the measurement of the strength of the electric quadrupole transition in exotic nuclei via lifetime techniques optimized for NSCL beam energies is given in Philip Voss' Ph.D. thesis [26].

2.2.2 Proton Inelastic Scattering

Proton inelastic scattering with exotic nuclei is done in inverse kinematics — the target is typically made of plastic, liquid hydrogen, or frozen hydrogen. The isotope of interest is accelerated and impinged upon the target. When the target is made of plastic the contribution to the reaction cross section from the carbon in the plastic must be subtracted. The target excites the nucleus of interest, which then emits de-excitation γ rays (see Fig. 2.1).

The excitation cross section, given by:

$$\sigma_{i\to f} = \frac{N_\gamma}{N_B N_T} \ , \tag{2.11}$$

which is determined from the number of de-excitation γ rays emitted (N_γ) relative to the number of target nuclei (N_T) and the number of projectiles incident on the target (N_B). The excitation cross section can be used to determine the shape of the nucleus in a model dependent way. The parametrization of the shape of the nucleus can be used to infer the contribution of protons and of neutrons to the deformation, also in a model dependent way.

Proton inelastic scattering is a hadronic probe, so it is sensitive to both the proton and neutron degree of freedom. The sensitivity ($b_{\pi(\nu)}$) to protons or neutrons varies depending on the energy regime of the probe [27]. The relative sensitivities are given in Tab. 2.1 for low-energy proton inelastic scattering.

The interactions of all the protons or all the neutrons in a nucleus with an external field can be treated individually and the operator mediating these transitions expressed as the sum over all the protons and neutrons in the nucleus [27]:

$$\mathcal{O}_{\lambda\mu} = b_\nu \sum_\nu r_i^\lambda Y_\mu^\lambda \left(\theta_i, \phi_i\right) + b_\pi \sum_\pi r_i^\lambda Y_\mu^\lambda \left(\theta_i, \phi_i\right) \ . \tag{2.12}$$

It is worth noting explicitly that if the probe is electromagnetic (as is the case in Coulomb excitation), $b_\nu = 0$, and the probe is only sensitive to the proton degree of freedom. Otherwise, one can extract the ratio of the neutron transition matrix element ($\mathcal{M}_\nu$) to the proton

External Field	Energy (MeV)	b_ν/b_π
EM	-	0
π	10-50	≈ 3
ν	10-50	$\approx 1/3$
π	100-200	≈ 1
ν	100-200	≈ 1

Table 2.1: Sensitivity of probe to nucleon species. At high center of mass energies ($\approx$ 100-200 MeV), the nuclear interior is transparent to the probe and the sensitivity of proton inelastic scattering to protons and neutrons is the same ($b_\nu/b_\pi \approx 1$) [28].

transition matrix element ($\mathcal{M}_\pi$) [28]:

$$\frac{\mathcal{M}_\nu}{\mathcal{M}_\pi} = \frac{b_\pi}{b_\nu}\left(\frac{\delta_{(p,p')}}{\delta_C}\left(1+\frac{b_\nu}{b_p}\frac{N}{Z}\right)-1\right) \ . \tag{2.13}$$

Here $\delta_{(p,p')}$ is the deformation length extracted from a parametrization of the nuclear deformation and δ_C is the deformation length extracted from a quantity sensitive to the proton degree of freedom alone, e.g. the $B(E2)$ value. The $\delta_{(p,p')}$ deformation length is deduced in a model-dependent way from a calculation of the excitation cross sections. This process will be discussed subsequently.

2.2.2.1 Extracting the Quadrupole Deformation Parameter

The shape of a deformed nucleus can be expressed in the formalism of the Liquid Drop Model as the surface vibrations of a liquid drop, or as the rotations of a deformed drop [29, 30]. In particular, the shape of an axially symmetric, quadrupole deformed nucleus can be expressed as [30]:

$$R(\theta) = R_0\left(1+\beta_2 Y_0^2(\theta,0)\right) \ , \tag{2.14}$$

where $R_0 = 1.2 \text{ fm} \cdot A^{1/3}$ is the nuclear radius, β_2 is the quadrupole deformation parameter and is related to the deformation length by $\delta = \beta_2 R_0$. In the rotational model of the

nucleus, assuming that the charge is uniformly distributed inside the nucleus, the deformation parameter can be related to the $B(E2\uparrow)$ value by [31]:

$$\beta_2 = \frac{4\pi}{3ZR_0^2}\sqrt{B(E2\uparrow)/e^2}. \tag{2.15}$$

Here, Z is the atomic number of the nucleus and the $B(E2\uparrow)$ value is in units of $\mathrm{e}^2\mathrm{fm}^4$. The deformation parameter obtained from a proton inelastic scattering measurement, $\beta_{2,(p,p')}$, can be extracted from a calculation of the cross section for the reaction, for example by a coupled-channels calculation.

The calculation of the cross section for a nuclear reaction must include all the excited states produced by the reaction. To simplify this discussion for proton inelastic scattering, the assumption is made that the target is made of hydrogen. Discussions of such "coupled channels" calculations can be found in works by Thompson and Nunes [32] or by Hodgson [33]. These calculations involve an optical model potential, which has real and imaginary components and (for proton inelastic scattering) describes a proton-nucleus interaction. The form of the optical model potential is (c.f. [33]):

$$V(r) = (U + iW)\, f(r, R, a)\ , \tag{2.16}$$

where U is the real part of the potential, W is the imaginary part of the potential, and $f(r, R, a)$ is a Woods-Saxon function (given in Eq. 1.9). The Woods-Saxon parameter R describes the radius of the system (typically $R = r_0 A^{1/3}$, with $r_0 = 1.2$ fm) and a is the surface-diffuseness parameter. This simplistic form is not sufficient to describe elastic scattering data, so optical model potentials such as the one by Koning and Delaroche [34]

include surface and spin-orbit terms.

In principle, the coupled channels calculation includes all the nuclear states, both bound and unbound. Of course such a complete description is impossible, so the absorptive imaginary potential is used to account for the states not explicitly included in the calculation.

In the case of axially symmetric quadrupole deformed nuclei, the radius given in Eq. 2.14 is used instead of the unperturbed radius (R) in the optical model potential, and (assuming the perturbation to the radius is small) the potential becomes:

$$V(r,\theta) = V\left(r - R\right) - \beta R Y_0^2\left(\theta, 0\right) \frac{dV}{dr} \ . \tag{2.17}$$

The solutions to the Schrödinger equation describing the projectile-target system are typically calculated by computer codes, such as FRESCO [35] or ECIS [36, 37]. The quadrupole deformation parameters are extracted by adjusting their values in the calculation to reproduce the excitation cross sections. By this method it is possible to deduce the deformation parameters, thus the magnitude of the quadrupole deformation, from (p, p') scattering data. However, this method is highly model dependent at many different steps.

It is possible to use a probe sensitive only to electromagnetic transitions as a less model-dependent complementary approach to this hadronic probe. Together, the two probes allow the determination of the relative contributions to the deformation from both protons and neutrons. Intermediate-energy Coulomb excitation is one such probe, as it is sensitive only to electromagnetic transition matrix elements.

2.2.3 Intermediate-Energy Coulomb Excitation

In intermediate-energy Coulomb excitation in inverse kinematics, a projectile moving with a velocity between $0.25 \lesssim v/c \lesssim 0.65$ interacts with the Coulomb field of a high-Z target and the projectile and target can be excited in the process [38]. Intermediate-energy Coulomb excitation occurs *above* the Coulomb barrier, so in principle nuclear contributions to the excitation cross section are possible. For this reason the analysis of intermediate-energy Coulomb excitation experiments is restricted to small scattering angles corresponding to large impact parameters. This section discusses one theory describing intermediate-energy Coulomb excitation.

The experimental cross section ($\sigma_{0^+ \rightarrow 2^+}$) for the intermediate-energy Coulomb excitation of the first excited state with spin-parity 2^+ in an even-even nucleus is the number of γ-rays emitted (N_γ), divided by the number of particles in the beam (N_B) and the number of scattering centers in the target (N_T):

$$\sigma_{0^+ \rightarrow 2^+} = \frac{N_\gamma}{N_B N_T} \ . \tag{2.18}$$

The theory of Alder and Winther [40] for intermediate-energy Coulomb excitation expresses the excitation cross section as being directly proportional to the observable of interest, the $B(E2)$ value. Following their formulation, the relationship between the integrated cross section and the $B(E2)$ value can be deduced:

$$\left(\frac{d\sigma}{d\Omega}\right) = \left(\frac{d\sigma}{d\Omega}\right)_{Rutherford} P_{i \rightarrow f} \ . \tag{2.19}$$

The differential cross section is first expressed as the Rutherford differential cross section

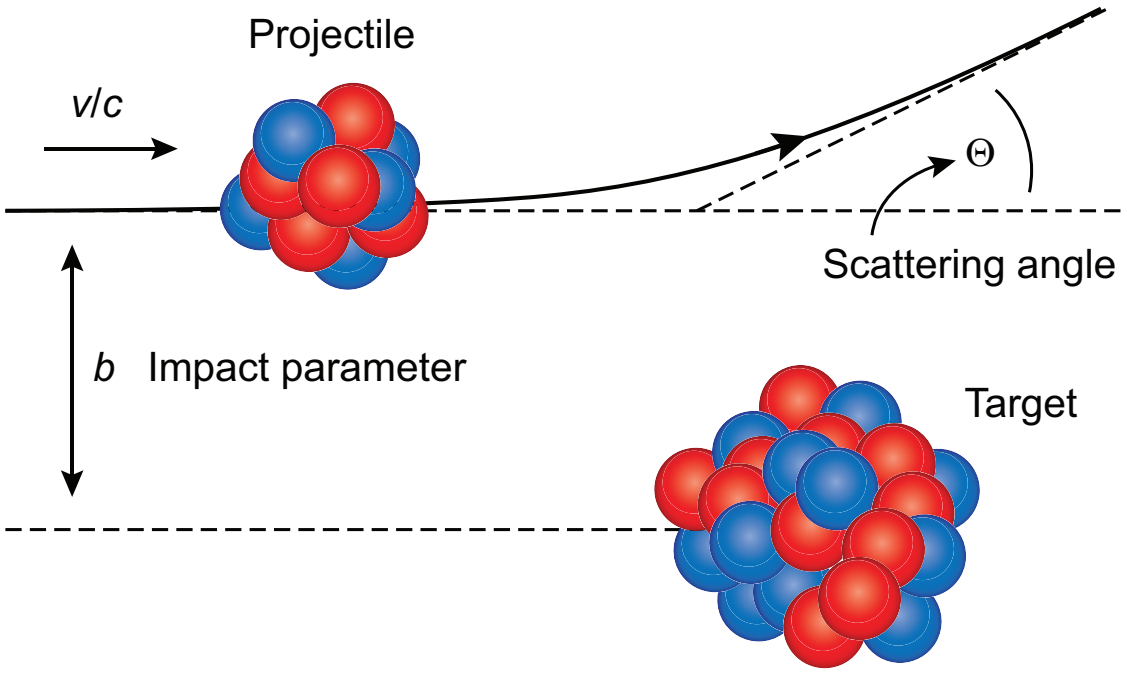

Figure 2.2: Schematic of intermediate-energy Coulomb excitation kinematics. Parameters discussed in text. Fig. from [1].

(which describes elastic scattering) times the probability for inelastic scattering, $P_{i\to f}$. The reaction kinematics are illustrated in Fig. 2.2, where the velocity (v) of the projectile is given in terms of the speed of light (c), the center of mass scattering angle is denoted by Θ, and the impact parameter by b. The impact parameter is related to the center of mass scattering angle by [39]:

$$b = \frac{a_\circ}{\gamma} \cot\left(\frac{\theta}{2}\right) \ , \tag{2.20}$$

where $\gamma = 1/\sqrt{1-(v/c)^2}$, and $a_\circ$ is the half-distance of closest approach:

$$a_\circ = \frac{Z_t Z_p e^2}{\mu v^2} \ . \tag{2.21}$$

Here, $Z_{t(p)}$ is the atomic number of the target (projectile), e is the electric charge and μ is the reduced mass of the projectile-target system.

Intermediate-energy Coulomb excitation occurs above the Coulomb barrier, where nuclear effects can contribute to the excitation cross section. If there are nuclear contributions to the excitation, the measured excitation cross section will not be solely indicative of the strength of the electric quadrupole transition. In order to restrict the contribution of nuclear effects to the excitation cross section, the impact parameter for the reaction is typically chosen to be at least two fermi larger than the sum of the nuclear radii of the projectile and the target (c.f. Gade *et al.* [43]):

$$b = 1.2 \text{ fm} \cdot \left(A_t^{1/3} + A_p^{1/3} \right) + 2 \text{ fm}. \tag{2.22}$$

this is typically referred to as the *minimum impact parameter* for safe Coulomb excitation at intermediate energies.

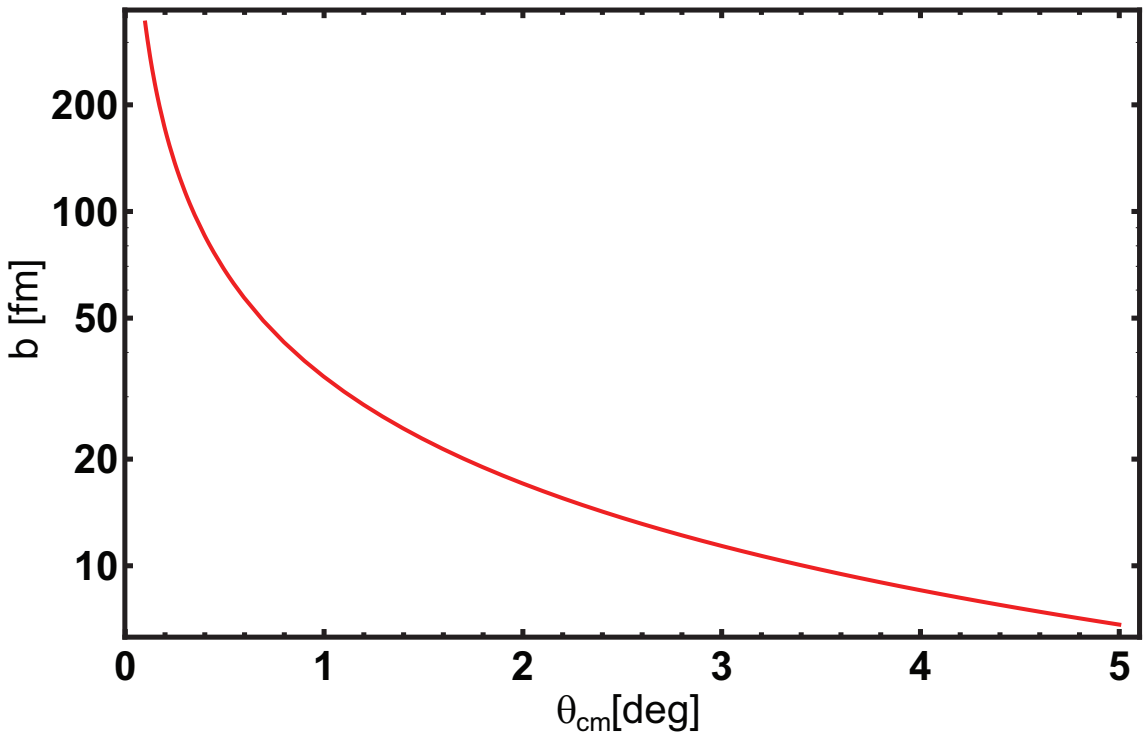

Figure 2.3: A plot showing the impact parameter (in log scale) as a function of center of mass scattering angle (see Eq. 2.20) for a ^{40}Si beam moving with 40% of the speed of light impinged on a ^{197}Au target.

Figure 2.3 shows the relationship between the center of mass scattering angle and the impact parameter for a ^{40}Si beam moving at 40% of the speed of light impinged upon a ^{197}Au target. ^{197}Au, with 79 protons, has a large Coulomb field and is isotopically pure, so it is a common choice for a Coulomb excitation target.

The excitation probability, $P_{i\to f}$, is the complex conjugate of the excitation amplitude and can be evaluated via perturbation theory if the Coulomb potential is time-dependent:

$$\begin{aligned} P_{i\to f} &= \left| a_{i\to f} \right|^2 \\ a_{i\to f} &= \frac{1}{i\hbar} \int_{-\infty}^{\infty} dt e^{it\Delta E/\hbar} \left\langle f \right| V_C \left(\vec{r}(t) \right) \left| i \right\rangle \ . \end{aligned} \tag{2.23}$$

Here, $a_{i\to f}$ is the amplitude of the excitation, where $\Delta E = E_f - E_i$, with $E_{i(f)}$ the energy of the initial (final) state, and $V_C(\vec{r}(t))$ is the time-dependent Coulomb potential.

The reason for insisting that the minimum impact parameter be larger than two nuclear radii is clearly seen — the perturbation of the excitation amplitude depends explicitly on the assumption that the time-dependent Coulomb potential is the only non-negligible potential involved in the reaction. If this is the case, one can then expand the time-dependent Coulomb potential in terms of its multipole moments ($\mathcal{M}(\pi\lambda\mu)$) [40]:

$$\chi_{i\to f}^{\pi\lambda} \simeq \frac{Z_t e}{\hbar c b^{\lambda}} \left\langle f \right| \mathcal{M} \left(\pi\lambda\mu \right) \left| i \right\rangle \ . \tag{2.24}$$

As before, $\pi = E$ for electric transitions, $\pi = M$ for magnetic transitions, λ is the multipolarity of the transition, and μ is the projection of the multipolarity. The excitation amplitude

is summed over the entire expansion:

$$a_{i\to f} = i\sum_{\lambda} \chi^{\lambda}_{i\to f} f_{\lambda}\left(\xi\right) \ . \tag{2.25}$$

The function $f_{\lambda}(\xi)$ characterizes the adiabaticity of the reaction in terms of the adiabatic parameter ξ, which will be discussed in some detail subsequently.

Expanding the excitation amplitude, Alder and Winther obtain:

$$a_{i\to f} = -i\frac{Z_t e^2}{\hbar v\gamma}\sum_{\pi\lambda\mu} G_{\pi\lambda\mu}\left(\frac{c}{v}\right)(-1)^{\mu} K_{\mu}\left(\xi\left(b\right)\right)\sqrt{2\lambda+1}k^{\lambda}\frac{\langle J_f M_f|\,\mathcal{M}\left(\pi\lambda-\mu\right)|J_i M_i\rangle}{e} \ . \tag{2.26}$$

Here K_{μ} are modified Bessel functions of the second kind, $k = \Delta E/(\hbar c)$. $\mathcal{M}(\pi\lambda-\mu)$ are the multipole matrix elements for electric or magnetic excitation (give in [40]). The excitation strength functions, $G_{E\lambda\mu}$ and $G_{M\lambda\mu}$ are given (for $\mu \geq 0$) by:

$$\begin{aligned} G_{E\lambda\mu}\left(\frac{c}{v}\right) = {} & i^{\lambda+\mu}\frac{\sqrt{16\pi}}{\lambda(2\lambda+1)!!}\left(\frac{(\lambda-\mu)!}{(\lambda+\mu)!}\right)^{\frac{1}{2}}\left(\left(\frac{c}{v}\right)^2-1\right)^{-\frac{1}{2}} \\ & \times\left(\frac{(\lambda+1)(\lambda+\mu)}{2\lambda+1}P^{\mu}_{\lambda-1}\left(\frac{c}{v}\right)-\frac{\lambda(\lambda-\mu+1)}{2\lambda+1}P^{\mu}_{\lambda+1}\left(\frac{c}{v}\right)\right) \ . \end{aligned} \tag{2.27}$$

for electric excitations, where P^{μ}_{λ} are the associated Legendre polynomials. For magnetic excitations,

$$G_{M\lambda\mu}\left(\frac{c}{v}\right) = i^{\lambda+\mu+1}\frac{\sqrt{16\pi}}{\lambda(2\lambda+1)!!}\left(\frac{(\lambda-\mu)!}{(\lambda+\mu)!}\right)^{\frac{1}{2}}\left(\left(\frac{c}{v}\right)^2-1\right)^{-\frac{1}{2}}\mu P^{\mu}_{\lambda}\left(\frac{c}{v}\right) \tag{2.28}$$

The excitation functions for $\mu < 0$ are related to those for positive μ by:

$$G_{E\lambda-\mu} = (-)^{\mu} G_{E\lambda\mu}$$

$$G_{M\lambda-\mu} = -(-)^{\mu} G_{M\lambda\mu}$$

The integrated cross section is calculated by summing the excitation probability over all magnetic sub-states and integrating the result from the minimum impact parameter, b_{min}, to ∞:

$$\sigma_{i\to f} = 2\pi \int_{b_{min}}^{\infty} bdb \frac{1}{2j_i+1} \sum_{m_i,m_f} \left| a_{i\to f} \right|^2 \ . \tag{2.29}$$

Integrating over the range of impact parameters leads to:

$$\sigma_{i\to f} = \left(\frac{Z_t e^2}{\hbar c} \right)^2 \sum_{\pi\lambda\mu} k^{2(\lambda-1)} \frac{B\left(\pi\lambda; j_i \to j_f\right)}{e^2} \left| G_{\pi\lambda\mu}\left(\frac{c}{v}\right) \right|^2 g_{\mu}\left(\xi\left(b_{min}\right)\right) \tag{2.30}$$

The total cross section for intermediate-energy Coulomb excitation to a state is given by the sum of all of the allowed multipole components of the transition [38]:

$$\sigma_{i\to f} = \sum_{\pi\lambda} \sigma_{\pi\lambda} \ . \tag{2.31}$$

With $\sigma_{\pi\lambda}$ is given by [38]:

$$\sigma_{\pi\lambda} \approx \left(\frac{Z_p e^2}{\hbar c} \right)^2 \frac{\pi}{e^2 b_{min}^{2\lambda-2}} B(\pi\lambda; 0 \to \lambda) \begin{cases} (\lambda-1)^{-1} & : \text{for } \lambda \geq 2 \\ 2\ln(\rho_a / b_{min}) & : \text{for } \lambda = 1. \end{cases} \tag{2.32}$$

Here, ρ_a is the impact parameter corresponding to the adiabatic cutoff for intermediate-

energy Coulomb excitation:

$$\rho_a = \frac{\gamma\hbar c\beta}{E_\gamma}, \tag{2.33}$$

where E_γ is the excited state energy.

2.2.3.1 Adiabaticity of the Reaction

ξ is the *adiabatic parameter* and is proportional to the ratio of the time elapsed during the collision between the stationary target and the projectile moving past the target with velocity v_p ($\tau_{coll} = b/\gamma v_p$) and the characteristic time of the nuclear motion ($\tau_{nucl} = \hbar/\Delta E$) [40, 41]:

$$\xi(b) = \frac{\tau_{coll}}{\tau_{nucl}} = \frac{\Delta E}{\gamma\hbar v_p} b \ . \tag{2.34}$$

This expression of the adiabatic parameter highlights two assumptions of the Alder-Winther theory. The first is that the projectile travels on a straight-line trajectory past the target, while the second is that the projectile spends a time τ_{coll} in the electric field of the target. Esbensen [42] devised a more realistic model for Coulomb excitation, including distortions due to Coulomb effects to the straight-line trajectory in the calculation. At sufficiently high beam energies (within the energy regime used for this work) the results converge with the straight-line trajectory used in [40].

The impact parameter must be adjusted such that $b \rightarrow b + \frac{1}{2}\pi a_\circ$, because the half-distance of closest approach ($a_\circ$) is increased by Coulomb repulsion [40]. This re-scaling of the impact parameter is meant to account for the Coulomb distortion to the trajectory, which will cause the trajectory to deviate from a straight line. In this model the adiabaticity parameter is given by:

$$\xi(b) = \frac{\Delta E}{\hbar\gamma v_p}\left(b + \frac{\pi}{2}\frac{a_\circ}{\gamma}\right) \ . \tag{2.35}$$

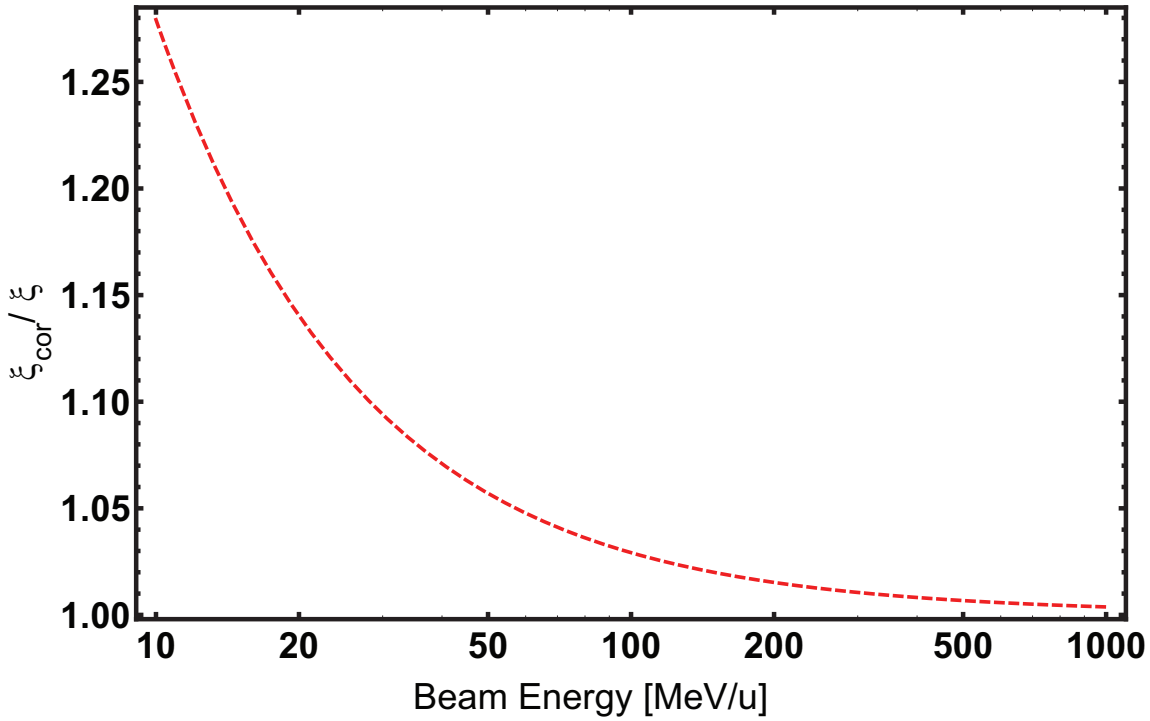

Figure 2.4: Comparison of the effect on the adiabatic parameter from the correction to the impact parameter for Coulomb repulsion.

As shown in Fig. 2.4, the effect of this correction is small for beam energies used in this work ($\approx$ 80 MeV/u). $\xi_{cor}/\xi \simeq 1.1 - 1.15$ in for these beam energies, suggesting that the assumption of the straight-line trajectory is valid.

The remaining function in the Coulomb excitation cross section (equation 2.30) is $g_\mu\left(\xi\left(b_{min}\right)\right)$, which measures the adiabaticity of the reaction and depends on the impact parameter, b_{min} (equation 2.22). Alder and Winther express g_μ as an integral of modified Bessel functions of the second kind, K_μ, over the impact parameter:

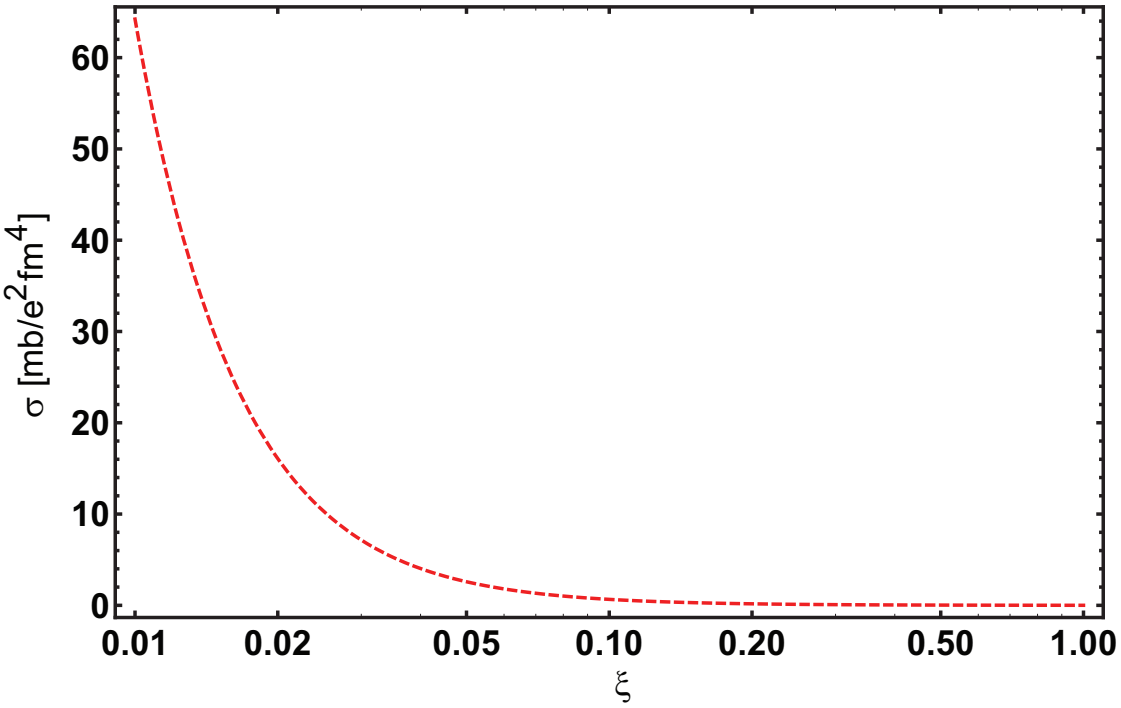

Figure 2.5: Total cross section as a function the adiabatic parameter, ξ. The calculation is for ^{40}Si at 80 MeV/u on ^{197}Au.

$$
\begin{aligned}
g_\mu\left(\xi\left(b_{min}\right)\right) &= 2\pi\left(\frac{E_f - E_i}{v\hbar\gamma}\right)^2 \int_{b_{min}}^{\infty} bdb\left|K_\mu\left(\xi\left(b\right)\right)\right|^2 \\
&= \pi\xi^2\left[\left|K_{\mu+1}\left(\xi\right)\right|^2 - \left|K_\mu\left(\xi\right)\right|^2 - \frac{2\mu}{\xi}K_{\mu+1}\left(\xi\right)K_\mu\left(\xi\right)\right] \qquad (2.36) \\
g_\mu &= g_{-\mu}
\end{aligned}
$$

as μ is the projection of the multipolarity, it runs in steps of 1 from $-\lambda$ to λ. Thus, for an $E2$ transition, one only need calculate $g_{0,1,2}$. Fig. 2.6 shows dependance of $g_{0,1,2}$ on ξ.

The crossing time between the target and projectile deceases with increasing beam energy, so the cross section for intermediate-energy Coulomb excitation is inversely proportional to the beam energy, as shown in Fig. 2.7.

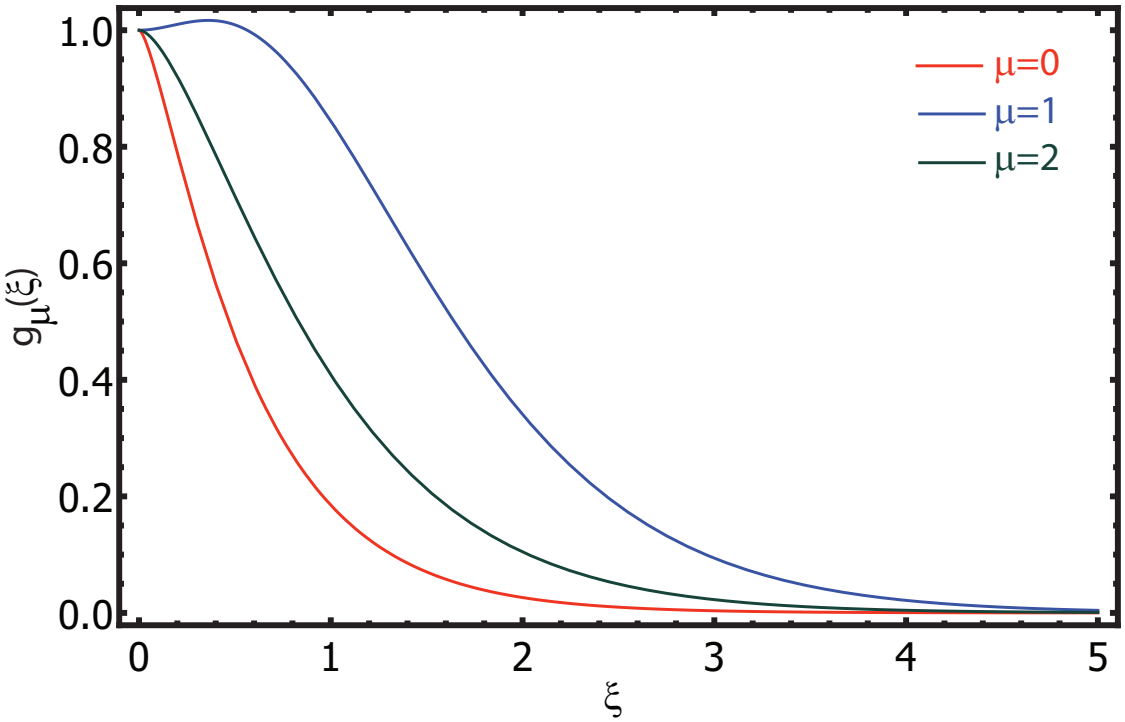

Figure 2.6: g_μ functions necessary to calculate the Coulomb excitation cross section for an $E2$ transition. The functions are normalized such that $g_\mu = 1$ for $\xi = 0$. Fig. after [40].

2.2.4 Intermediate-Energy Coulomb Excitation as a Probe of the $B(E2)$ Value

The accuracy of the Alder-Winther formulation of the excitation cross section in intermediate-energy Coulomb excitation as a probe of the $B(E2)$ value has been questioned by Bertulani *et al.* ([45]) who suggested that Coulomb distortion and retardation effects cause discrepancies on the order of 30% between the Alder-Winther theory and a formulation in which these effects are considered. However, Scheit *et al.* ([46]) point out that this discrepancy is due to a misunderstanding on the part of Bertulani *et al.* as to whether the scattering angle presented in the experimental papers cited in [45] were in the center of mass or laboratory frame. In addition, Bertulani *et al.* use the incident beam energy rather than the half-target beam energy in the calculation Coulomb excitation cross section. When the correct val-

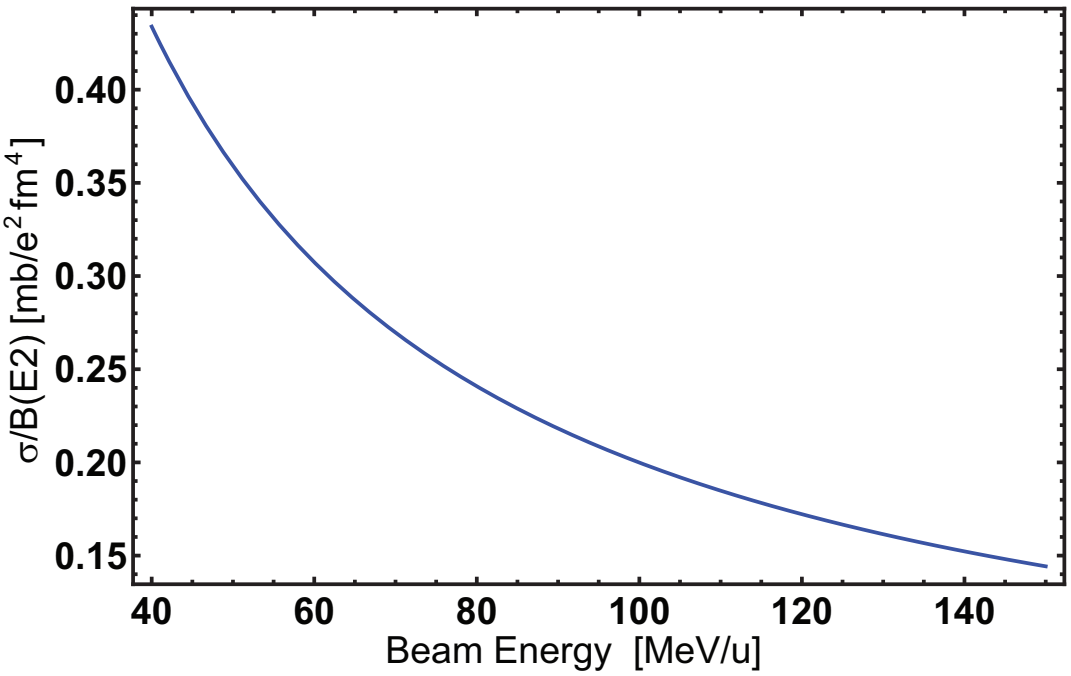

Figure 2.7: Intermediate-energy Coulomb excitation excitation cross section, $\sigma_{0^+\to 2^+}$, as a function of beam energy. The calculation is for ^{40}Si on ^{197}Au (recall that the cross section for an electric quadrupole transition is directly proportional to the $B(E2)$ value for a given scattering angle) and $E_\gamma \simeq 1$ MeV.

ues are used, Scheit *et al.* found excellent agreement between the Alder-Winther theory of Coulomb excitation and the formulation presented by Bertulani *et al.*. Subsequent papers by Esbensen [42] and by Kumar *et al.* [47] agree.

However, Scheit *et al.* agree with Bertulani *et al.* that a fully relativistic approach to Coulomb excitation, which does not make the approximation of a straight-line trajectory, is likely necessary for high-precision Coulomb excitation experiments (such an approach is presented by Esbensen [42]) but suggest that uncertainties introduced by these approximations are not likely to affect the current ensemble of data from lower precision, statistics-limited Coulomb excitation experiments with exotic nuclei.

From an experimental perspective, the current generation of intermediate-energy Coulomb excitation experiments agree quite well with other probes. Cook *et al.* [48] compared the $B(E2)$ values obtained from intermediate-energy Coulomb excitation with those obtained from other probes for eight different nuclei and found excellent agreement between the value obtained from intermediate-energy Coulomb excitation and the adopted value, as shown in Fig. 2.8.

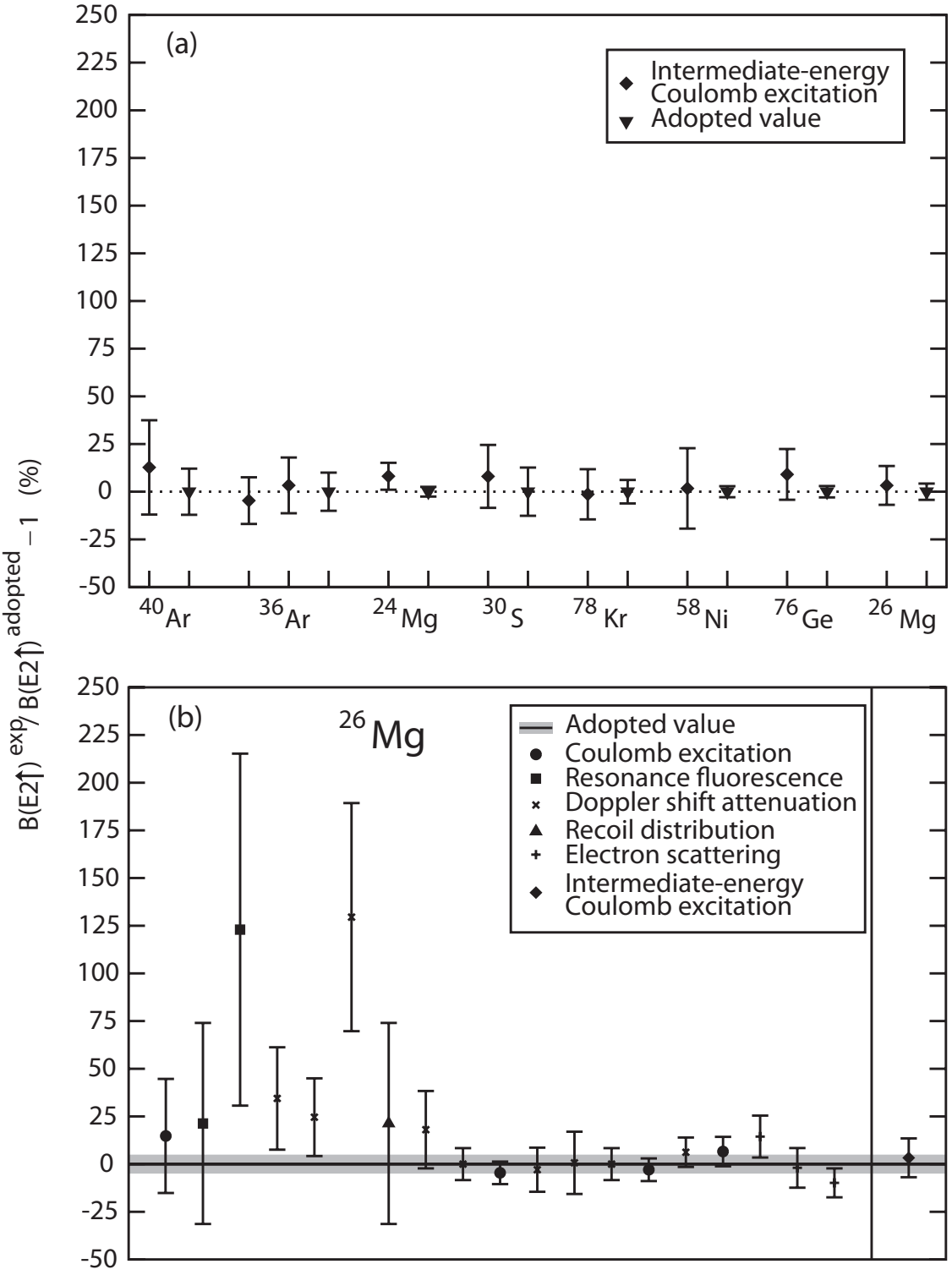

Figure 2.8: Panel (a): Comparison of the adopted $B(E2)$ value and that obtained from intermediate-energy Coulomb excitation. Panel (b): Comparison of the $B(E2)$ for ^{26}Mg obtained from intermediate-energy Coulomb excitation and other probes. See [48] for the sources of the values plotted in this figure.

Chapter 3

Experimental Apparatus

As discussed in the first chapter, the experiments which provide the most stringent tests of nuclear models typically study nuclei which do not exist in nature and have to be produced artificially. At NSCL, these nuclei are produced by fast fragmentation. In this process, a stable beam (called the primary beam) is accelerated to a velocity of about 50% of the speed of light and impinged on a thick target, usually made of ^{9}Be. The products of the fragmentation reaction are separated according to their mass and charge by a $B\rho-\Delta E-B\rho$ method and a particular species of nuclei (called the secondary beam) or an ensemble of nuclear species (a secondary cocktail beam) are selected from all the produced fragments.

The nucleus of interest is transmitted to an experimental station where its reaction with a target can be studied. In intermediate-energy Coulomb excitation, the nucleus of interest is produced in the fragmentation of the primary beam, selected by the A1900 Fragment Separator ([51, 52]), transported to an experimental station (in this work, the S800 Spectrograph [53]), and focused at a secondary, high-Z target. If the projectiles are excited by the target (or vice versa), the excited state will decay and emit a de-excitation γ-ray, which has a chance of being detected by the high-efficiency scintillator array (CAESAR, [54]) po-

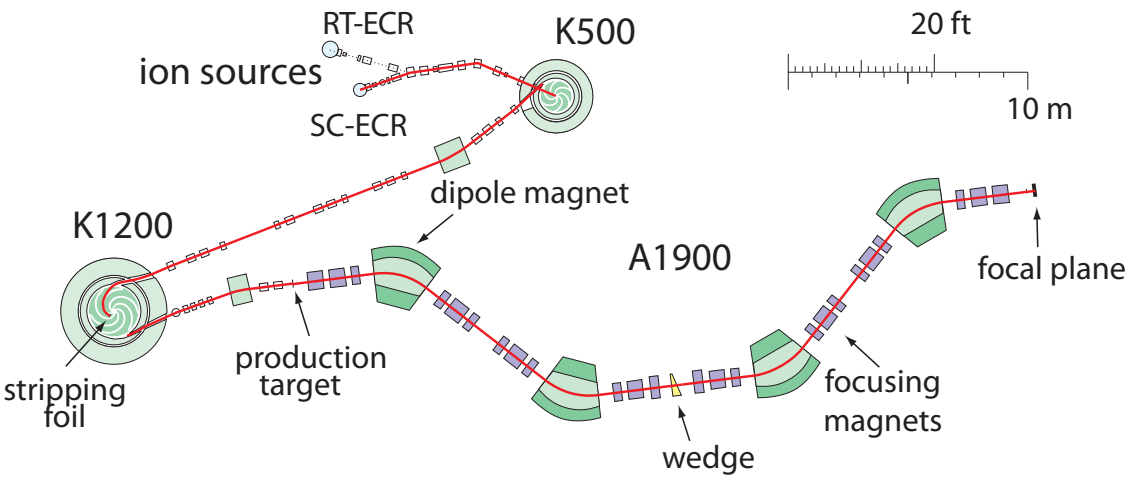

Figure 3.1: A schematic of the Coupled Cyclotron Facility at NSCL. The central path of the beam, from an ion source to the cyclotrons to the A1900 Fragment Separator is highlighted in red. Figure is modified from [69].

sitioned around the secondary excitation target. The reaction products are detected on an event-by-event basis by the focal plane detector system of the S800 Spectrograph [55]. All of these systems will be discussed in some detail in this chapter.

3.1 Beam Production

A stable beam is prepared by ionizing the atoms of a stable isotope in an electron cyclotron resonance (ECR) ion source, injecting the (usually singly- or doubly-) ionized isotope into the K500 cyclotron, accelerating it to $\simeq$15% of the speed of light, and injecting it into the K1200 cyclotron where it is further stripped and accelerated to about 50% of the speed of light. The accelerated and stripped[1] primary beam is impinged on a thick production target, usually ^{9}Be. The resulting nuclei produced by the fragmentation of the primary beam are filtered by the A1900 Fragment Separator, which is tuned to select the isotope of interest. This isotope is transmitted to an experimental station for measurement. A schematic of the

[1]The ^{48}Ca primary beams used in this work were fully stripped, but it is not possible to fully strip much heavier beams at NSCL energies, see [49].

devices involved in this process is shown in Fig. 3.1.

3.1.1 Primary Beam Preparation

The production of a primary beam begins in an ion source (see Fig. 3.1). If the atom used to produce the primary beam is not gaseous, it is heated in an oven until it vaporizes and then the plasma is injected into a magnetic bottle inside the ion source. The ^{48}Ca primary beam used for all the experiments discussed in this work was prepared from a solid block of metallic ^{48}Ca. Once the gas is in the ion source, it is bombarded by electrons, which are accelerated by microwave radiation. The resonant frequency (ω) of the cavity is given by:

$$\omega = \frac{eB}{m_e} \ , \tag{3.1}$$

where e is the electron charge, B is the applied magnetic field and m_e is the rest mass of an electron. The electrons collide with the atoms in the gas and ionize the atoms. The ionized gas is injected into the K500 cyclotron by the application of a bias voltage. The ECR ion source method produces beams that are doubly or singly ionized, so further ionization is accomplished by means of a carbon "stripper foil" placed in the middle of the K1200 cyclotron. Each time the beam passes through the stripper foil it can become more highly ionized.

The K500 and K1200 cyclotrons take advantage of the fact that the radius of curvature ρ for the path of a particle with charge q and mass m moving with a velocity of v in a magnetic field of strength B is:

$$\rho = \frac{\gamma m v}{qB} \ . \tag{3.2}$$

Any increase in the velocity or in mass will increase the radius of curvature of the particle's path. The K500 and K1200 cyclotrons apply a magnetic field strong enough to constrain particles to move in a circle (between 3-5 Tesla). Each cyclotron has 3 "dees" and three "hills" (see Fig. 3.2). A strong RF field is applied across the gap each time the beam traverses the gap between the dee and the hill. The momentum (p) of the particle is given by:

$$p = m\gamma\beta c \ . \tag{3.3}$$

It is common to refer to the *magnetic rigidity* or simply *rigidity* of the beam as (re-arranging Eq. 3.2):

$$B\rho = \frac{p}{q} = \frac{\gamma\beta mc}{q}, \tag{3.4}$$

The ^{48}Ca primary beams used for this work were produced at an energy of 140 MeV/u and an intensity of 80 particle-nano Amps (about 5×10^{11} particles per second). The intensity of the primary beam is measured sporadically by a Faraday cup after extraction.

3.1.2 Secondary Beam Selection

Once the primary beam has been accelerated to the desired energy, it is extracted from the K1200 cyclotron and impinged on a thick ^{9}Be production target. The primary beam is selected based on the probability of producing the isotope of interest in fragmentation, commonly through the use of the LISE++ program [56], which simulates the fragmentation reaction and subsequent isotopic selection in the A1900 Fragment Separator. The maximum magnetic rigidity of the devices is 6 Tm and the maximum rigidity of the secondary beams used in this work was ≈ 4.04 Tm.

The A1900 Fragment Separator is composed of 44 magnetic elements, four 45° dipole

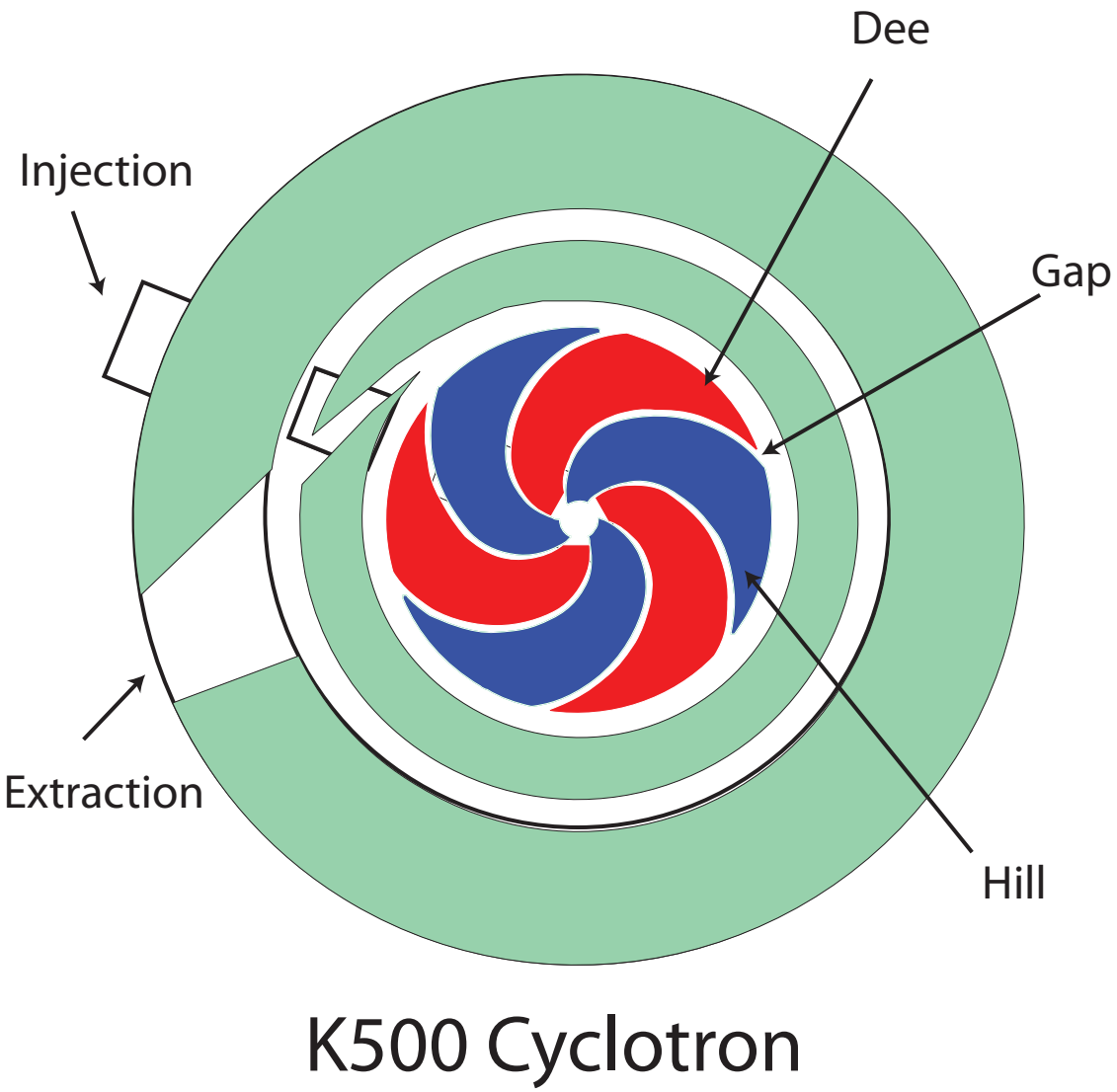

Figure 3.2: A schematic of the K500 cyclotron. The dees are shown in red, the hills in blue. An accelerating voltage is applied between the dee and the hill, so each time the ionized beam crosses this gap it is accelerated. Figure is modified from [69].

bending magnets and 40 large-diameter multipole focusing magnets [51, 52]. The dipole magnets disperse the beam according to its rigidity (see Eq. 3.4). The magnetic field can be tuned to select the mass-to-charge ratio of the particle of interest. The multipole focusing magnets located after the dipole magnets re-focus the beam after dispersion.

Unambiguous particle selection cannot be accomplished by mass-to-charge selection alone; particles with the same ratio and velocity will not be spatially separated by the dipole magnets. For this reason, an aluminum or Kapton "wedge"[2] is inserted at the mid-acceptance position of the A1900 (see Fig. 3.1). Particles moving through material lose energy through interactions with the electrons in the material. This energy loss is described by the *Bethe formula* [58]:

$$-\frac{dE}{dx} = \frac{4\pi e^4 Z_p^2}{m_e v^2} N Z_t \left[\ln\left(\frac{2m_e v^2}{I}\right) - \ln\left(1 - \frac{v^2}{c^2}\right) - \frac{v^2}{c^2} \right] . \tag{3.5}$$

The distance the beam travels through the material is represented by x, N, I, and Z_t are respectively the number density, mean excitation potential, and the atomic number of the absorbing material. Z_p is the atomic number of the projectile, e is the electron charge, and m_e is the electron rest mass. The energy loss is thus proportional to the square of the atomic number of the beam: $dE/dx \propto Z_p^2$, so the fragments lose energy in the wedge depending on their atomic number, allowing the two remaining dipoles to select the species of interest. A thin plastic scintillator is located at the focal plane of the A1900. This scintillator is used in conjunction with a downstream scintillator to measure the time-of-flight of the particles in the beam on an event-by-event basis. The time-of-flight depends on the momentum of a particle and, together with the measured energy loss of the particle allows an unambiguous

[2] the nomenclature is somewhat misleading — the "wedge" actually has a curved profile, so that the A1900 Fragment Separator is achromatic [57].

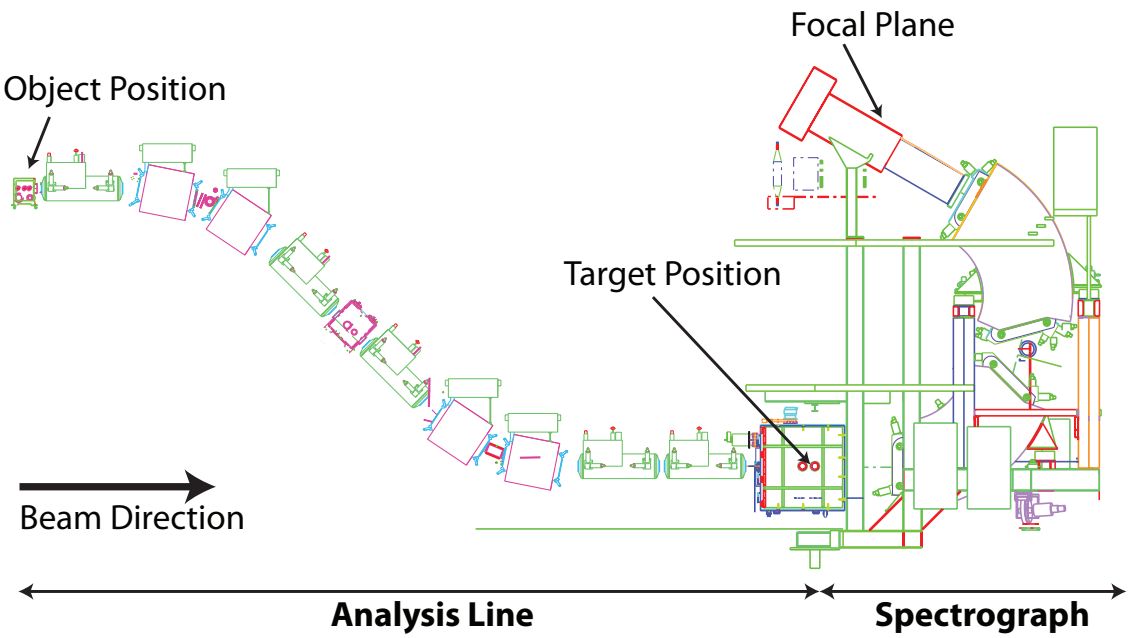

Figure 3.3: A schematic of the S800 Spectrograph showing the location of the object and target positions and the focal plane. Figure from [59].

A, Z identification for each particle. The beam is then directed onto the intermediate-energy Coulomb excitation target, located at the target position of the S800 Spectrograph.

3.2 The S800 Spectrograph - Particle Detection

The S800 Spectrograph is a high-resolution, high-acceptance spectrograph, composed of the analysis line and the spectrograph (see Fig. 3.3). The analysis line is used to tune the beam to the target and to characterize the incoming beam. The maximum rigidity of the analysis line is 4.9 Tm [53]. The spectrograph is used to direct the reaction products to the focal plane, where the position, energy loss, and time-of-flight of each particle are measured. The angular acceptance of the spectrograph is about $\pm 5^{\circ}$ in the non-dispersive direction and $\pm 3.5^{\circ}$ in the dispersive direction, amounting to a solid angle coverage of about 20 msr [55]. The energy resolution of the spectrograph is about $\Delta E/E \approx 10^{-3}$ [60].

The beam incoming from the A1900 is focused at the object position, where a thin plastic scintillator (typically 125 μm thick) is located for time-of-flight measurements. The analysis line was operated in the achromatic "focused mode" for this work, so the beam was focused at the target position and dispersed in the x direction at the focal plane. In focused mode, the beam spot on the target is quite small, so the momentum acceptance of the A1900 can be as large as $\Delta p/p = \pm\ 2\%$. The analysis line can also be operated in "dispersion matched" mode, in which the beam is dispersed at the target position according to its momentum, as discussed in [60].

A high-Z target for intermediate-energy Coulomb excitation was located at the target position of the S800. The target is followed by a quadrupole focusing doublet, to re-focus the beam in x and y after interacting with the target, and by two dipole magnets which disperse the components of the beam according to their mass-to-charge ratio (see Sec. 3.1.2). The magnets after the target are tuned to select the experimental reaction channel of interest, typically by calculating the rigidity of the nucleus of interest after the target (e.g. ^{34}Si with an energy of $\approx$ 84 MeV/u before the 518 mg/cm^2 thick ^{197}Au target will have an energy of $\approx$ 76 MeV/u after the target, so the rigidity of the S800 will be set to $\approx$ 3.11 Tm). The maximum rigidity of the spectrograph is 4 Tm. The beam is directed up to the S800 focal plane, where an ensemble of detectors measure its position, time-of-flight and energy loss on an event-by-event basis.

3.2.1 The S800 Focal Plane

The S800 focal plane contains a number of detectors (see Fig. 3.4) which are used to obtain information about the reaction at the target position [55]. First, the reaction product passes through two Cathode Readout Drift Chambers (CRDCs), spaced a meter apart, which mea-

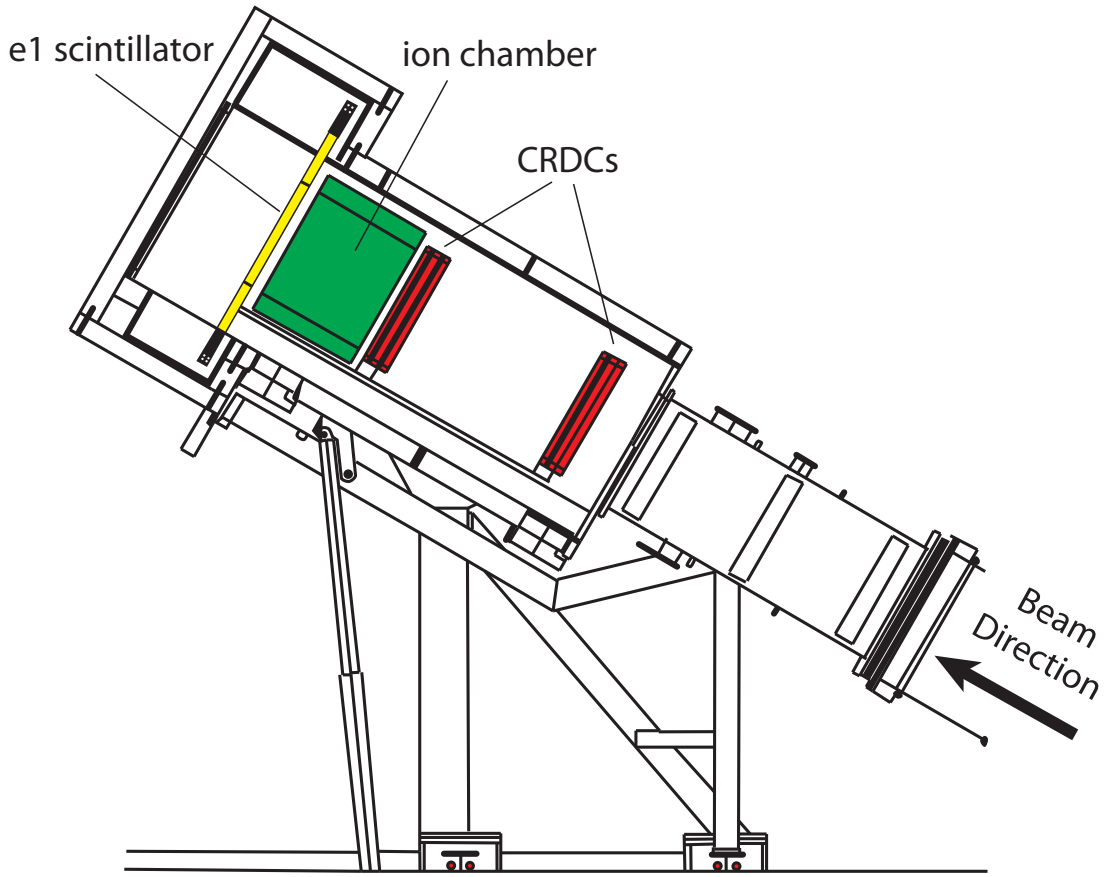

Figure 3.4: Schematic of the S800 focal plane showing the detectors used in this work. Figure is courtesy of S. McDaniel [61].

sure the x and y position of the particle (see Fig. 3.4 and Fig. 3.5). The positions measured in the CRCDs are used to determine the particle's trajectory, which is then used to reconstruct the scattering angle at the target. The reaction product then passes through an ionization chamber, which measures energy loss in order to determine the atomic number of the reaction product, as discussed in Sec. 3.1.2. The reaction product finally passes through a thin plastic scintillator (the "e1 scintillator") which provides a time-of-flight signal relative to other timing detectors upstream and triggers the data acquisition for S800 events. The measurements made in the focal plane detectors of the S800 provide unambiguous identification of the particle by its atomic number and mass.

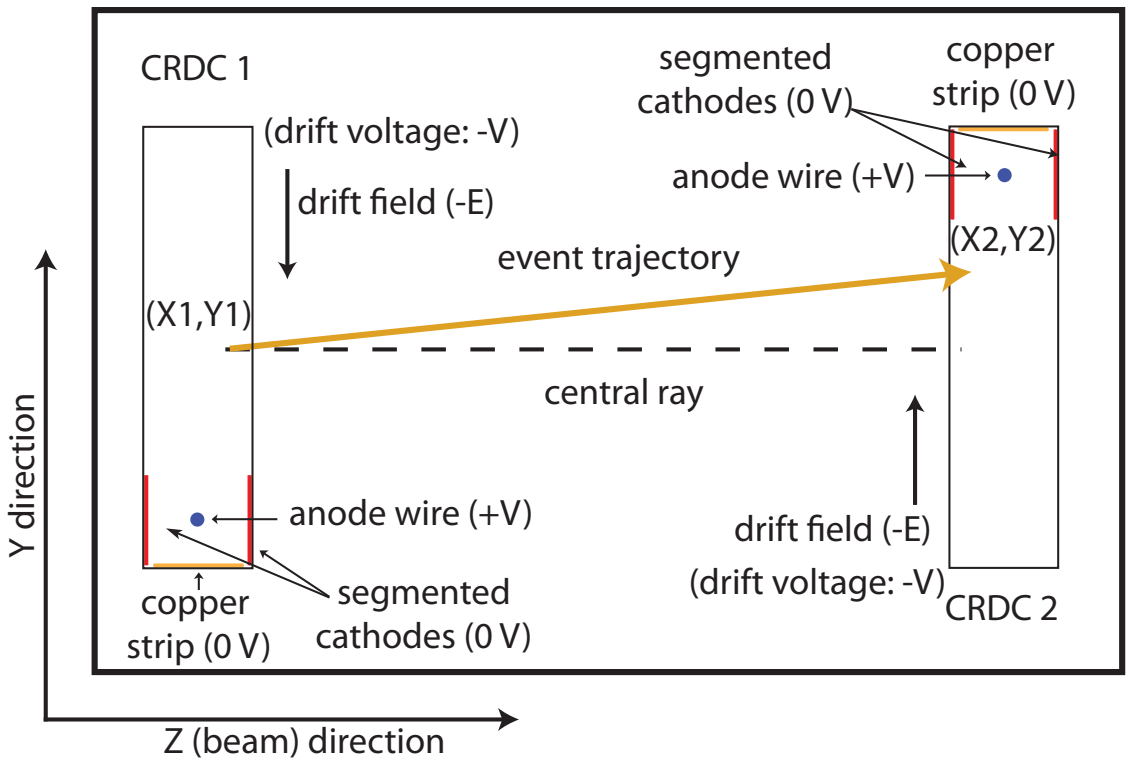

Figure 3.5: Schematic of the CRDCs in the S800 focal plane (not to scale). The y and z directions are as indicated in the figure, the x direction is out of the page. The trajectory of a particle is indicated by the yellow arrow, the central trajectory by the dashed line. The components of the CRDC which are used to determine the y position (the anode wire) and the x position (the segmented cathode) are indicated.

3.2.1.1 Cathode Readout Drift Counters - Position and Tracking

As discussed in Sec. 2.2.3, the nuclear contribution to the intermediate-energy Coulomb excitation cross section is negligible if the impact parameter is larger than two nuclear radii + 2 fm (see Eq. 2.22). As Eq. 2.20 shows, the minimum impact parameter is related to a maximum scattering angle. The scattering angle is calculated on an event-by-event basis by measuring the (x,y) position of particles in the CRDCs, located in the focal plane of the S800, and reconstructing the trajectory of each particle back to the target.

Each CRDC has a position resolution of about 0.5 mm in the dispersive and non-dispersive directions [60]. These detectors are 56 cm in the x (dispersive) direction by

26 cm in the y (non-dispersive) direction, with an active depth of 1.5 cm [55]. The CRDCS are filled with a gas mixture of 20% isobutane and 80% carbon tetrafluoride at a pressure of 50 Torr [60]. A negative bias voltage (called the *drift voltage*) is applied across the CRDC in the y direction. The fill gas is ionized by a projectile and the ionization electrons drift towards the anode wire, which is held at a positive voltage, where they are collected.

The anode wire is bordered by a cathode, which is segmented into 224 pads, each 2.54 mm wide [55]. The charge drifting toward the anode wire induces image charges on the cathode pads. The position of an interaction in the dispersive (x) direction is determined by fitting a Gaussian distribution to the measured charge deposition on the pads. The x position is then taken to be that of the pad most closely matching the centroid of the Gaussian distribution.

The y-position of the interaction between a projectile and the fill gas is calculated from the drift time of the electrons to the anode wire by measuring the difference in time between the signal from the anode wire and the signal from the e1 scintillator. The drift time (typically 0-20 μs [62]) depends on the distance between the ionization electrons and the anode wire, the drift voltage, and the condition of the fill gas. The CRDCs must be calibrated during the experiment. This is done by inserting thick tungsten masks with known (x,y) positions in front of each CRDC (Fig. 3.6 shows a typical spectrum taken for such a calibration). The drift time is calibrated by a linear fit of the measured position of the holes in the mask to their known positions. As the experiment progresses, the drift time can shift due to changes in the pressure, temperature, or composition of the fill gas. For this reason, mask calibrations were taken periodically during the measurements discussed in this work. The slope of the linear function obtained from the mask calibration was adjusted on a run-by-run basis (each run was about 30 minutes long) to shift the centroid of the measured CRDC drift time spectrum for each run to that of a reference run. A comparison of run-by-run corrected

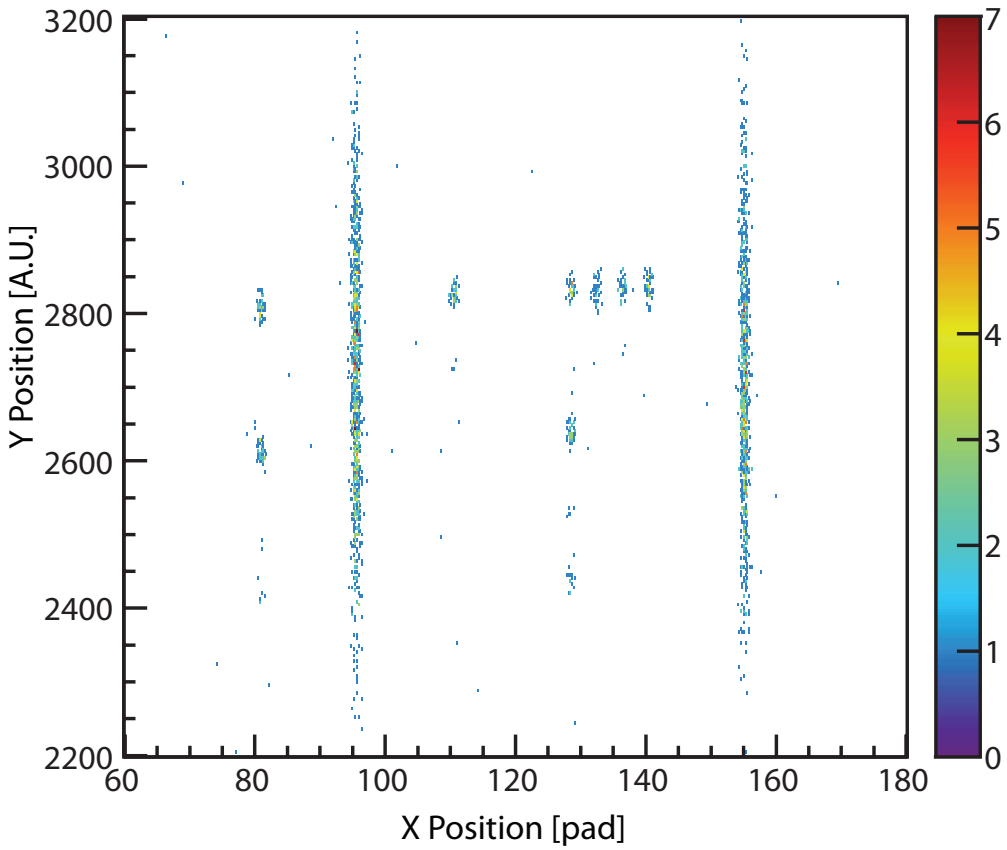

Figure 3.6: Mask calibration from the ^{40}Si data set. The matrix shown was taken with the tungsten mask inserted in front of CRDC 1. The localized intensities correspond to holes and slits in the mask.

and un-corrected CRDC y spectra is shown in Fig. 3.7.

The CRDCs begin to lose efficiency for beam rates above about 5,000 particles per second (pps) and high beam rates can damage the CRDCs [53]. If necessary, the primary beam is attenuated to ensure that the number of particles incident on the CRDCs does not exceed this limit.

3.2.1.2 Trajectory Reconstruction in the S800

Because the S800 Spectrograph is a high-acceptance device, particles with different combinations of momentum and trajectory will reach the focal plane. The time-of-flight of these

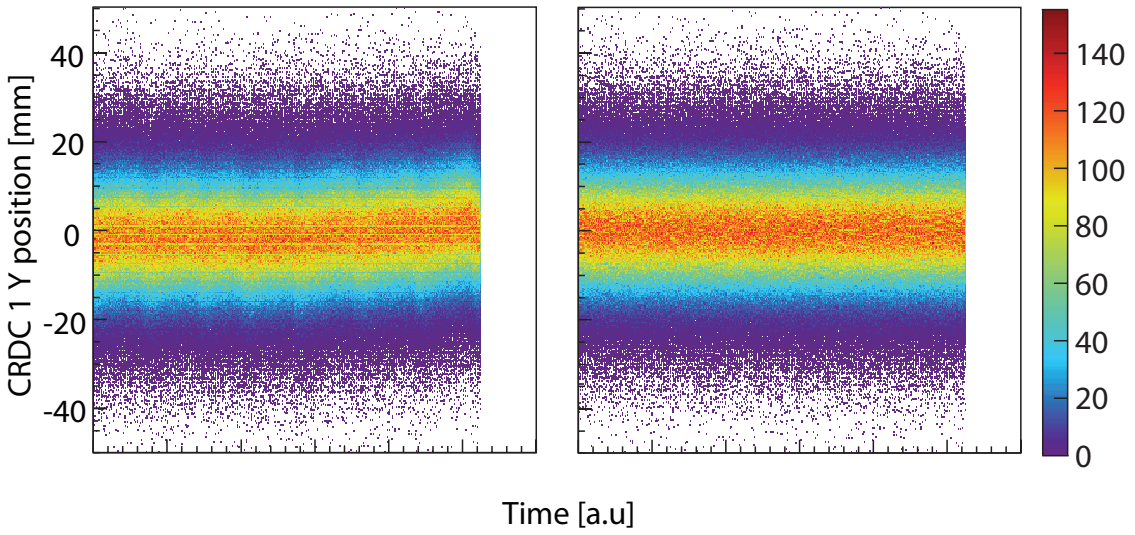

Figure 3.7: CRDC 1 y position (extracted from the drift time) plotted versus elapsed time. The plot on the left is obtained with a fixed mask calibration taken in the beginning of the measurement, the plot on the right was obtained by including run-by-run corrections to the drift time to accommodate the changes in the drift time over the measurement. The data shown here are from the ^{40}Si data set and represent about 38 hours of beam incident on the CRDCs.

particles will vary, so in order to determine the scattering angle of each particle at the target position it is necessary to first reconstruct the particle's trajectory. This is accomplished by calculating the position and angle of the particle in the focal plane and using an ion optics code (COSY Infinity [63]) to reconstruct the trajectory of the particle through the spectrograph back to the target.

Once the (x,y) positions in each CRDC have been obtained they can be used to calculate angles in the focal plane. The dispersive and non-dispersive angles are, respectively:

$$\begin{aligned} a_{fp} &= \text{ArcTan}\left[\frac{crdc2.x - crdc1.x}{gap}\right] \\ b_{fp} &= \text{ArcTan}\left[\frac{crdc2.y - crdc1.y}{gap}\right], \end{aligned} \tag{3.6}$$

where $gap = 1000$ millimeters and the $crdc.1(2).x(y)$ positions are measured in millimeters.

The positions are given by:

$$\begin{aligned} x_{fp} &= \frac{crdc1.x}{gap} \\ y_{fp} &= \frac{crdc1.y}{gap} \ , \end{aligned} \tag{3.7}$$

The positions and angles at the target are reconstructed by means of an inverse map ($\mathcal{S}^{-1}$) produced by COSY Infinity, which relates the positions measured and angles calculated at the focal plane to positions at the target by the matrix equation [62]:

$$\begin{pmatrix} a_{ta} \\ y_{ta} \\ b_{ta} \\ d_{ta} \end{pmatrix} = \mathcal{S}^{-1} \begin{pmatrix} x_{fp} \\ a_{fp} \\ y_{fp} \\ b_{fp} \end{pmatrix} \ . \tag{3.8}$$

Here a_{ta} and b_{ta} are the dispersive and non-dispersive angles reconstructed at the target, respectively. The reconstructed y position at the target is given by y_{ta} and d_{ta} is the fractional deviation in kinetic energy of the particle (E) from the expected kinetic energy of the same particle taking the central path through the spectrograph (E_0): $d_{ta} = (E - E_0)/E_0$.

The calculation of these inverse maps has been automated. The necessary inputs are the currents supplied to the magnets in the spectrograph, the magnetic rigidity of the spectrograph, the mass and charge of the particle of interest and the shift in focus at the target and in the focal plane (if any).

Then the dispersive and non-dispersive angles reconstructed at the target are used to calculate the laboratory scattering angle (θ) in milliradians:

$$\theta = \mathrm{ArcSin}\left[\sqrt{\mathrm{Sin}^2\left(a_{ta}\right) + \mathrm{Sin}^2\left(b_{ta}\right)}\right] \tag{3.9}$$

$\mathrm{Sin}(a_{ta})$	$\mathrm{Sin}(b_{ta})$	ϕ
> 0	> 0	$\mathrm{ArcTan}\left[\frac{\sin(a_{ta})}{\sin(b_{ta})}\right]$
< 0	> 0	π - $\mathrm{ArcTan}\left[\frac{\sin(a_{ta})}{\lvert\sin(b_{ta})\rvert}\right]$
> 0	< 0	2π - $\mathrm{ArcTan}\left[\frac{\lvert\sin(a_{ta})\rvert}{\sin(b_{ta})}\right]$
$= 0$	$= 0$	0

Table 3.1: The value of the azimuthal scattering angle depends on the sine of the dispersive and non-dispersive angle. The azimuthal scattering angle is calculated in radians.

The calculation of the azimuthal scattering angle is a little more complicated, as shown in Tab. 3.1.

3.2.1.3 The Ionization Chamber - Energy Loss for Particle Identification

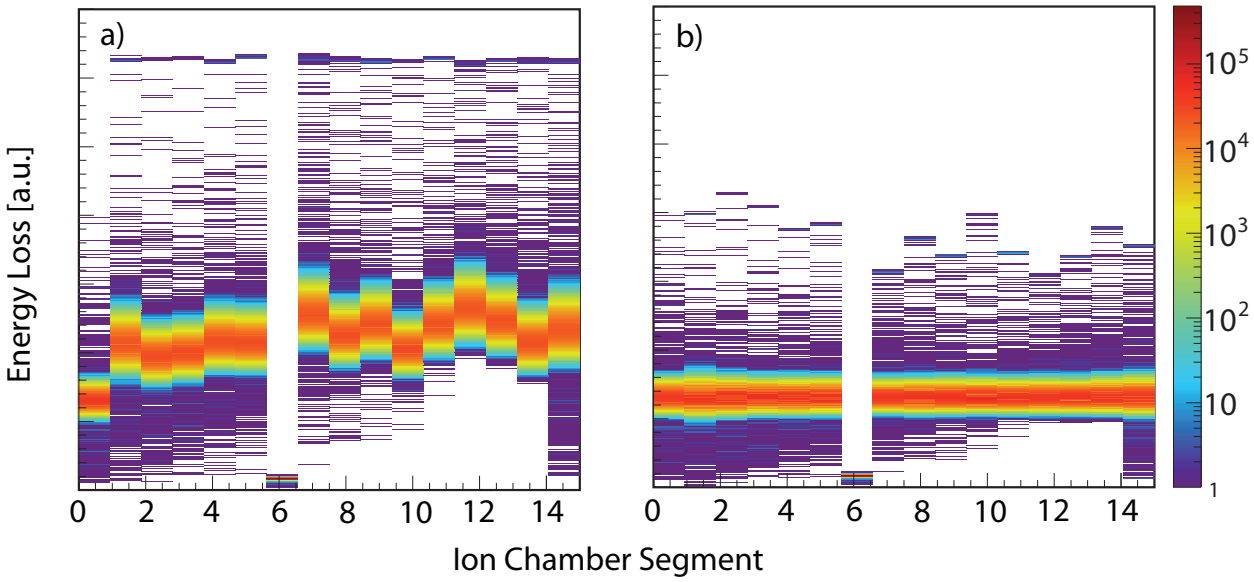

Figure 3.8: Plots of the un-calibrated (panel a) and calibrated (panel b) energy-loss measured in the ionization chamber are shown as a function of the ionization chamber segment measuring the energy loss. Segment 6 was malfunctioning, it was turned off and omitted from the analysis. The data shown are from the ^{40}Si data set.

An ionization chamber is located in the focal plane of the S800 to measure energy loss of the reacted beam [55]. The ionization chamber is 16 inches long and is segmented into

16 one-inch anodes, with anode one most downstream and anode 16 most upstream. The ionization chamber is filled with a mixture of 90% argon and 10% methane gas (a standard mixture called "P10") at a pressure of 140 Torr. The traversing particle creates electron-ion pairs in the gas, the positively charged ions of the fill gas are collected on the cathode while the electrons are collected on the anodes. The energy loss of a particle moving through material is related to the square of the charge of the particle (Eq. 3.5), so measuring the energy deposited by the particle allows the atomic number of the particle to be determined.

The energy loss spectrum measured in the first segment of the ionization chamber is used as a reference and the energy loss spectra measured in the successive segments of the ionization chamber are aligned with that of the first segment by a linear function. Fig. 3.8 shows the results of such an alignment procedure for the ^{40}Si data set. Segment six was malfunctioning during the first experiment, so it was turned off and omitted from the analysis of the Coulomb excitation of $^{34-40}$Si. The ion chamber described was replaced prior to the experiment measuring the Coulomb excitation of ^{42}Si with one segmented into 32 cathode-anode pairs (16 of each), which ran perpendicular to the direction of the beam. This ionization chamber is much faster than the one used in the intermediate-energy Coulomb excitation of $^{34-40}$Si, as the electrons and ionized fill gas have to drift a much shorter distance before being collected.

The total energy lost in the ionization chamber ($ic.sum$) is calculated to be the sum of the energy lost in each of the aligned segments ($ic.cal.i$) in the ionization chamber:

$$ic.sum = \sum_{i=1}^{16} ic.cal.i \tag{3.10}$$

3.2.1.4 The E1 Scintillator - Time of Flight and Triggering

Downstream of the ionization chamber there is a large area (30×59 cm) thin (3 mm thick) plastic scintillator [60] which measures the time of flight difference with respect to an upstream scintillator. The e1 scintillator has photomultiplier tubes positioned at the top and bottom, which give energy, position and timing information for a particle. In this analysis the e1 scintillator was only used to provide timing information and the trigger for events in the S800 focal plane.

3.3 Gamma-ray Detection

One important decay mode for reaction products created in an excited state by a nuclear reaction in the target is the emission of γ rays. For example, in the intermediate-energy Coulomb excitation experiments discussed in this work, the incoming even-even nuclei of interest were excited from the 0^+ ground state to the first 2^+ state and emitted a prompt de-excitation γ ray with energy characteristic of the excited state. For some cases, the number of de-excitation γ rays emitted was quite low, depending on the secondary beam rate and the cross section for the reaction of interest. In addition, the velocity of the secondary beam particles was between 0.3 and 0.4 c, meaning that the energy of the de-excitation γ rays (which is fixed in the rest frame of the particle) is detected with an angle-dependent Doppler-shift in the laboratory frame. These conditions demand a γ-ray spectrometer with optimized detection efficiency and a sufficient granularity for reconstructing the Doppler-shifted γ-ray energies back into the projectile's rest frame.

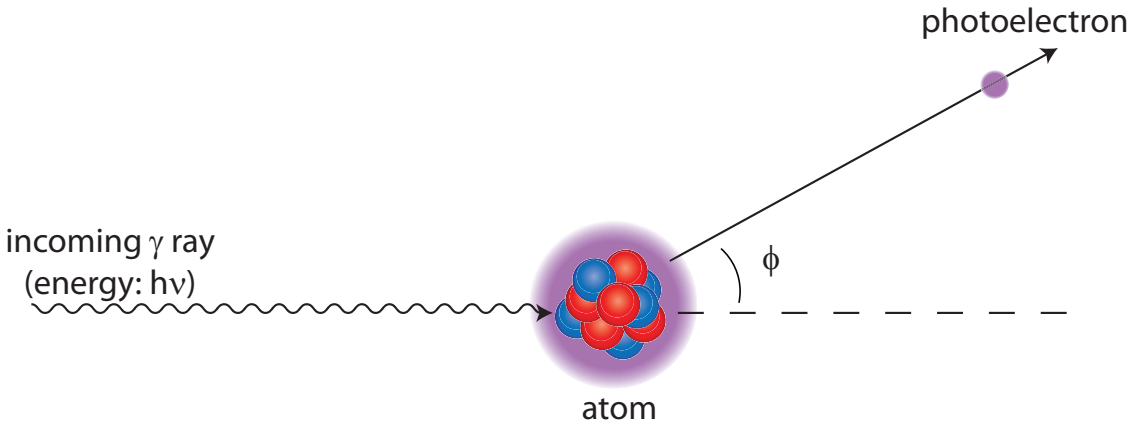

Figure 3.9: Schematic description of the photoelectric effect. A γ ray incident from the left knocks an electron from the atomic shell. The relative sizes of the nucleus and the atom are not drawn to scale. Figure after [58].

3.3.1 Interaction of Gamma-Rays with Matter

The γ rays with energies of interest in a γ-ray spectroscopy experiment interact with the detector material via the photoelectric effect, Compton scattering or pair production. These interaction channels depend both on the energy of the γ ray and the atomic number of the absorbing material.

3.3.1.1 The Photoelectric Effect

The photoelectric effect is the primary interaction channel for γ rays with energy between 10 keV and 500 keV for the detector material used in this work (see Fig. 2.20 of [58]). If a γ ray interacts with matter via the photoelectric effect, the γ ray is completely absorbed by an atom in the material (see Fig. 3.9), which emits a *photoelectron* with energy E_{e^-}:

$$E_{e^-} = E_\gamma - E_b \ , \tag{3.11}$$

where E_b is the binding energy of the atomic shell from which the electron was ejected. The probability per atom for absorption via the photoelectric effect can be approximated as [58]:

$$\tau \approx const \frac{Z^n}{E_\gamma^{3.5}} \tag{3.12}$$

the value of n depends on the γ-ray energy and increases from about 4 at 100 keV to 4.6 at 3 MeV [64].

3.3.1.2 Compton Scattering

In Compton scattering, a γ ray carrying energy E_γ elastically scatters off a quasi-free electron in the absorbing material, imparting some of its energy to the *recoil electron* and continuing to propagate as a scattered γ ray carrying energy E'_γ:

$$\frac{1}{E'_\gamma} - \frac{1}{E_\gamma} = \frac{1}{m_e c^2} \left(1 - \cos\theta\right). \tag{3.13}$$

The process is shown in Fig. 3.10, with the scattering angle of the γ ray given by θ.

The energy deposited in the absorbing material from a Compton-scattered γ ray is at a minimum of $E'_\gamma = 0$ MeV when the scattering angle $\theta = 0^\circ$ and varies continuously up to a maximum energy. These highest-energy Compton-scattered γ rays scatter with an angle of $\theta = 180^\circ$ and are said to form the *Compton edge* of the γ-ray spectrum. Evaluating Eq. 3.13 at $\theta = 180^\circ$ gives the energies of the highest-energy scattered γ rays as:

$$E'_\gamma(180^\circ) = E_{CE} = \frac{E_\gamma}{1 + \frac{2E_\gamma}{m_e c^2}}. \tag{3.14}$$

Compton-scattered γ rays with scattering angles $0^\circ \leq \theta \leq 180^\circ$ have energy between 0

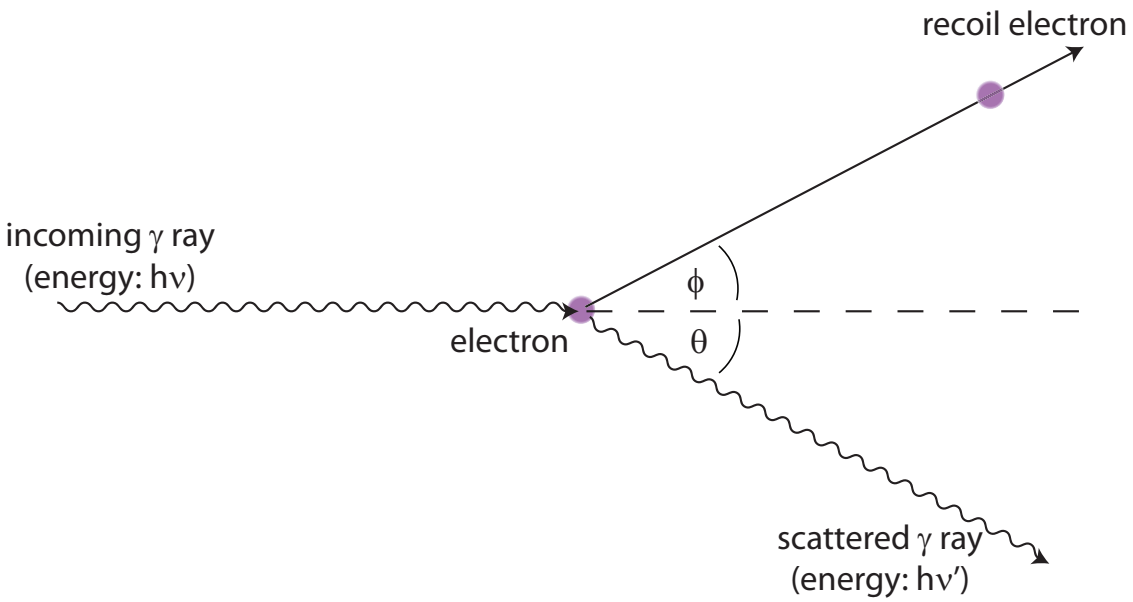

Figure 3.10: Schematic description of Compton scattering. The γ ray is incident from the left. Figure after [58].

and E_{CE} MeV. These γ rays form the *Compton Plateau* or *Compton Continuum* in the characteristic spectrum measured with a γ-ray detector, illustrated in Fig. 3.12.

A γ ray can Compton scatter, imparting some of its energy to an electron, and subsequently be completely absorbed via the photoelectric effect. As a practical matter, as long as all the interactions happen in the same detector the γ-ray energy will be counted in the full-energy peak. An algorithm for recovering the energy of γ rays that scatter out of one detector and deposit a fraction of their energy in a neighboring detector will be discussed in a later section.

3.3.1.3 Pair Production

For γ rays with an energy higher than twice the electron rest mass ($2m_e$ =1.022 MeV) there is a probability that the γ ray will interact with the electric field of the nuclei in the

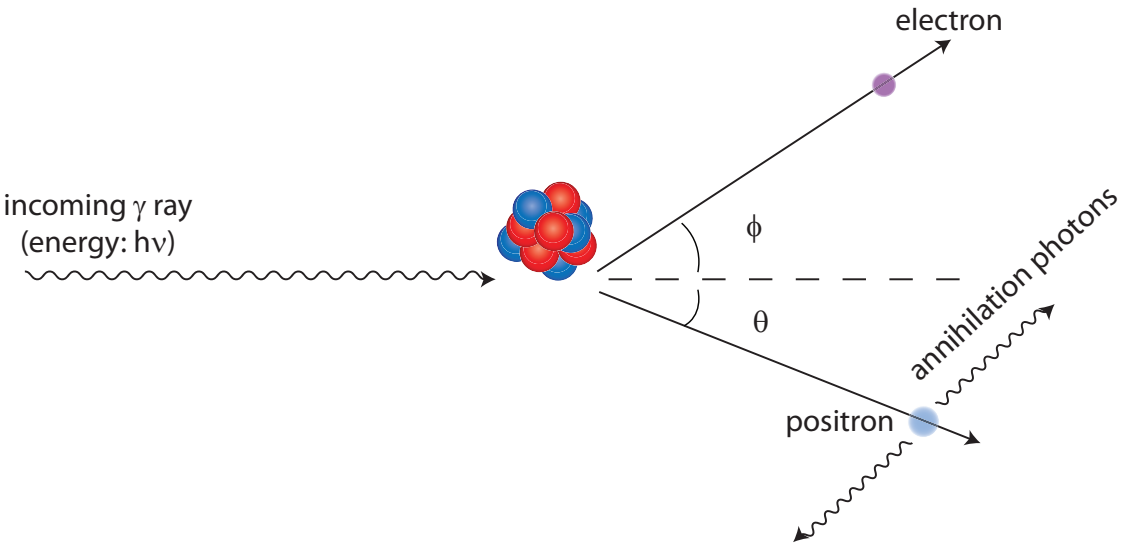

Figure 3.11: Schematic description of pair production in the electric field of a nucleus. The γ ray is incident from the left. Figure after [58].

absorber material by producing an electron-positron pair. Energy conservation gives:

$$E_\gamma = \left(T_{e-} + T_{e+}\right) - 2m_e c^2 \tag{3.15}$$

for the γ-ray energy, where T is the kinetic energy of the electron or positron. The probability of pair production is small for low-energy γ rays, but becomes the dominant interaction mechanism for γ rays with energies in excess of several MeV[3]. A positron is the anti-particle of an electron, so if an electron and positron collide, they will be annihilated and in the process emit two γ rays with an energy of $E_\gamma = 511$ keV traveling in opposite directions, as shown in Fig. 3.11. If the energies of the electron and positron are deposited in the detector, and the photons created in the annihilation of the positron escape the detector, the γ-ray spectrum measured in the detector will exhibit a *double escape peak* which has energy $E_{DE} = E_\gamma - 2m_e c^2$ (see Fig. 3.12). If only one of the annihilation photons escapes

[3]For Caesium Iodide, the material used to make the CAESAR detectors, pair production is the dominant interaction mechanism for γ rays with energies in excess of ~ 6 MeV. See Fig. 2.20 in [58].

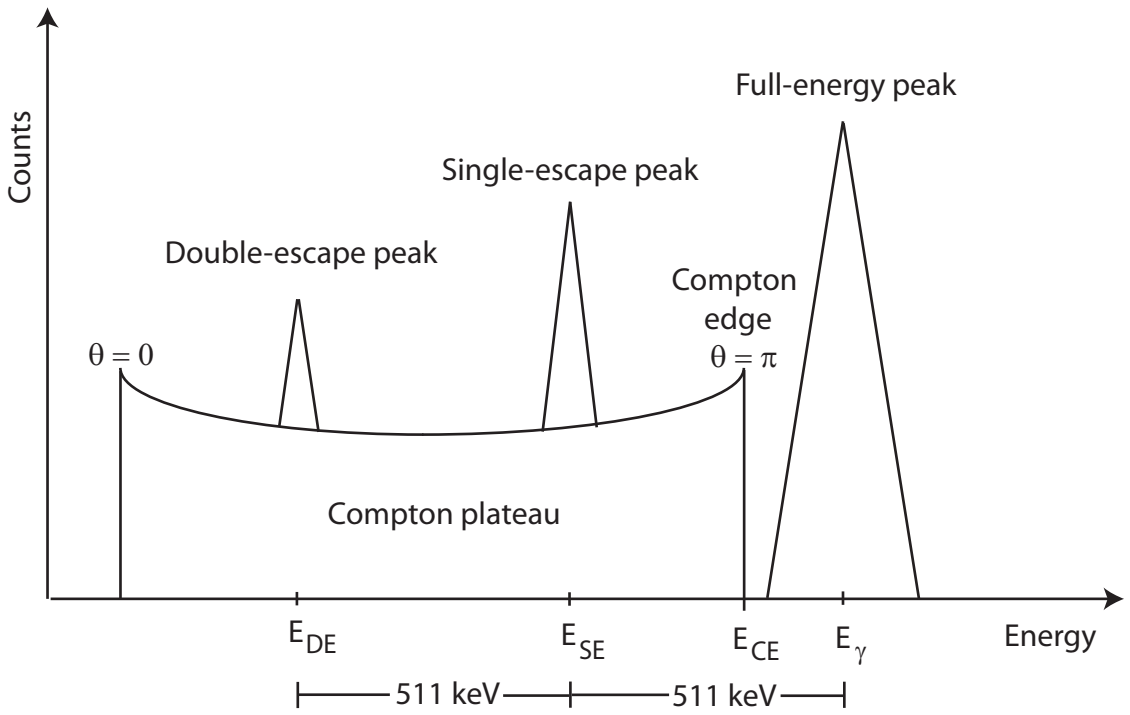

Figure 3.12: Cartoon of a γ-ray spectrum measured in a detector showing characteristic features from various interactions. The energies (E_x) are discussed in the text. Figure after [58].

the detector, the result is a *single escape peak*, whose signature is a peak at an energy given by $E_{SE} = E_\gamma - m_e c^2$.

Figure 3.12 shows a γ-ray spectrum with characteristic features of the various interactions discussed in these sections.

3.3.2 The Doppler Shift

When a γ ray with energy E_γ is emitted by a source moving at a relativistic velocity v with respect to the laboratory frame, the energy of the γ ray measured in the laboratory frame will be Doppler-shifted with respect to the original energy according to:

$$E_\gamma = E_\gamma^{lab} \cdot \gamma \left(1 - \beta \cos\theta\right) \tag{3.16}$$

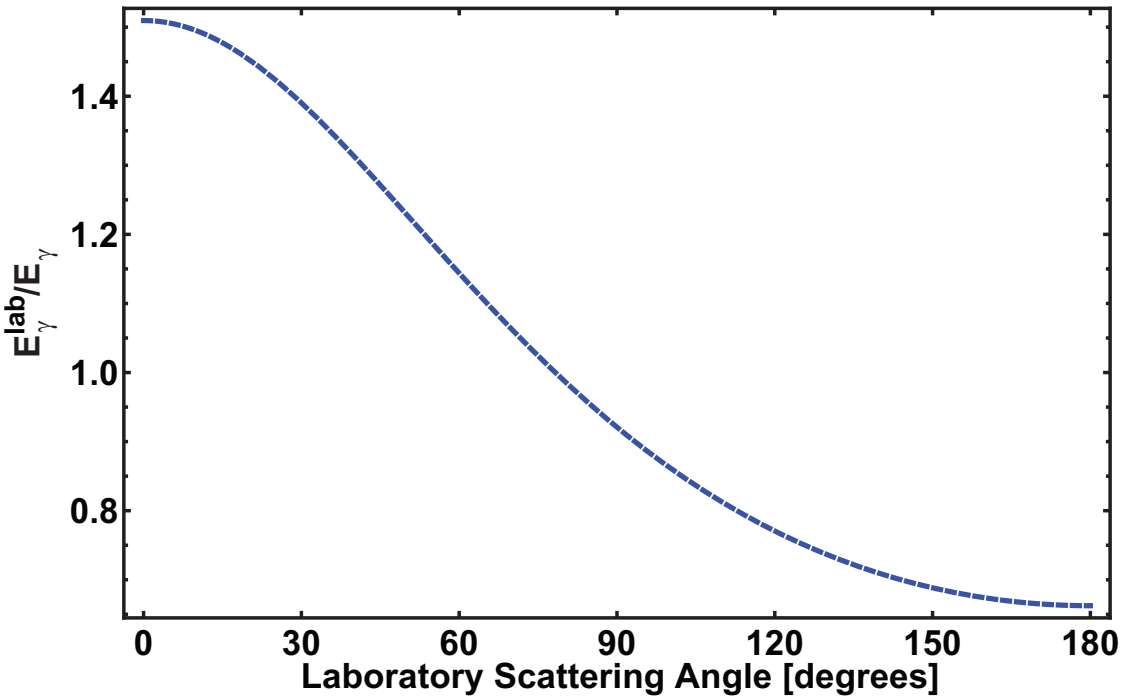

Figure 3.13: The ratio of the γ-ray energy measured in the lab frame (E_γ^{lab}) to the γ-ray energy measured in the rest frame of the projectile (E_γ) plotted as a function of the laboratory angle between the γ ray and the scattered projectile. Figure after Glasmacher [38].

where $\beta = v/c$ is the velocity of the source (v) with respect to the speed of light (c), and θ is the angle measured with respect to the direction of the projectile from which the γ ray is emitted.

The convention is to refer to the frame in which the projectile is at rest as the *rest frame* of the projectile, and to the frame of the stationary observer as the *laboratory frame*.

Figure 3.13 shows the relationship between E_γ and E_γ^{lab} for a γ ray detected at the angle θ (measured in the laboratory frame) between the emitted γ ray and the scattered projectile. As Eq. 3.16 suggests, an observer in the laboratory frame forward of the source will measure a higher energy for emitted γ rays than will an observer in the laboratory frame behind the source.

3.3.2.1 Energy Resolution and Doppler Broadening

In the intermediate-energy Coulomb excitation of even-even nuclei, one only expects to excite the first 2^+ excited state, as discussed in Sec. 2.1. Thus, after a Doppler correction is applied to the γ ray spectra, one expects to see a single peak corresponding to the prompt in-flight decay of an excited state in the projectile. The energy resolution of the γ-ray spectrometer used in such experiments must be sufficient to distinguish between γ rays emitted in-flight by the de-excitation of an excited state in the projectile, or γ rays created by atomic processes [65], and (in some cases) γ rays emitted in the laboratory frame by excited states in the target.

The energy resolution of a detector is often given in terms of the full width at half maximum (FWHM) of a peak in the spectrum [66]:

$$R = \Delta E/E, \tag{3.17}$$

where ΔE is the FHWM of the peak located at an energy E. For the detectors used in this work, the energy resolution goes as [66]:

$$R \propto \frac{1}{\sqrt{E\gamma}}, \tag{3.18}$$

for a γ ray with energy E_γ. However, following Eq. 3.16, γ rays emitted with an energy E_γ in the rest frame of the projectile will be detected in the laboratory frame with an energy E_γ^{lab}. Uncertainties in the velocity of the projectile emitting the γ ray ($\Delta\beta$) and the angle between the emitted γ ray and the scattered particle ($\Delta\theta$) contribute to the Doppler broadening, as

given by [38]:

$$\left(\frac{\Delta E_\gamma}{E_\gamma}\right)^2 = \left(\frac{\beta \sin\theta}{1-\beta\cos\theta}\right)^2 (\Delta\theta)^2 + \left(\frac{\cos\theta-\beta}{\left(1-\beta^2\right)(1-\beta\cos\theta)}\right)^2 (\Delta\beta)^2 + \left(\frac{\Delta E_{intr}}{E_\gamma}\right)^2. \tag{3.19}$$

It is instructive to examine the individual contributions to the total energy resolution, as is done in [38]:

1. $\Delta\beta$ is the uncertainty in the velocity of the projectile at the time of γ-ray emission. For excited states with short (less than ~ 1 ps) lifetimes, the γ-ray decay can happen anywhere in the target, therefore $\Delta\beta$ is given by the projectile's energy loss in the target expressed in units of β.

2. $\Delta\theta$ is the uncertainty in the angle between the γ ray and the scattered projectile. In the experiments discussed in this work, the uncertainty in θ is dominated by the finite opening angles of the detectors.

3. ΔE_{intr} is the intrinsic energy resolution of the γ-ray detectors, given in Eq. 3.18. The γ-ray detectors used for the measurements discussed in this work have intrinsic energy resolutions of better than 7% for a 1 MeV γ ray emitted at rest with respect to the detector [54]. The detector array discussed in this work was optimized so that the contribution to the energy resolution from $\Delta\beta$ and $\Delta\theta$ would match the contribution from the intrinsic energy resolution for 1 MeV γ rays emitted from projectiles moving at $0.3 - 0.4$ c.

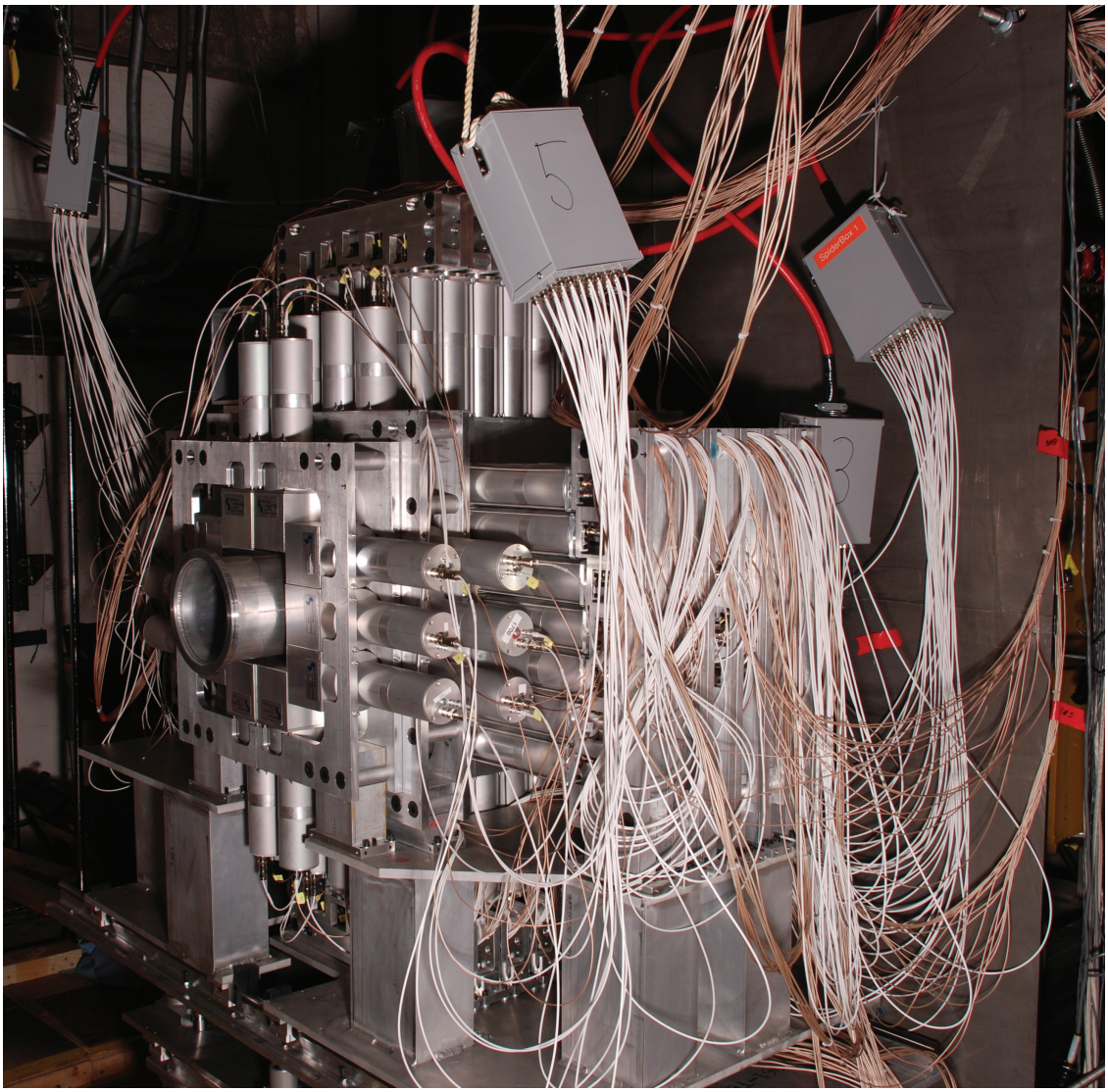

Figure 3.14: Photograph of CAESAR in front of the S800 spectrograph. The beam is incident from the left side of the image. See Fig. 3.15 for a side view of the CAESAR setup.

3.4 CAESAR - Gamma-Ray Detection

Efficiency is critical for γ-ray spectroscopy experiments of the most exotic nuclei, where the beam rates are on the order of a few particles per second. CAESAR (see Fig. 3.14) was commissioned in 2009 to answer this need. CAESAR is composed of 192 CsI(Na) crystals, weighing about 300 kg in total. It covers 95.5% of the solid angle around the target and is about 40% efficient for a 1 MeV γ ray [54].

The design and commissioning criteria for CAESAR are discussed in [54]. The design considerations were driven by the geometry of the experimental station where the detector would be primarily used (at the target position of the S800 spectrograph), the goal of 10% FWHM energy resolution from each detector for a 1 MeV γ ray emitted from a source moving at 40% of the speed of light, and the need for high detection efficiency. This baseline led to an array with 192 CsI(Na) crystals, 48 of which measure 3×3 inches on the front face and are three inches deep. The remaining 144 detectors measure 2×2 inches on their front face and are four inches deep. The dimensions of the crystal faces match the diameter of standard photomultiplier tubes.

As seen in Fig. 3.15, CAESAR is arranged in ten rings, labeled A (most upstream) through J (most downstream). The geometry of CAESAR is such that some detectors are partially shielded with respect to the target by others, especially at the corners. For this reason it is not expected that all detectors will measure the same number of γ rays isotropically emitted from a source placed in the center of the array.

The cross section for γ-ray interactions with the detector material increases with the atomic number (Z) of the material from which the detector is made (see Sec. 3.3.1). This being so, it is no surprise that materials optimized for γ-ray spectroscopy tend to be composed

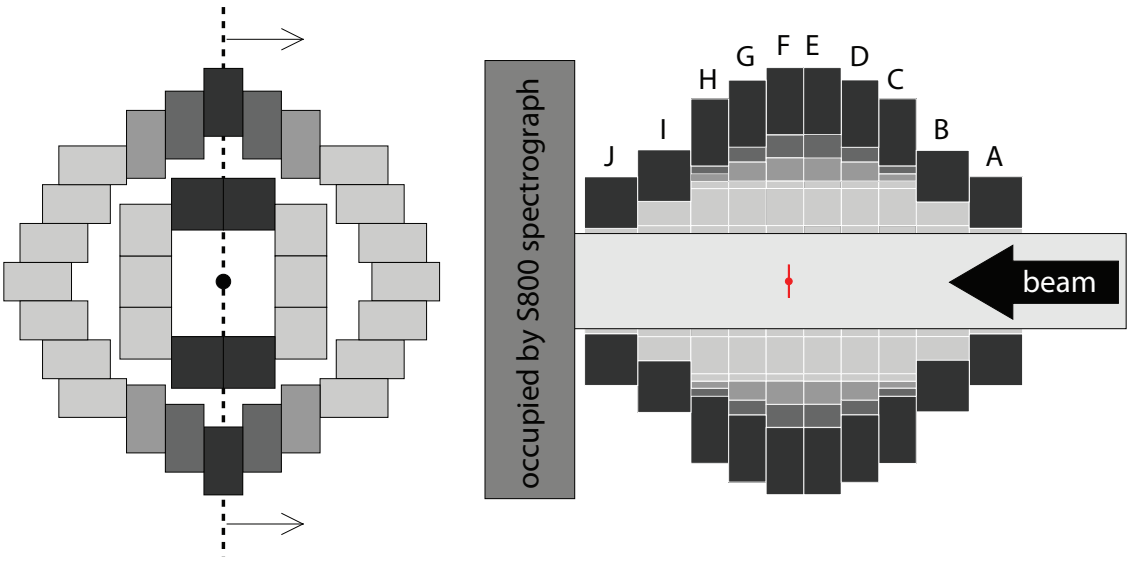

Figure 3.15: Schematic of the arrangement of the 2 × 2 × 4 inch and 3 × 3 × 3 inch crystals in CAESAR. The figure on the left shows a cross-sectional view of the rings F and J perpendicular to the beam axis. The figure on the right shows the ten rings of the array, labeled A (most upstream) through J (most downstream), as well as the target position (in red), and the position of the S800 Spectrograph. The gray scale of the crystals corresponds to the position on the rings, as shown in the figure on the left. Figure from [54].

of high-Z elements. There are two main types of detectors used for γ-ray spectroscopy: semiconductor detectors and scintillation detectors. A common choice of scintillation material is Thallium-doped Sodium Iodide (NaI(Tl)). The detectors used in this work were made of Sodium-doped Caesium Iodide (CsI(Na)), because this material has a higher stopping power for γ rays than does NaI(Tl) but provides nearly the same FWHM and response time (see [54]).

3.4.1 CAESAR Detectors

The CAESAR detectors were produced by ScintiTech, they consist of CsI(Na) scintillator crystals encased in an aluminum housing. The encapsulation is necessary because the CsI(Na) crystals are hygroscopic and as such will suffer damage if exposed to moisture. There is a 1.5 mm thick layer of reflective material between the 1 mm thick aluminum wall

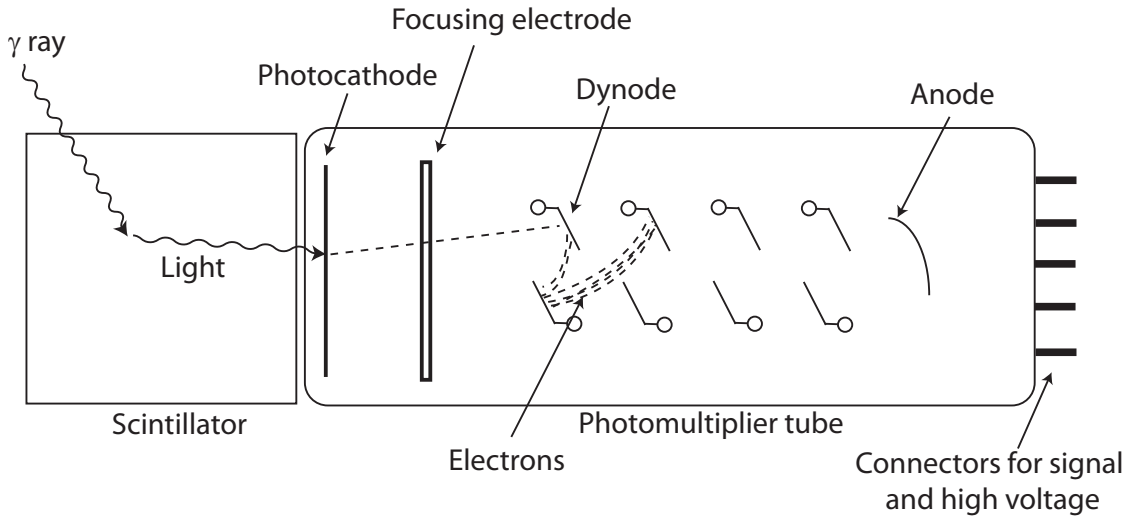

Figure 3.16: Schematic of a photomultiplier tube with attached scintillation crystal. Components are discussed in text. Figure after [66].

and the crystal. Each crystal is encapsulated on 5 sides, the 6^{th} side is covered with a round borosilicate window framed in aluminum so that it can be coupled to a photomultiplier tube.

A schematic of a photomultiplier tube (PMT) coupled to a scintillator is shown in Fig. 3.16. A PMT converts light into an electronic signal whose current is proportional to the energy of the γ-ray which caused the scintillation light. Photons produced as a result of a γ-ray interaction with the scintillating detector material hit the photocathode of the PMT and produce electrons via the photoelectric effect (Sec. 3.3.1.1), which are collected by the focusing cathode and multiplied by the system of dynodes. A bias voltage is applied across the PMT and each dynode is at a higher voltage than the previous one, such that the electrons produced on one dynode will be accelerated to the next. The dynodes are made of material that, when struck with an electron of sufficient energy, emits several more electrons (see [58]). The electrons are collected on the anode, and a current signal proportional to the number of photoelectrons emitted from the photocathode is read out. The compounds composing the glass of the tube are chosen to have an index of refraction which matches

the detector material and window, and the photocathode is deposited on the face of the PMT with is coupled to the scintillator by optical grease. The photoelectric tubes used in CAESAR were produced by Hamamatsu Photonics and are model numbers R1307 (with a three inch diameter) and R1306 (with a two inch diameter). The PMTs were covered by an aluminum shell which is screwed on to the crystal encapsulation.

CAESAR is typically operated near magnets and the fringe fields from these magnets can be non-negligible and affect the operation of the array's photomultiplier tubes. For this reason several layers of μ-metal were placed between the PMT and the aluminum shell. This shielding keeps the detector assemblies operational in magnetic fields of up to 2-3 mT. Magnetic fields exceeding 0.5 mT were observed to impact the pulse height of the signals. However, fringe fields from the S800 Spectrograph can exceed a magnetic field strength of 3 mT at and around the pivot point were CAESAR is located. Therefore, a large soft-iron steel shield (67 $\times$ 67 inches wide and 0.25 inches thick) was installed between the spectrograph and CAESAR as can be seen in Fig. 3.14.

3.4.2 Nearest-Neighbor Addback

In one of the mechanisms discussed in Sec. 3.3.1 for the interaction of γ rays with matter (the photoelectric effect) the γ ray is absorbed, while in the other two mechanisms (pair production and Compton scattering), the γ ray deposits part of its energy with each interaction. Compton scattering is a significant effect in the energy regimes used for this work. The signatures of this effect (see Fig. 3.12) are apparent in nearly all of the experimental γ ray spectra. If two neighboring detectors simultaneously register a γ-ray event, there are three possible reasons:

1. Two γ rays from the source triggered two neighboring detectors.

2. One (or both) of the γ-ray events was a random coincidence from background sources.

3. A γ ray deposited a fraction of its energy in one crystal and scattered into a neighboring crystal.

If the γ ray count rate low, it is unlikely that two unrelated γ rays will interact in neighboring crystals, thus ruling out option one. Option two can be ruled out as well, for much the same reason: the count rate from room background is low. Option three is by far the most likely of those listed above and will result in a loss of full-energy peak efficiency that can be recovered by a technique called *nearest-neighbor addback*. The nearest-neighbor addback routine is implemented in the CAESAR analysis code. The routine's algorithm is as follows:

1. Identify events in neighboring detectors.

2. If such an event is found, add the energies from both detectors together, taking the detector with the highest measured γ-ray energy as the first interaction point for Doppler reconstruction. The first interaction point determines the emission angle of the γ ray in the laboratory frame.

3. If necessary, perform a Doppler correction to this summed energy.

The nearest-neighbor addback routine increases the γ-ray detection efficiency significantly. The full-energy-peak efficiency of CAESAR for a 1 MeV γ ray emitted at rest is around 30%. The nearest-neighbor addback routine improves this efficiency by more than 20%. The improvement for a 2 MeV γ ray is more than 30% [54]. The threshold for γ-ray detection is vitally important to the efficiency of addback: if the threshold for detection is

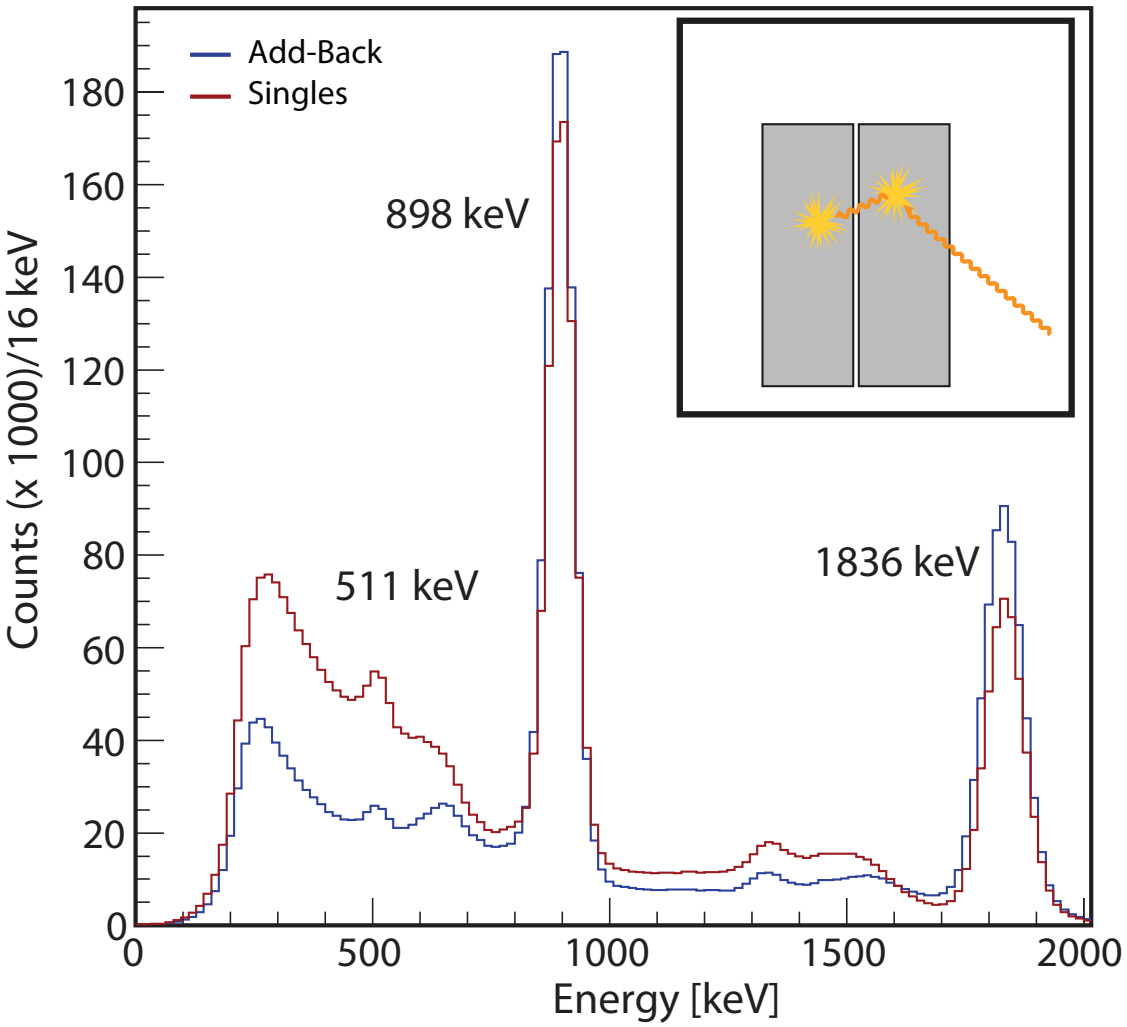

Figure 3.17: Inset: cartoon of a γ ray interacting in one detector and scattering into a neighboring detector. Main figure: comparison of addback (blue) and singles (no addback routine applied, red) spectra measured from the decay of a ^{88}Y source.

set at a higher γ-ray energy than that of the scattered γ ray, it will not be detected and the event will be lost.

An illustration of the effect of the addback routine is shown in Fig. 3.17. Since the nearest neighbor addback routine adds two lower energy events into one higher energy event, it has the effect of *decreasing* the number of counts in the Compton plateau (see Fig. 3.12) and increasing the number of counts in the full-energy peak, which improves the peak-to-background ratio.

3.4.3 CAESAR Detection Efficiency

In order to measure the cross section for a transition with a characteristic de-excitation γ-ray energy (Eq. 2.18) it is necessary to measure the number of γ rays emitted in the reaction. The number of γ rays detected (N_γ^{obs}) is related to the number of γ rays emitted (N_γ) by the detection efficiency (ϵ) of the detection system:

$$N_\gamma = \frac{N_\gamma^{obs}}{\epsilon\left(E_\gamma\right)} \tag{3.20}$$

The absolute efficiency for γ-ray detection is given by:

$$\epsilon\left(E_\gamma\right) = \frac{\text{number of } \gamma \text{ rays detected}}{\text{number of } \gamma \text{ rays emitted}} \tag{3.21}$$

This efficiency depends on the energy of the emitted γ ray in the laboratory frame. If the source is moving, the detected γ-ray energy will correspond to the Doppler-shifted energy (see Sec. 3.3.2). Due to the Lorentz boost, the solid angle coverage of a detector is different in the rest frame of the projectile from the laboratory frame. In addition, the angle of emission

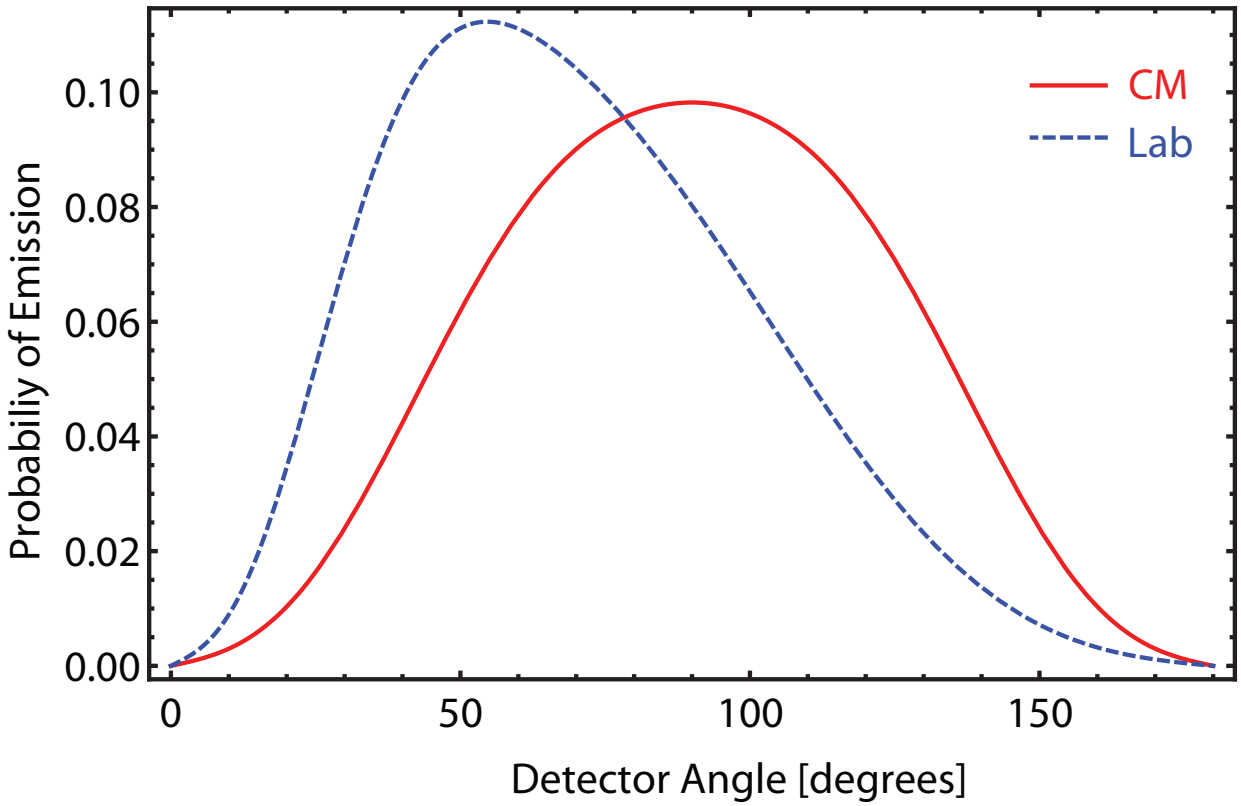

Figure 3.18: Change in angular distribution for γ rays emitted isotopically in the projectile frame (red solid line) from a source moving at $v/c = 0.3912$ and detected in the laboratory frame (blue dashed line). This angular distribution plot is for γ rays emitted in the de-excitation of ^{40}Si.

for a γ ray in the projectile frame is related to the angle of detection (in the laboratory frame) by [41]:

$$\tan\left(\theta_{lab}\right) = \frac{\sin(\theta_{cm})}{\gamma\left(\cos(\theta_{cm}) + \beta\right)} \tag{3.22}$$

where $\theta_{lab(cm)}$ are the angles of emission in the lab (projectile) frame. If the angular distribution of γ rays in the projectile frame is isotropic, this leads to a forward-focusing in the lab frame of γ rays emitted in the projectile frame (see Fig. 3.18). Thus the energy-dependent efficiency should be different for γ rays emitted at the same energy in-flight and at rest. One typically calculates the total efficiency by folding the detection efficiency with

the angular distribution of emitted γ-rays ($W(\Omega)$), this is discussed by Olliver *et al* in [75]):

$$\epsilon_{tot}\left(E\gamma,\Omega\right) = \frac{\int_{\Omega} d\Omega\epsilon\left(E_{\gamma},\Omega\right) W(\Omega)}{\int_{\Omega} d\Omega W(\Omega)} \tag{3.23}$$

This approach works well for a spherically symmetric detector system. CAESAR is not spherically symmetric, so in order to calculate in-beam efficiencies, a GEANT4 [68] simulation was written by Baugher *et al.* [70], which takes into account the geometry of CAESAR, the target position, the aluminum housing of the crystals, the small gap between adjacent detectors, the aluminum beam pipe, the velocity of the source at emission, the thickness and composition of the target, the lifetime of the state emitting the γ ray, and other experimental conditions. This simulation accurately reproduces measured spectra of standard γ ray sources at rest.

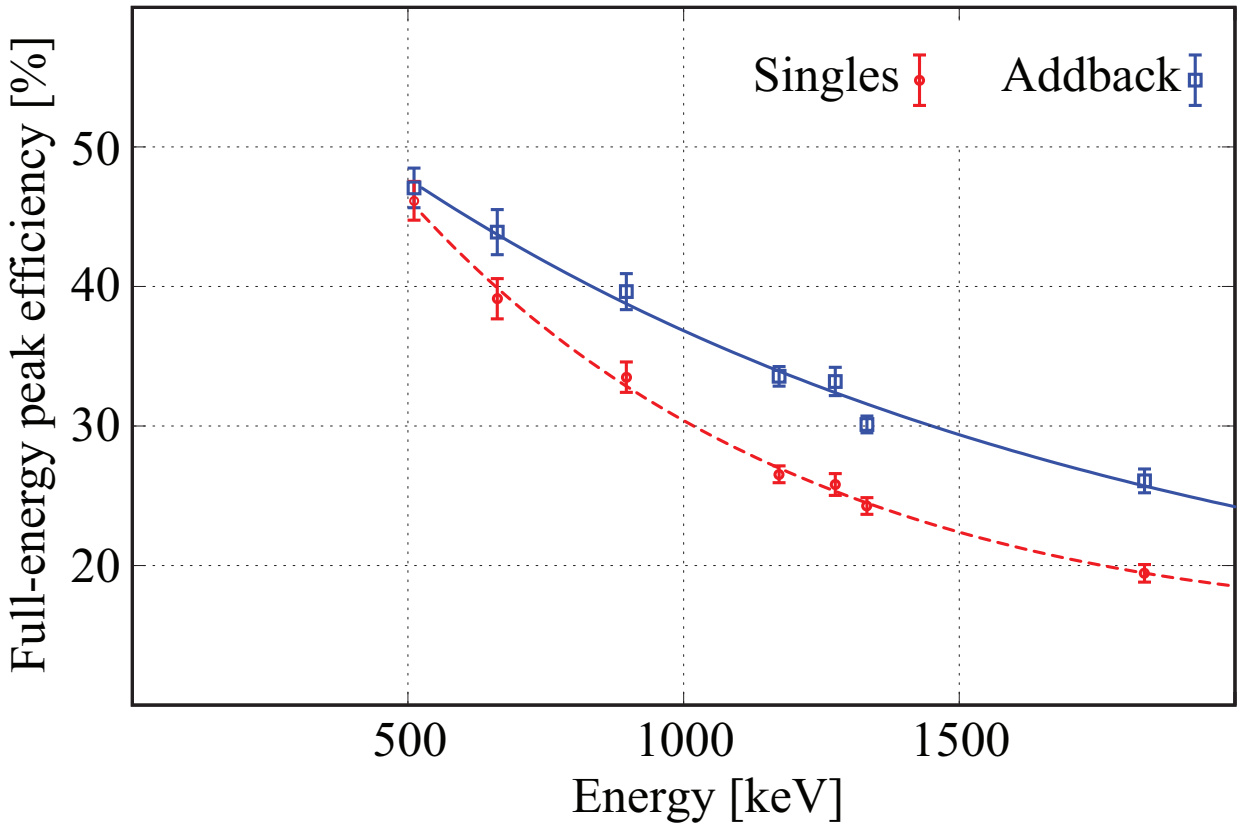

Figure 3.19: Measured absolute full-energy peak efficiency for CAESAR. Sources used are standard γ-ray calibration sources: ^{22}Na, ^{137}Cs and ^{88}Y. The dashed red line is the measured efficiency, the solid blue line is the efficiency including addback. Figure from [54].

Chapter 4

Coulomb Excitation of $^{34-42}$Si

The intermediate-energy Coulomb excitation of $^{34-42}$Si was performed in order to determine the strength of the electric quadrupole transition matrix element, the $B\left(E2; 0^+ \rightarrow 2_1^+\right)$ value, for this isotopic chain. Each silicon isotope was produced as a secondary beam from the fragmentation of a ^{48}Ca primary beam on a thick ^{9}Be target. The primary beam was accelerated to 140 MeV/u in the Coupled Cyclotron Facility at NSCL [50]. After the fragmentation of the primary beam, the silicon isotope of interest was selected by the A1900 fragment separator [51, 52] and directed onto a high-Z target located at the target position of the S800 magnetic spectrograph [53]. Particles in the secondary beam which were excited by the Coulomb field of the high-Z secondary target emitted de-excitation γ rays with energies characteristic of the excited state. These γ rays were detected by the high-efficiency scintillator array CAESAR [54] in coincidence with scattered particles tracked on an event-by-event basis in the S800 magnetic spectrograph [53].

4.0.4 Experimental Details

Assuming that only the first state with spin-parity 2^+ is excited, the experimental cross section for intermediate-energy Coulomb excitation of an even-even nucleus is calculated as:

$$\sigma_{2^+\rightarrow 0^+} = \frac{N_{\gamma(2^+\rightarrow 0^+)}}{N_B N_T} \ , \tag{4.1}$$

where $N_{\gamma(2^+\rightarrow 0^+)}$ is the number of γ rays emitted in the decay of the first 2^+ excited state, N_B is the number of nuclei of interest incident on the target and N_T is the areal number density of the target, given by:

$$N_T = \frac{N_A \cdot \rho}{A} \ . \tag{4.2}$$

Here, $N_A = 6.022 \times 10^{23}$ mol^{-1} is Avogadro's number, ρ is the areal density of the secondary reaction target in g/cm^2, and A is the atomic mass of the target nuclei in g/mol. Two different targets were used in this work. The experiments measuring the cross sections for the intermediate-energy Coulomb excitation of $^{34-40}$Si used a 0.518 g/cm^2 (about 268 μm) thick ^{197}Au target and the experiment measuring the cross section for the intermediate-energy Coulomb excitation of ^{42}Si used a 0.492 g/cm^2 (about 502 μm) thick ^{209}Bi target. The uncertainty in the thickness of the target was assumed to be 4 mg/cm^2. The areal number densities calculated following Eq. 4.2 for the two targets used in this work are given in Tab. 4.1.

The determination of the number of beam particles and of the number of de-excitation γ rays emitted will be discussed in the following sections.

isotope	target	ρ (g/cm^2)	thickness (μm)	N_T
$^{34-40}$Si	^{197}Au	0.518(4)	268(2)	1.58(1) $\times 10^{21}$
^{42}Si	^{209}Bi	0.492(4)	502(4)	1.42(1) $\times 10^{21}$

Table 4.1: Areal densities, thicknesses, and areal number densities of the secondary targets used in this work.

4.0.4.1 Particle Detection and Tracking

Particles were detected on an event-by-event basis in the focal plane of the S800 spectrograph (see Fig. 3.3). The focal plane detectors used in this work were CRDCs, which provide tracking information for the particles (see Sec. 3.2.1.1), the ionization chamber, which measures the energy loss of particles passing through it (see Sec. 3.2.1.3) and the e1 scintillator, which provides the time-of-flight signal for the particles.

4.0.4.2 S800 Mask Calibrations and Ionization Chamber Gain Matching

As discussed in Sec. 3.2.1.1, the CRDCs in the S800 focal plane measure the (x,y) positions of projectiles. The CRDCs are one meter apart, so if both CRDCs have measured the (x,y) position of a particle the scattering angle for this particle can be determined. The x position of an event is known from a fit of the charge distribution induced on the segmented cathode pads. The y position is calculated from the drift time of the electrons created in the ionization of atoms in the gas mixture filling the CRDCs. The drift time is the measured difference in time between the collection of the electrons on the anode wire in the CRDC and time at which the e1 scintillator registered the event.

The drift time depends on the properties and composition of the fill gas and is observed to shift over time (see Sec. 3.2.1.1). The drift time was calibrated periodically during the experiments discussed in this work by inserting a mask with holes at certain positions in front

isotope	C1 slope	C2 slope	PD1 (%)	PD2 (%)	elapsed time (hr)
^{34}Si	-0.0514	0.0506	1.8	2	17
^{36}Si	-0.0522	0.0544	3.5	3	9
^{38}Si	-0.0537	0.0530	2.6	2.5	10
^{40}Si	-0.0492	0.0485	1.7	2	38
^{42}Si	-0.0691	0.0645	4.2	5.4	134

Table 4.2: initial CRDC1 (C1) and CRDC2 (C2) drift time calibration values and the percent difference in calibration value for CRDC1 (PD1) and CRDC2 (PD2) over the course of the measurements as well as the number of hours secondary beam was incident on the CRDCs.

of each of the two CRDCs. The drift time calibration was obtained based on the position of the holes in the mask and the measured positions in the CRDCs. The drift time calibration was calculated by applying a linear function to map the measured y positions to the known y positions of the holes in the mask. A spectrum taken during a mask calibration is shown in Fig. 3.6. The drift time calibration obtained from the mask calibration was adjusted on a run-by-run basis (as discussed in Sec. 3.2.1.1). Figure 3.7 shows the effect of this correction.

The ionization chamber is divided into 16 segments and the energy loss measured in each segment is recorded. The segments of the ionization chamber were gain-matched by a linear function which arbitrarily aligned the energy loss measured in each segment with that of the first segment. The total energy lost in the ionization chamber is the sum of the energy lost in each of the segments.

4.0.4.3 Particle Identification

Particles were identified by measuring the time-of-flight difference event-by-event between two thin plastic scintillators (see Sec. 3.2.1.4), one before (the object scintillator) and one after the secondary target (the e1 scintillator, see Fig. 3.3). The time-of-flight measured

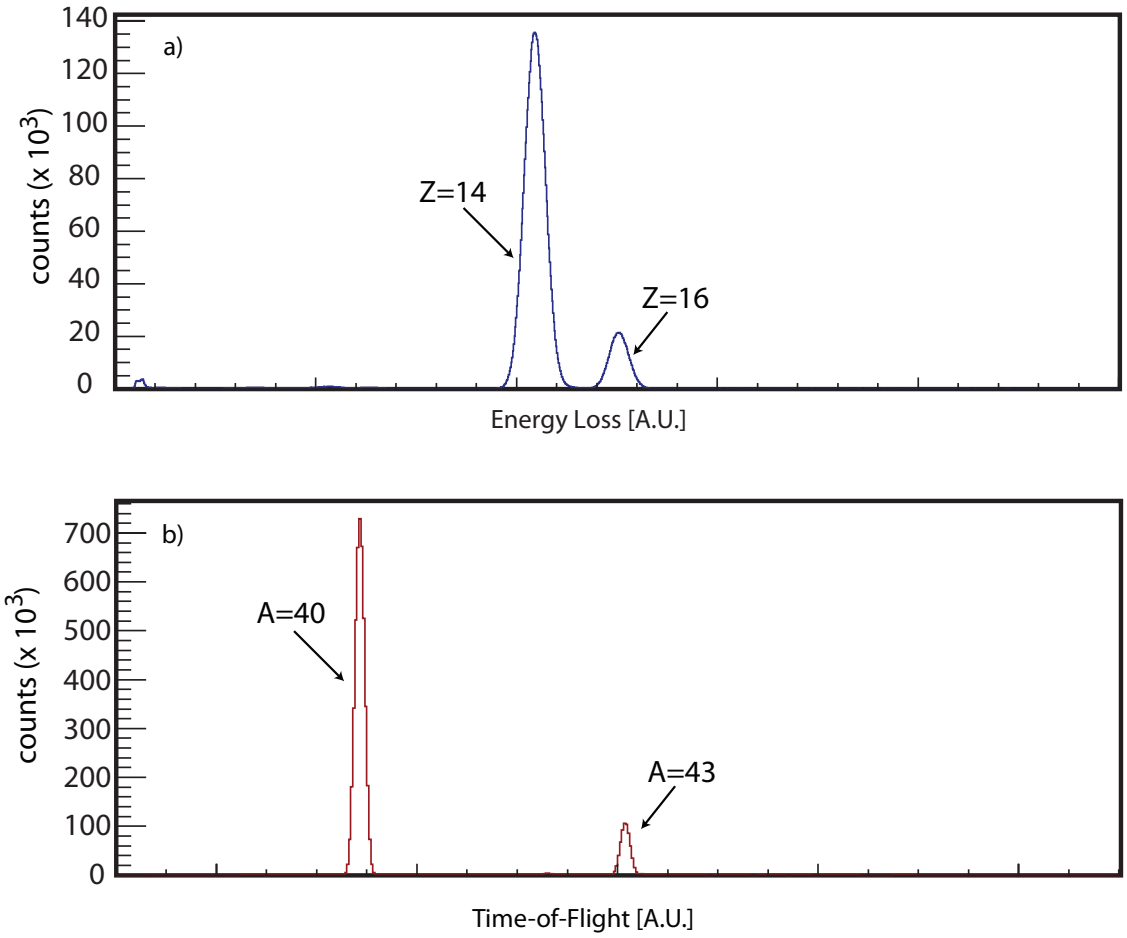

Figure 4.1: panel (a): energy loss measured in the S800 ionization chamber for the intermediate-energy Coulomb excitation of ^{40}Si. panel (b): time-of-flight difference measured between the scintillator in the object position of the S800 analysis line (before the secondary target) and the e1 scintillator in the S800 focal plane (after the secondary target) for the intermediate-energy Coulomb excitation of ^{40}Si.

isotope	PT	WT	BTE (MeV/u)	rate (pps)	purity (%)
^{34}Si	752	750	87	1.144×10^{6}	94
^{36}Si	752	750	86	9.92×10^{4}	92
^{38}Si	752	750	91	8400	91
^{40}Si	752	750	90	$\simeq$ 184	85
^{42}Si	1269	450	84	$\simeq$ 140	1.4

Table 4.3: The ^{9}Be primary target thickness (PT), ^{27}Al wedge thickness (WT), both in mg/cm^{2}, beam energies before the secondary target (BTE), rate of the isotope of interest at the A1900 focal plane, and purities of the secondary beams used in the measurements discussed in this work.

in this way for the ^{40}Si secondary beam is shown in panel b of Fig. 4.1. This allowed the separation of the reaction products by A/Z (assuming $Q = Z$). The energy loss was measured (also on an event-by-event basis) in the ionization chamber in the focal plane of the S800 (shown for ^{40}Si in panel a of Fig. 3.2.1.3), which allowed discrimination by atomic number.

The correlation between energy loss and time-of-flight measured for the beam containing ^{40}Si is shown in Fig. 4.2. The isotope of interest (^{40}Si) can be clearly distinguished from the other particles in the beam. The purity of the incoming beam was about 85% ^{40}Si, the major contaminant (^{43}S) made up about 12% of the beam. Tab. 4.3 shows the rates and purities at the A1900 focal plane for all of the secondary beams discussed in this work. If the rate at the S800 target position was greater than the rate limitation imposed by the CRDCs in the S800 focal plane (about 6000 particles per second (pps), see Sec. 3.2.1.1), the rate was lowered to $\approx$ 6000 pps by attenuating the primary beam.

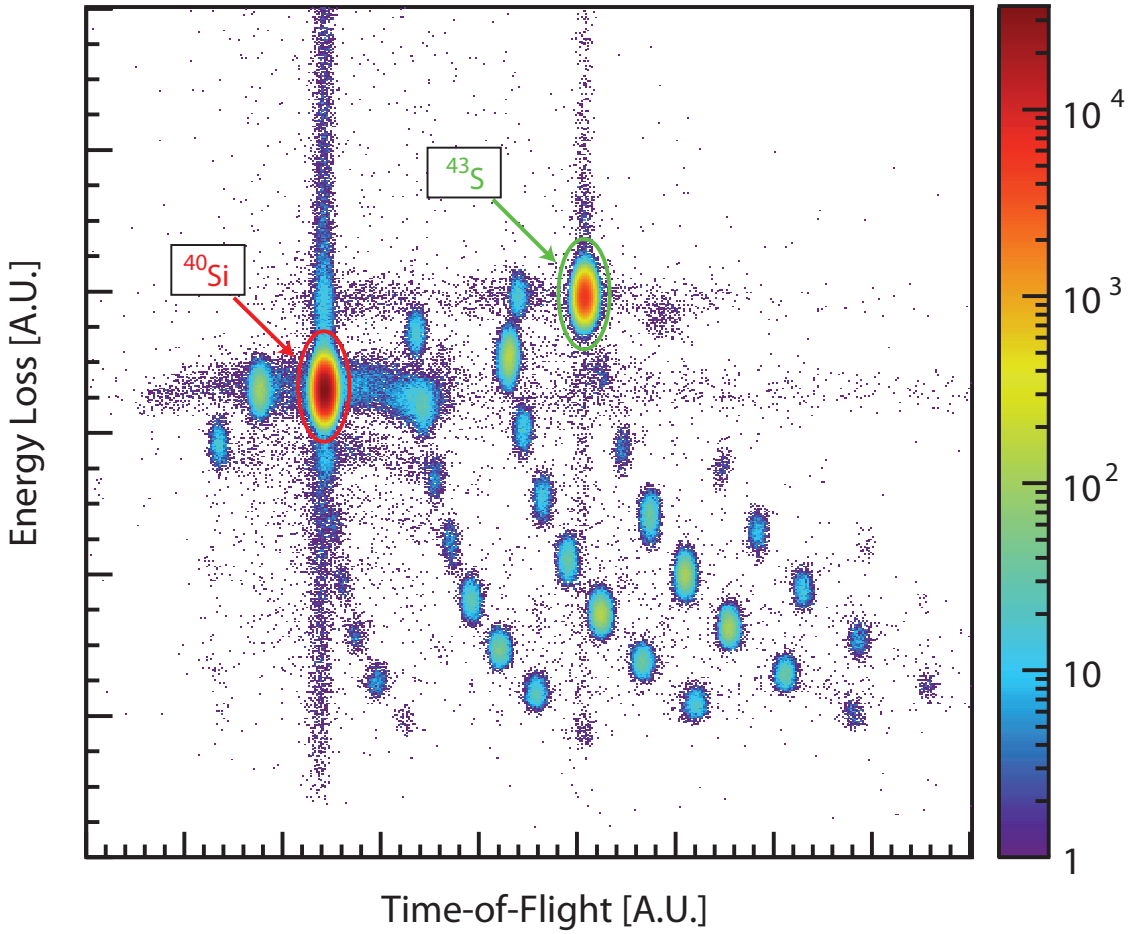

Figure 4.2: Energy loss measured in the ionization chamber in the S800 focal plane plotted against the time-of-flight difference between a scintillators before and after the secondary target. The isotope of interest (^{40}Si) is labeled. The color scale corresponds to the intensity at which the isotope was produced.

4.0.4.4 Scattering Angle Reconstruction

In order to ensure that the excitation of the projectile (or target) is a result of the electromagnetic field of the target (or projectile), the analysis is restricted to events with a smaller scattering angle than a maximum scattering angle corresponding to the safe impact parameter of touching spheres plus 2 fm (see Sec. 2.2.3). The scattering angle is reconstructed from the (x,y) positions measured in the CRDCs and with the known optics properties of the spectrograph according the method described in Sec. 3.2.1.1.

The scattering angle (θ) is calculated as:

$$\sin(\theta) = \sqrt{\sin^2(a_{ta}) + \sin^2(b_{ta})} \tag{4.3}$$

where a_{ta} is the angle in the dispersive direction reconstructed after the target and b_{ta} is the angle in the non-dispersive direction reconstructed after the target. The correlation between these two angles is shown in Fig. 4.3 for the intermediate-energy Coulomb excitation of ^{40}Si.

The scattering angle calculated from the dispersive and non-dispersive angles for the intermediate-energy Coulomb excitation of ^{40}Si is shown in Fig. 4.4. The maximum safe scattering angle was calculated from Eq. 2.20 and using the mid-target beam energy, which was calculated using LISE++ [56]. The energy of the secondary beam before the target deduced from the rigidity of the S800 analysis line before the target. Table 4.4 summarizes the calculated values of the laboratory and center-of-mass frame maximum scattering angles and of the beam energy calculated at mid-target for all of the isotopes studied in this work.

The nominal angular acceptance in the laboratory frame of the S800 spectrograph is 7° in the dispersive direction and 10° in the non-dispersive direction [55]. The safe angles used in this work are well below the acceptance limit of the S800 spectrograph. The accuracy of

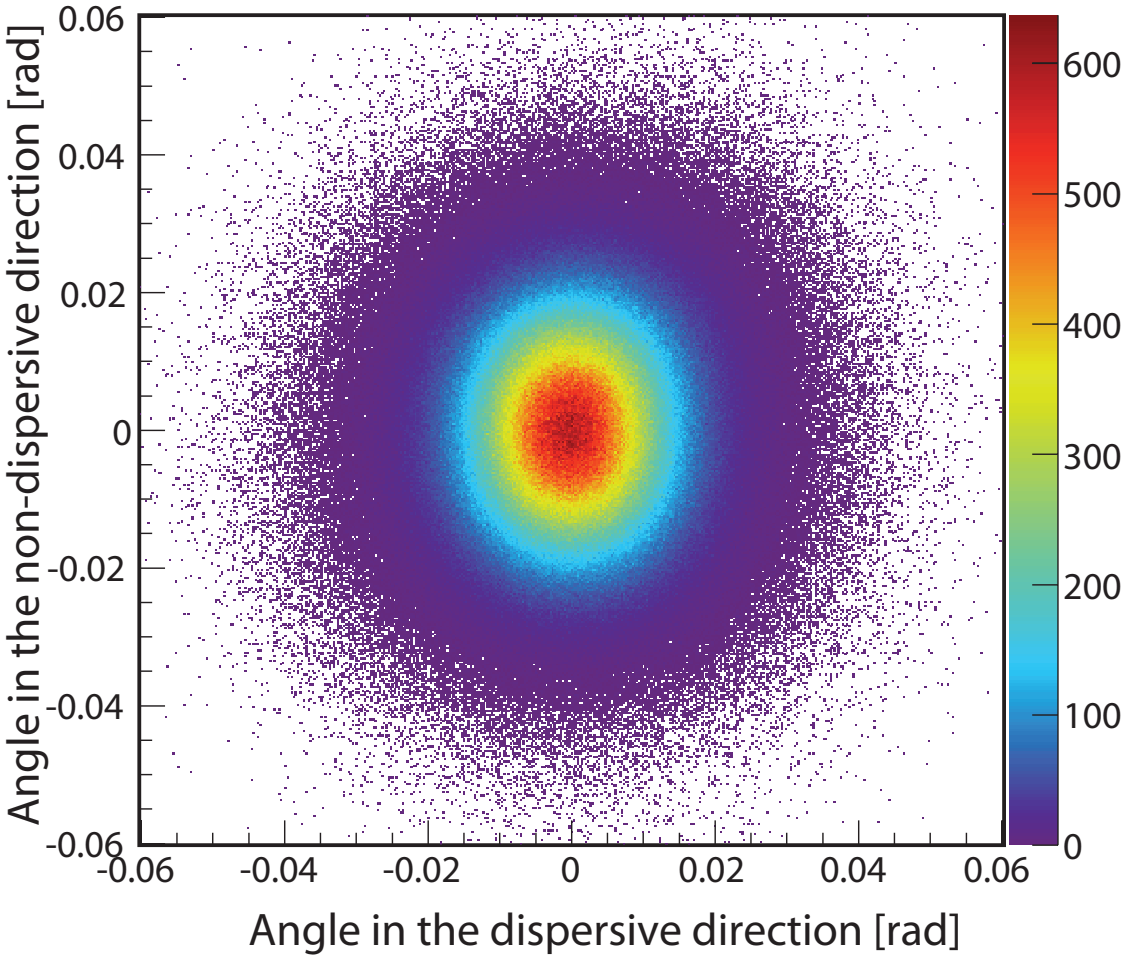

Figure 4.3: Matrix showing the correlation between the dispersive and non-dispersive angles as reconstructed at the target position. The matrix is gated on ^{40}Si.

isotope	E_{MT} (MeV/u)	θ_{lab}^{max} (mrad)	θ_{cm}^{max} (degrees)
^{34}Si	81	46	3.1
^{36}Si	81	43	3.0
^{38}Si	86	39	2.7
^{40}Si	85	37	2.6
^{42}Si	79	39	2.7

Table 4.4: Energies and scattering angles calculated at mid-target thickness for the intermediate-energy Coulomb excitation of $^{34-42}$Si.

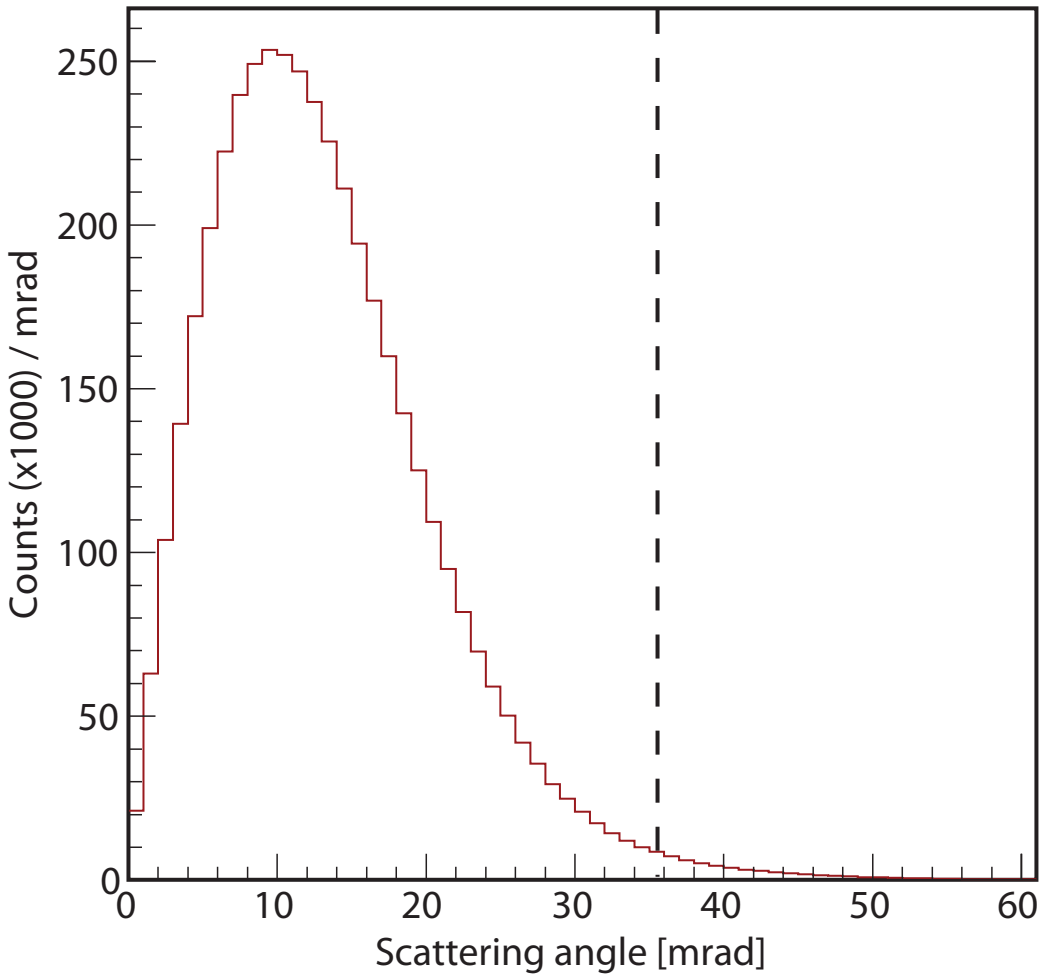

Figure 4.4: A spectrum showing the number of scattered ^{40}Si nuclei as a function of the scattering angle. The maximum scattering angle corresponding to safe impact parameter is marked by the black dashed line.

isotope	Obj$_{eff}$ (%)	CRDC 1$_{eff}$ (%)	CRDC 2$_{eff}$ (%)
^{34}Si	98(1)	98(1)	99(1)
^{36}Si	100(1)	99(1)	99(1)
^{38}Si	100(1)	99(1)	97(1)
^{40}Si	99(1)	99(1)	98(1)
^{42}Si	100(1)	100(1)	100(1)

Table 4.5: Efficiencies of the particle detection systems in the focal plane for the measurements discussed in this work.

the reconstructed scattering angle event-by-event in the laboratory frame is assumed to be 2 mrad (0.12°) [55].

4.0.4.5 Efficiency of the Focal Plane Detectors

The particle detectors used in this measurement are: CRDC 1, CRDC 2, the ionization chamber, the object scintillator, and the e1 scintillator. The efficiency of each of these detectors is calculated with respect to the ionization chamber, which is assumed to be 100% efficient. The measured efficiencies of these detectors are given in Tab. 4.5. The uncertainty quoted is statistical.

4.0.5 CAESAR Calibrations and Simulation Input

The signature of intermediate-energy Coulomb excitation is a de-excitation γ ray, emitted either from an excited state of a projectile (in flight) or from an excited state in the target (at rest). The γ rays emitted following the intermediate-Coulomb excitation of $^{34-42}$Si were detected in the CAESium Iodide ARray (CAESAR) [54], which was positioned around the target position of the S800 Spectrograph. The properties of CAESAR are discussed in Sec. 3.4.

The detectors were gain matched using the 1836 keV γ ray from an ^{88}Y source. The voltage was set at the beginning of each experiment to be such that the 1836 keV line was at channel 500 in a raw energy spectrum. In order to perform the energy calibration for each detector, γ-ray spectra were obtained from standard γ-ray calibration sources (^{88}Y, ^{137}Cs and ^{22}Na), covering a range of energies from about 500 keV to 2 MeV. The centroids of the full-energy-peaks for each transition were obtained, and these positions fit to the known value of the transition by a second order polynomial. The resulting energy calibration was used to sort the data. In order to ensure that the effects of signal drift were minimized, an energy calibration taken before the beginning of each Coulomb excitation setting was used (i.e. source data was taken between each experimental setting of ^{34,36,38,40}Si, and the analysis of each setting was performed with an energy calibration made from the source data taken before that setting). This was necessary because the change in the rigidity of the S800 spectrograph causes the magnetic field in the vicinity of CAEASR to change, which can cause shifts in the effective gain of the PMTs. As Fig. 4.6 shows, the calibrated energies remained stable throughout the experiment.

In the first experiment (the Coulomb excitation of $^{34-40}$Si, the trigger was S800 singles (downscaled by 50), or S800-CAESAR coincidences (not downscaled), or CAESAR singles (downscaled by 60). The downscaled CAESAR singles trigger allows the measurement of the 1460 keV γ ray in the room background from the decay of ^{40}K as well as the background from a $\simeq$ 2.6 MeV γ ray from the decay of ^{208}Tl.

The effect of this energy calibration is seen in Fig. 4.5. Both spectra show the result of measuring the decay of an ^{88}Y source for $\approx$ 5 minutes, the spectrum on the left is shown without calibration, while the spectrum on the right has a second-order polynomial calibration applied. The results shown in these spectra are typical for the calibrations used

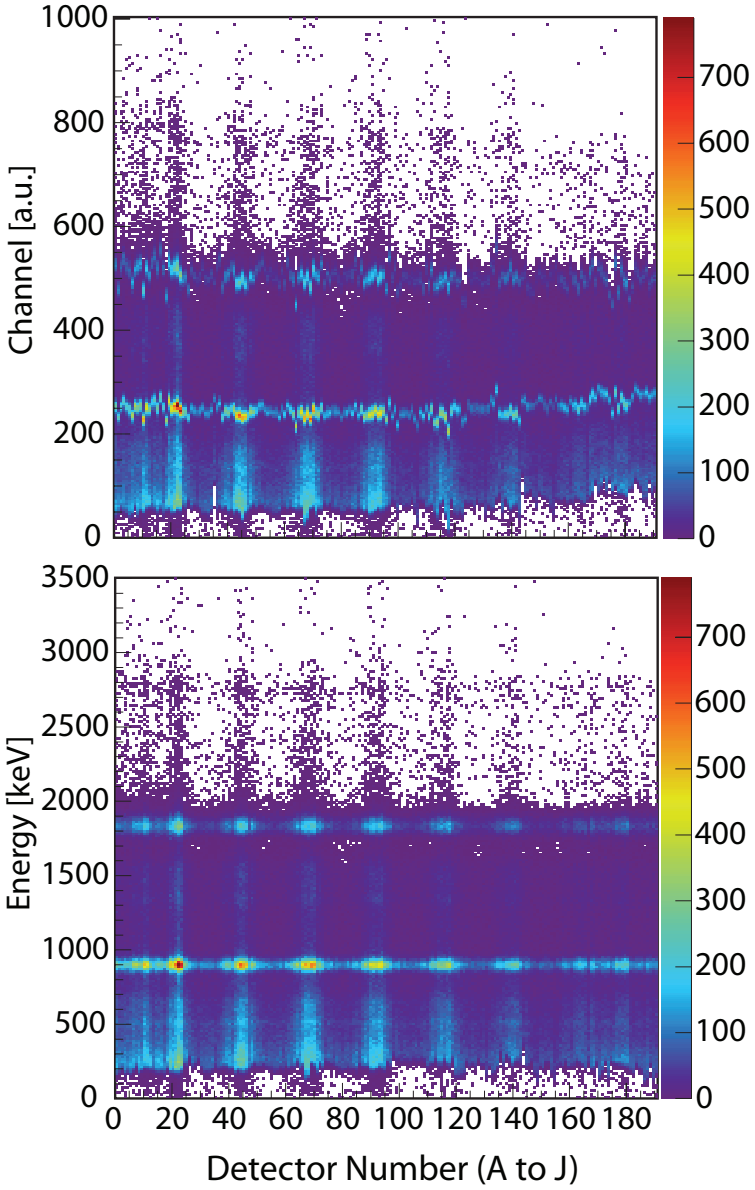

Figure 4.5: Top: un-calibrated energies plotted as a function of detector number (detector A1 is 1, detector J10 is 192 - see Fig. 3.15 for ring ordering). The detectors were gain-matched by adjusting the voltage so that the 1836 keV transition in ^{88}Y corresponded to channel 500. Bottom: a second-order polynomial fit using data points taken from 5 minutes of measuring the decay of ^{88}Y and ^{22}Na. This calibration was used for the analysis of γ-rays detected in coincidence with ^{34}Si particles in the S800. Some detectors are shielded from the room background by others (see Sec. 3.4) and because of this have a lower number of room background counts. Both spectra are shown for the same ^{88}Y data set.

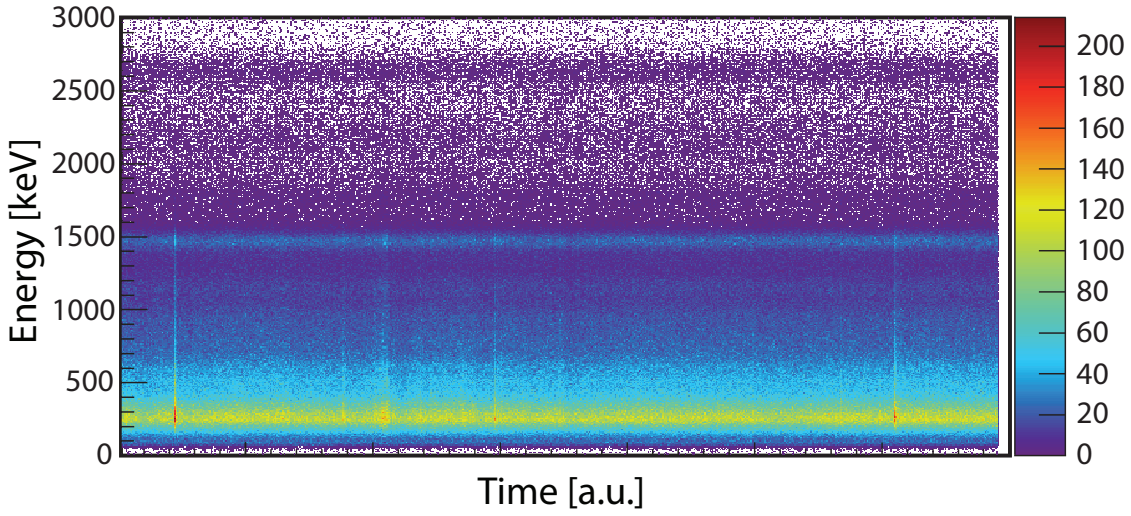

Figure 4.6: Elapsed time (x) vs. the energy of a representative detector (y) during the Coulomb excitation of ^{34}Si. The trigger is CAESAR singles downscaled by a factor 60, so room background is shown. The intensity variations represent changes in the beam rate that allow more background to be acquired. About 18 hours of data is shown in this plot, so it is clear that the gain is stable over long time scales.

in the analysis of all the measurements discussed in this work.

4.0.5.1 Energy Resolution of CAESAR

In order to accurately simulate the response of CAESAR to γ rays it is necessary to parameterize the energy resolution of the detectors in CAESAR (discussed in Sec. 3.3.2.1) in a way that can be reproduced in the GEANT4 simulation (which will be discussed subsequently). The widths of several peaks in each ring of CAESAR were fit to provide input for the energy resolution simulated for CAESAR by the GEANT4 simulation. The γ-ray energies used were: 511 keV (from the decay of ^{22}Na), 898 and 1836 keV (from the decay of ^{88}Y) and 1460 keV (from the decay of ^{40}K). The widths of the peaks were measured by fitting a Gaussian distribution and extracting the width of the distribution. The extracted

Ring	α	β
A	0.72	0.53
B	0.39	0.62
C	0.63	0.54
D	0.92	0.47
E	0.44	0.59
F	0.61	0.54
G	0.68	0.55
H	0.38	0.64
I	0.60	0.57
J	0.62	0.56

Table 4.6: Parameters for Eq. 4.4 describing the energy resolution in each ring of CAESAR.

widths were fit as a function of their energy. The fit function used was:

$$\sigma(E) = \alpha \cdot E^{\beta} \ , \tag{4.4}$$

where σ is related to the FWHM of the peak by $FWHM = 2\sqrt{2\ln(2)}\sigma$, and α, β are fit parameters. The values obtained from the fits of the widths of the peaks in CAESAR and subsequently used as inputs to the GEANT4 simulation are given in Tab. 4.6. A plot of σ as a function of γ-ray energy is shown for ring A of CAESAR in Fig. 4.7.

4.0.5.2 Nearest Neighbor Addback and Threshold Effects

The nearest neighbor addback routine is discussed in [54] and in Sec. 3.4.2. The addback routine attributes γ-ray energies measured in coincidence in neighboring detectors to a Compton-scattered γ ray (see Sec. 3.3.1 for a discussion of Compton scattering). The two measured γ-ray energies are added together, with the detector with the highest energy deposition taken as the first interaction point. If the energy threshold for γ-ray detection is higher than the energy of the scattered γ ray it will not be detected, so it is necessary to include the energy thresholds in the GEANT4 simulation in order to reproduce the effect of the threshold on

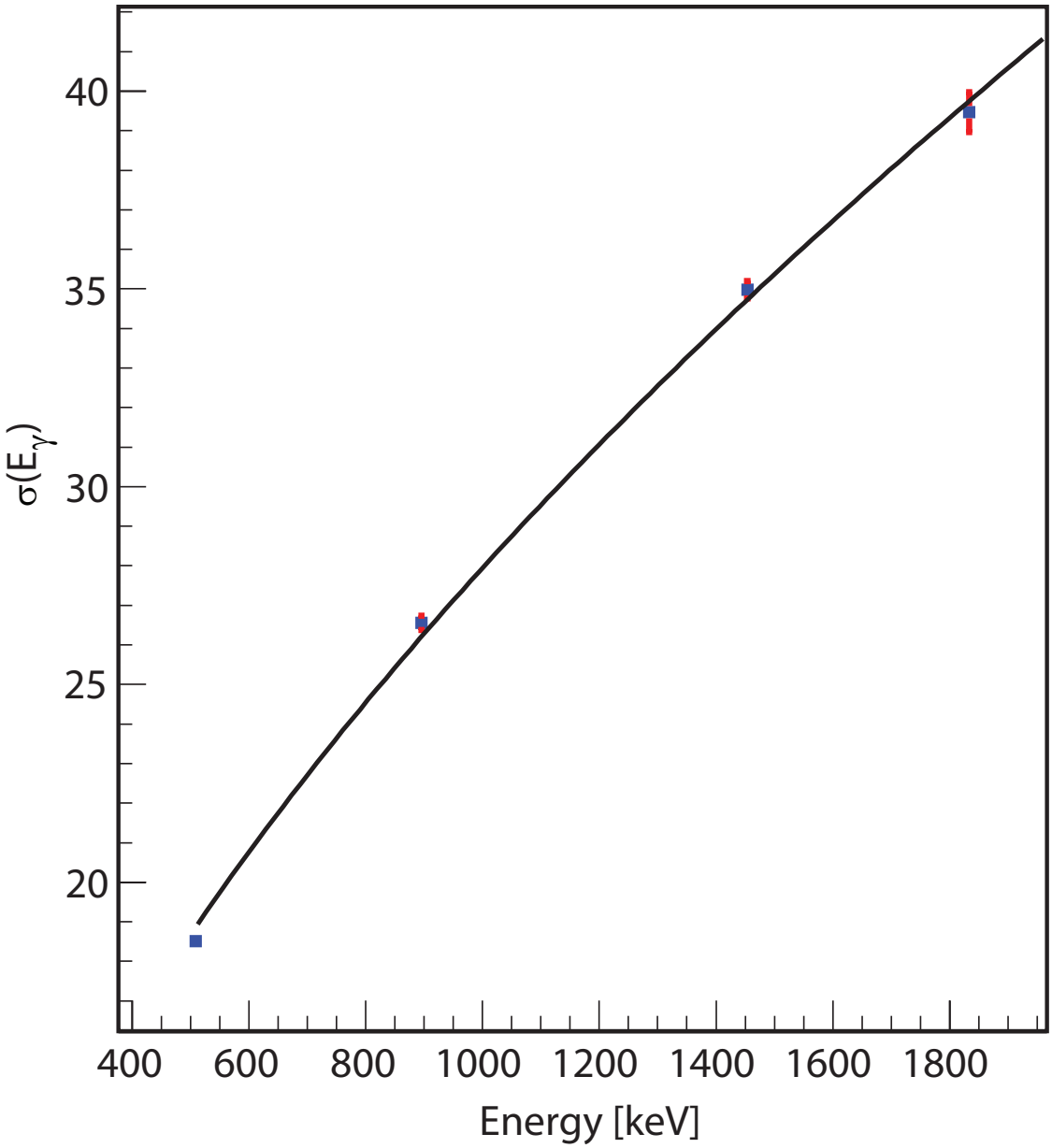

Figure 4.7: The width of a peak as a function of its energy for ring A. The FWHM of the peak is related to σ by $FWHM = 2\sqrt{2\ln 2}\sigma$.

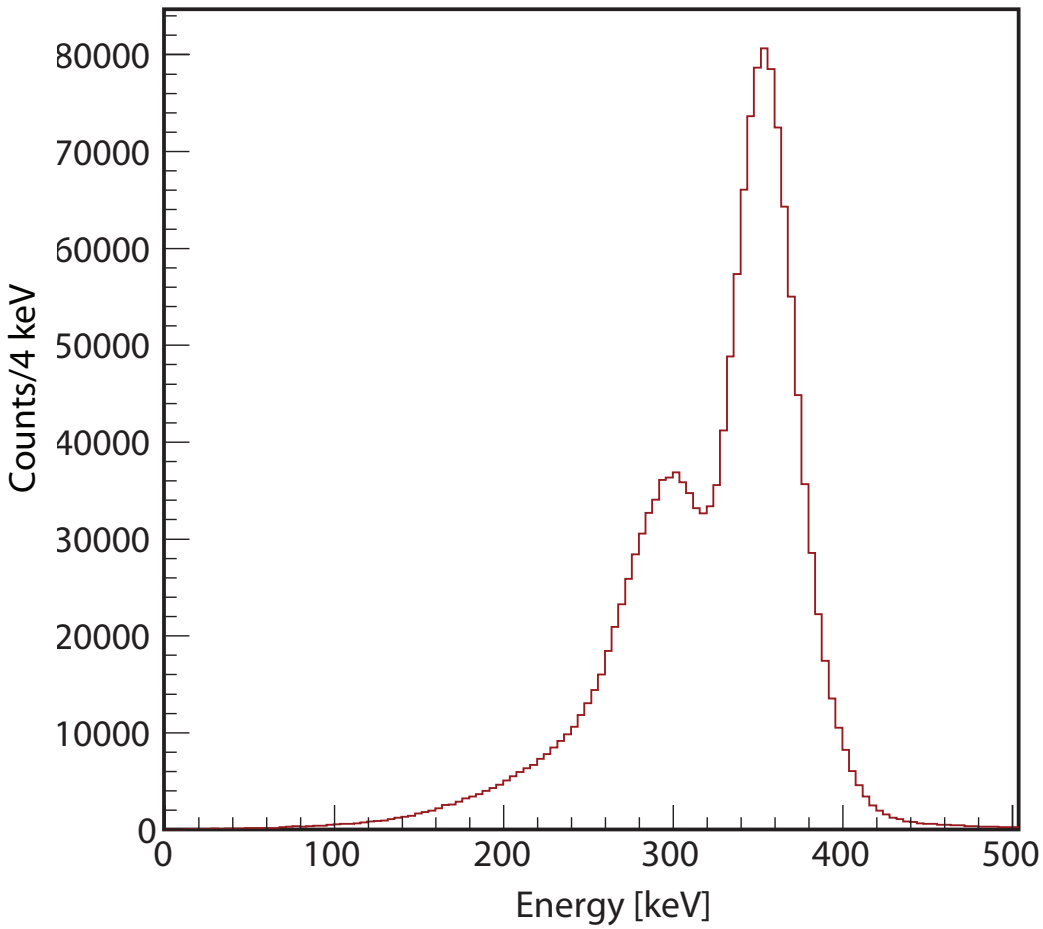

Figure 4.8: Decay spectrum of ^{133}Ba measured in CAESAR showing the 356 keV de-excitation γ ray and the impact of the energy threshold settings on low-energy γ rays.

the addback routine.

The energy thresholds were experimentally determined to be at $\approx$ 270 keV by placing a ^{133}Ba γ ray source in CAESAR. As Fig. 4.8 shows, the 356 keV γ ray from the decay of this source and the low-energy threshold are clearly visible.

The energy thresholds of all of the rings in CAESAR were fit with a Gaussian distribution, and the extracted full width at half maximum (FWHM) and mean value were used as inputs for the GEANT4 simulation for CAESAR, which models the energy threshold with

Ring	Mean (keV)	FWHM (keV)
A	254	99
B	255	94
C	259	96
D	268	101
E	265	80
F	312	126
G	259	133
H	273	142
I	261	125
J	235	158

Table 4.7: The mean and FWHM of the Gaussian distribution determined from data and used to describe the energy thresholds of the rings of CAESAR.

a Gaussian shape. The result of this fit to ring D in CAESAR is shown in Fig. 4.9; the mean value and FHWM of the Gaussian distribution for the rings in CAESAR are given in Tab. 4.7.

4.0.5.3 Efficiency of CAESAR

The absolute full-energy peak efficiency of CAESAR was determined by measuring the decay of the calibrated γ-ray sources, ^{22}Na, ^{137}Cs and ^{88}Y, which provide γ rays with energies between 511 keV and 1836 keV. The peak areas of the γ-ray transitions were determined by extrapolating a linear background to the spectrum beneath the peak and extracting the number of counts above this background. The absolute full-energy peak efficiency calibration for CAESAR obtained by this method is shown in Fig. 4.10. The results are agree with those shown by Weisshaar *et al.* [54], who used the same method to determined the absolute full-energy peak efficiency. The GEANT4 simulation successfully reproduces the measured efficiency, as Fig. 4.10 shows.

The in-beam efficiency of CAESAR is calculated with a GEANT4 simulation, which will be discussed subsequently. The absolute disagreement between the GEANT4 simulation and

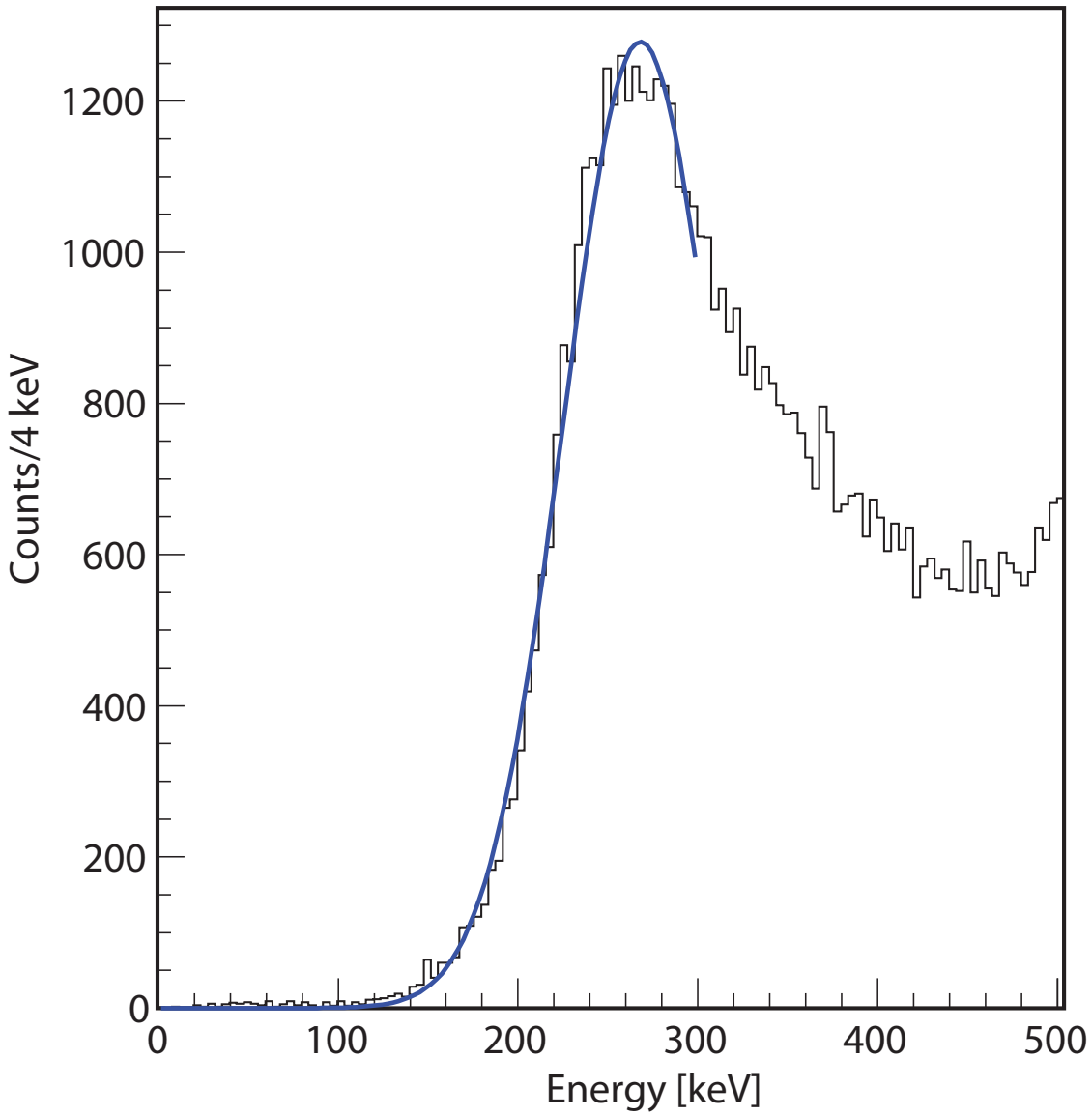

Figure 4.9: A Gaussian distribution (blue line) fit to the low-energy threshold of ring D.

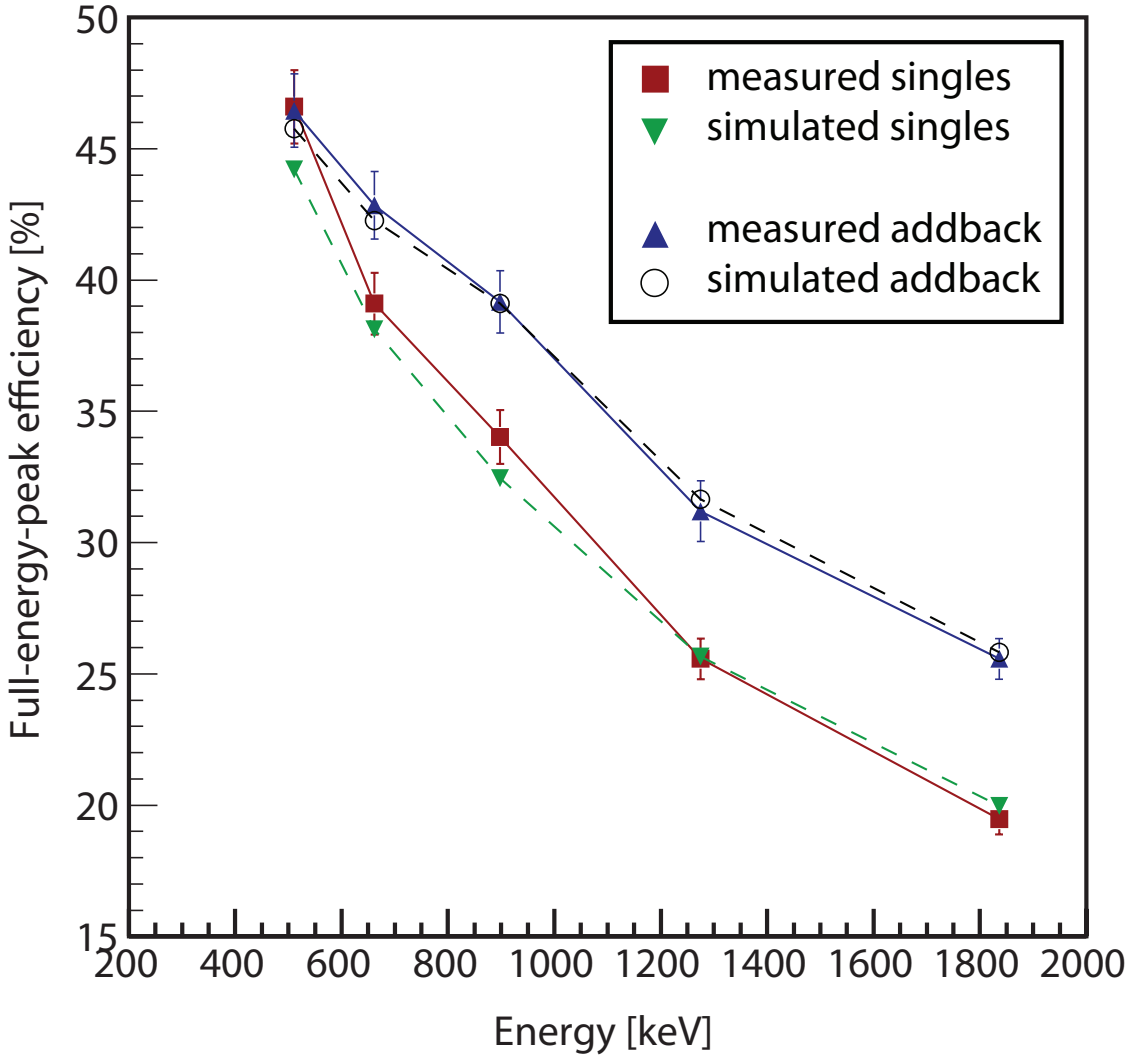

Figure 4.10: Absolute full-energy peak efficiency measured from calibrated γ ray sources. The red dashed line indicates the results of analysis without the nearest neighbor addback routine, the solid blue line shows the efficiency with addback. Both lines are only intended to guide the eye.

the measured efficiency is (at a maximum) 1%, so this is the adopted value for the absolute uncertainty of the efficiency ($\Delta\epsilon_{GEANT}$) of the GEANT4 simulation. It is also necessary to include the uncertainty in the initial activity of the calibration sources, which was 3% for all the sources used in this work.

4.0.5.4 Doppler Reconstruction

Gamma rays with energy E_γ emitted from a projectile moving with a velocity v are Doppler-shifted to a different energy (E_γ^{lab}) in the laboratory frame depending on their detection angle (θ_{lab}):

$$E_\gamma^{lab}\left(E_\gamma, \theta_{lab}\right) = \frac{E_\gamma}{\gamma\left(1 - \beta\cos\left(\theta_{lab}\right)\right)} \ , \tag{4.5}$$

where $\beta = v/c$ and $\gamma = 1/\sqrt{1-\beta^2}$. Doppler reconstructions were performed in order to determine the energy with which the γ rays detected in the experiments were emitted from the projectile.

The velocity of the projectile used for the Doppler reconstruction was selected depending on the approximated lifetime of the first 2^+ excited state in the projectile and the velocity of the projectile before the target. The velocity of the projectile before the target was determined from energy of the beam before the target (given in Tab. 4.3). The lifetimes of the first 2^+ excited states in $^{34-38}$Si can be estimated from their known $B(E2; 0^+ \rightarrow 2^+)$ values [17] (see Sec. 2.2.1). The $B(E2)$ values of ^{40,42}Si were not known, so the lifetime was estimated from predicted values, which will be discussed subsequently.

The target used for the intermediate-energy Coulomb excitation of $^{34-40}$Si was made of 268 μm thick ^{197}Au, while the target used for the intermediate-energy Coulomb excitation of ^{42}Si was made of 502 μm thick ^{209}Bi. In all but one case (the intermediate-energy Coulomb

isotope	τ (ps)	d (mm)	$\beta\gamma$ (v/c)
^{34}Si	0.15(7)$*$	0.02	0.39
^{36}Si	4.5(17)$*$	0.6	0.38
^{38}Si	17(8)$*$	2.2	0.39
^{40}Si	6$\star$	0.8	0.39
^{42}Si	14$\star$	1.7	0.37

Table 4.8: Estimated lifetimes of 2^+ excited states of $^{34-42}$Si, distance traveled before γ emission and velocity at γ-ray emission. The target for the intermediate-energy Coulomb excitation of $^{34-40}$Si was $\approx$ 0.268 mm thick ^{197}Au, for the intermediate-energy Coulomb excitation of ^{42}Si the target was $\approx$ 0.5 mm thick ^{209}Bi. Lifetimes for $^{34-38}$Si (marked with $*$) are from ENSDF [14], lifetimes for ^{40,42}Si (marked with $\star$) are predicted values [11].

excitation of ^{34}Si), the lifetime of the first 2^+ excited state was longer than the time required for the projectile to pass through the target. For these projectiles, the velocities at which the γ rays were emitted was taken to match the rigidity of the S800 spectrograph after the target, which was optimized for the transmission of the particle of interest to the focal plane of the S800.

As the lifetime of the first 2^+ excited state in ^{34}Si is short, 0.15(7) ps, the velocity of the projectile at emission was taken to be the velocity at mid-target. The lifetimes of the excited states, distances traveled after excitation, and velocities at γ ray emission for all the projectiles discussed in this work are shown in Tab. 4.8.

4.0.5.5 GEANT4 Simulation

A GEANT4 simulation for CAESAR was written by Baugher *et al.* [70] and models the effects discussed in the previous sections: the energy thresholds and measured energy resolution of CAESAR, the energy of the emitted γ ray, the lifetime of the state emitting the γ ray and the incoming velocity of the projectile. The simulation is sufficiently sophisticated

to model the energy loss of the projectile as it passes through the target, the absorbtion of γ rays in the target, the Lorentz boost, the Doppler shift, and the angular distribution of the emitted γ rays. The simulation includes aspects of the experimental setup, including the beam pipe and the aluminum housing of the detectors.

As shown in Fig. 4.11, the simulation successfully reproduces measured source data, analyzed without (panels a-c) and with (panels 1-3) the nearest neighbor addback routine, which improves the efficiency of CAESAR, as discussed in Sec. 3.4.2. The simulation also agrees with the measured efficiency, as shown in Fig. 4.10. Since the simulation accurately reproduces the measured data, it can be used to extract the number of γ rays emitted from a projectile in flight, as shown in the next section.

4.0.6 Extraction of Gamma-ray Yields

The number of de-excitation γ-rays produced in the intermediate-energy Coulomb excitation of $^{34-42}$Si were extracted by fitting the results of GEANT4 simulations of emitted γ rays to the measured data.

4.0.6.1 Background Reduction

A coincidence window between the S800 Spectrograph and CAESAR is opened each time a particle is detected in the e1 scintillator in the S800 focal plane. As Glasmacher points out [38], in intermediate-energy Coulomb excitation measurements, most of the particles which enter the focal plane will not have been excited by the target. These particles will open a coincidence window without having emitted a γ ray. The coincidence window is about 300 ns wide and CAESAR counts background at a rate of about 4 kHz, so the number of random

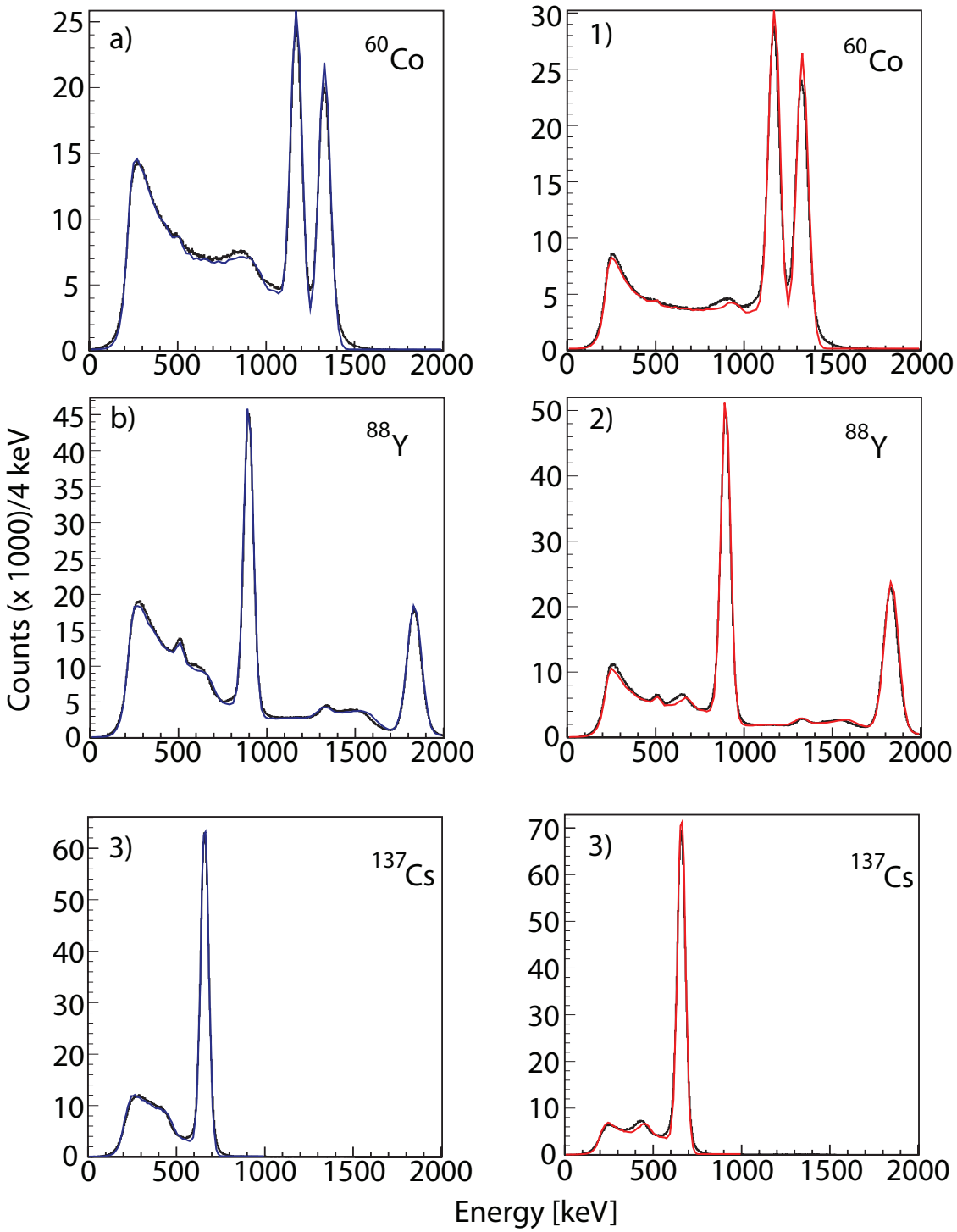

Figure 4.11: Comparison of measured and simulated γ-ray transitions from standard calibration sources. Panels a-c (left) show the measured (black) and simulated (blue) transitions for the decay of (from a) ^{60}Co, ^{88}Y and ^{137}Cs analyzed without addback. Panels 1-3 (right) show the measured (black) and simulated (red) transitions for the decay of the same three sources, but analyzed with addback.

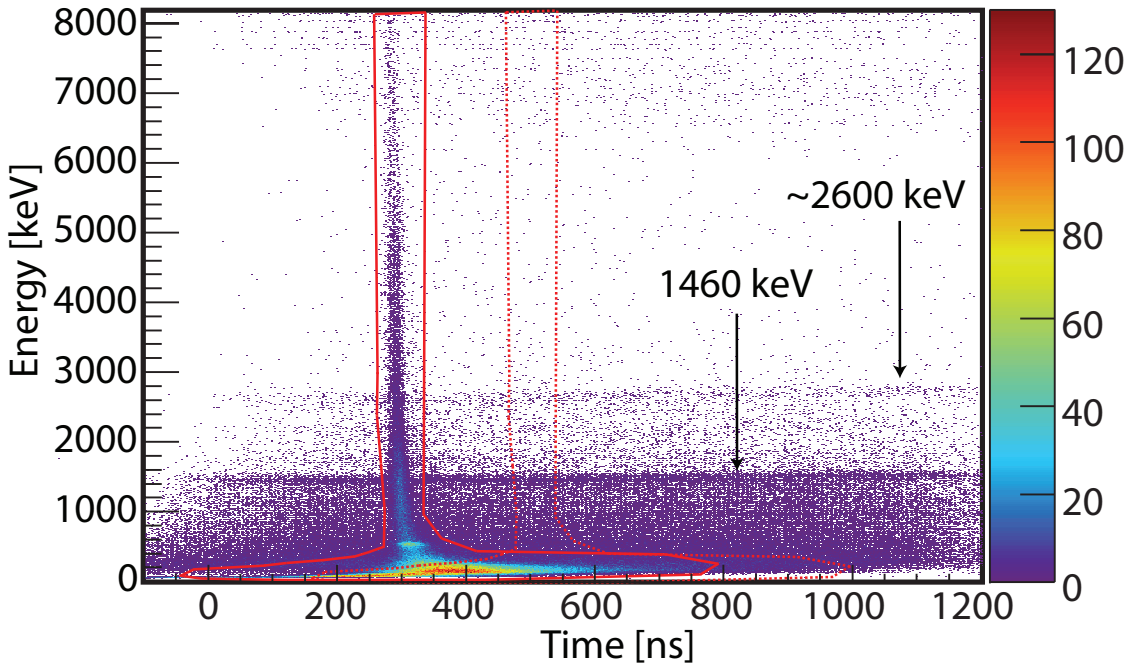

Figure 4.12: Correlation between non-Doppler-corrected γ-ray energy (y axis) and walk-corrected detector timing, measured with respect to the object scintillator (x axis), for the intermediate-energy Coulomb excitation of ^{38}Si. The prompt time-energy gate is shown by the solid red line, the off-prompt time-energy gate is shown by the dashed red line.

coincidences can be similar to the number of excited scattered particles in the focal plane[1].

Following the technique described by Weisshaar *et al.* [54], the number of random coincidences are reduced by the application of a two-dimensional time-energy gate condition to the γ-ray spectra (shown in Fig. 4.12 for the intermediate-energy Coulomb excitation of ^{38}Si). The detector timing is measured with respect to a thin plastic scintillator at the object position of the S800 spectrograph (see Fig. 3.3), so events measured in CAESAR are correlated in time with particles detected in the S800 focal plane. The two-dimensional time-energy gate condition can remove many of the random coincidences from room background from the γ ray spectra, without impacting the coincidences with prompt γ rays.

[1]For example, in the case of ^{38}Si, the cross section to the first 2^+ excited state is $\sigma \approx 48$ mb and the target was 518 mg/cm^2 thick ^{197}Au, so approximately 1 excited ^{38}Si nucleus is expected for every 13,000 ^{38}Si incident on the target.

A comparison of the γ-ray spectra, without a Doppler-correction applied, from intermediate-energy Coulomb excitation of $^{34-40}$Si with and without the time-energy gate applied is shown in Fig. 4.13. The time-energy gate reduces the number of off-prompt γ rays in the γ-ray spectra without impacting the peak area of the prompt transitions. The time-energy gate condition almost entirely removes the room background peak at 1460 keV from the γ-ray spectra, without changing the peak area from the prompt de-excitation of the excited state at 547 keV produced by the intermediate-energy Coulomb excitation of the ^{197}Au target by the projectile. The same comparison for same cases, but with a Doppler-correction applied, is shown in Fig. 4.14. Again, the two-dimensional time-energy gate removes the random coincidences with room background without impacting the coincidences with prompt γ rays.

The γ-ray background can be further reduced by offsetting the time-energy gate in time, so that it samples the room background, and subtracting the resulting background spectra from the spectra measured with the prompt two-dimensional time-energy gate. The choice made for this gate condition did not have an impact on the number of coincidences in the full-energy peak.

The results of such a background subtraction are shown for spectra analyzed without a Doppler correction applied in Fig. 4.15. As this figure shows, the background subtraction removes the remaining background peak at 1460 keV without impacting the peak areas corresponding to the prompt transitions. The results of such a background subtraction are shown for spectra analyzed with a Doppler correction applied in Fig. 4.16.

The intermediate-energy Coulomb excitation of ^{42}Si was performed with a 492 mg/cm^2 thick ^{209}Bi target. The ground state of ^{209}Bi has a spin and parity of $J^\pi = 9/2^-$ and the first excited state in ^{209}Bi, at 896.28(6) keV, has spin and and parity of $J^\pi = 7/2^-$ [71]. The adopted $B(E2; 9/2^- \rightarrow 7/2^-)$ value for the transition between the ground state and

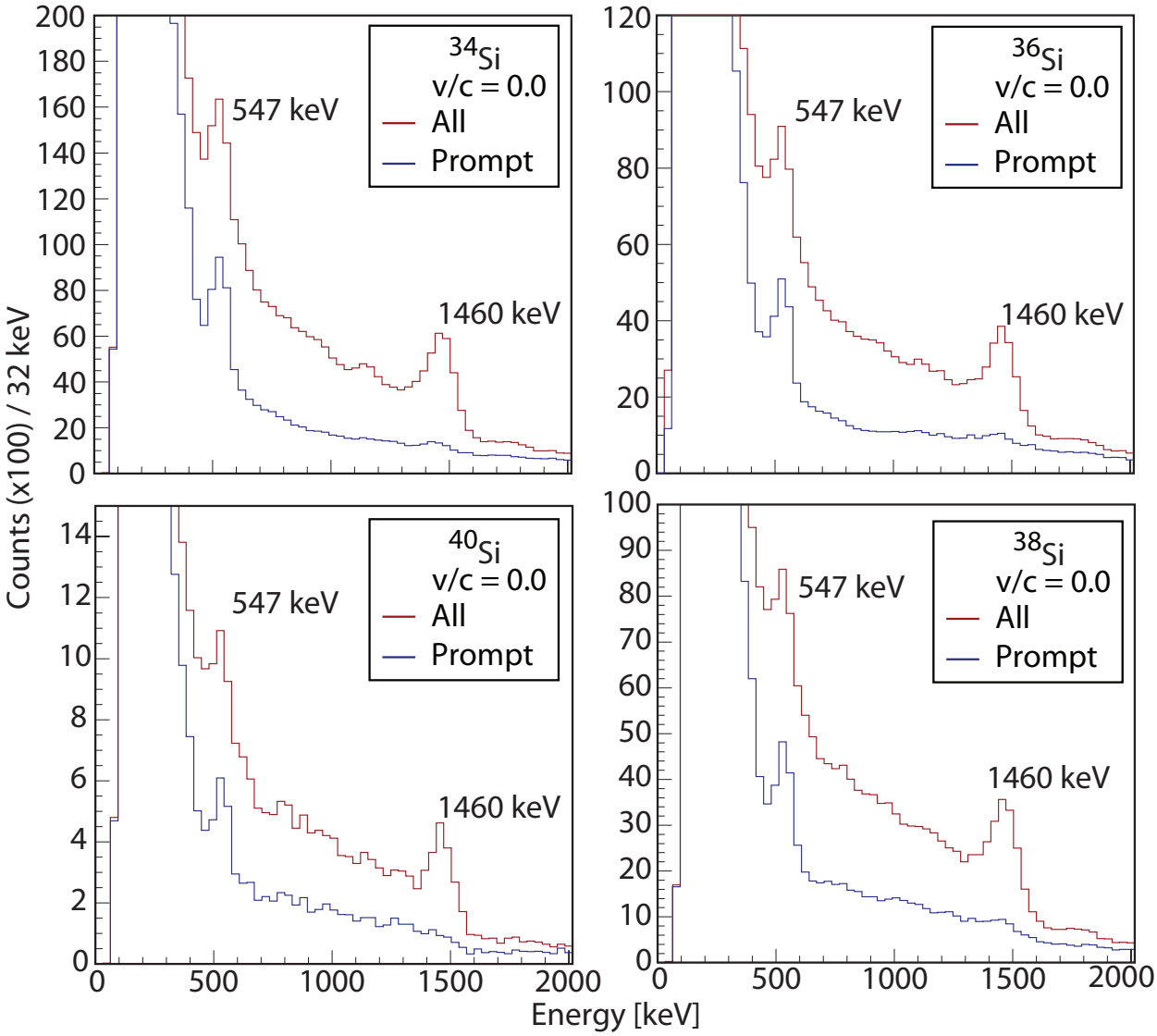

Figure 4.13: Measured γ-ray spectra from the intermediate-energy Coulomb excitation of $^{34-40}$Si, analyzed with the nearest neighbor addback routine and without a Doppler correction applied. The spectra in red were analyzed without the time-energy gate condition applied, the spectra in blue with the time-energy gate condition. The peak at 547 keV corresponds to the prompt decay of an excited state in the target, produced in the intermediate-energy Coulomb excitation of the ^{197}Au target by the projectile. The peak at 1460 keV result of a random coincidence with the decay of ^{40}K and is part of the room background. The time-energy gate reduces the random particle-γ coincidences without impacting the number of prompt γ rays.

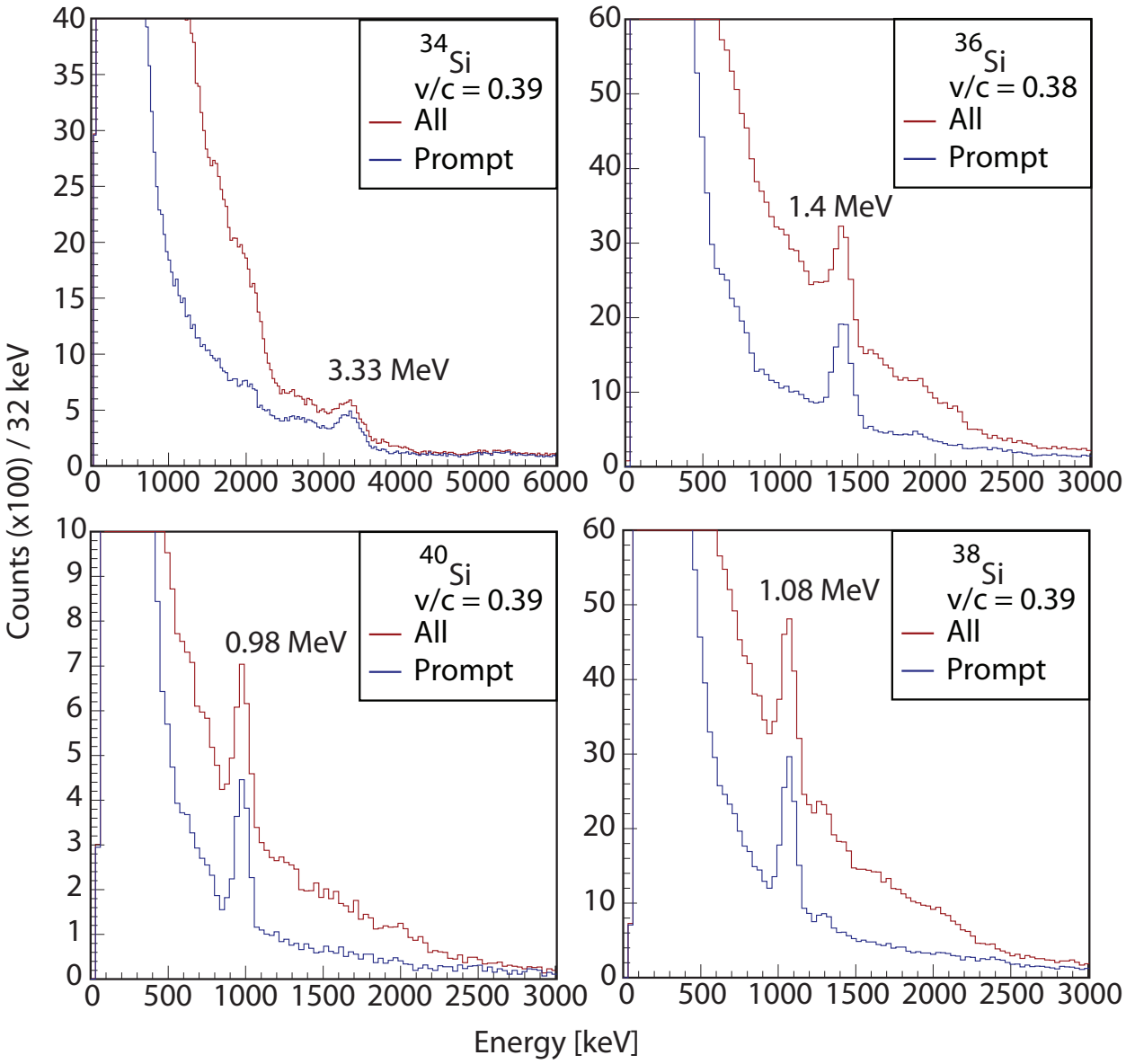

Figure 4.14: Measured γ-ray spectra from the intermediate-energy Coulomb excitation of $^{34-40}$Si, analyzed with the nearest neighbor addback routine and with a Doppler correction applied. The spectra in red were analyzed without the time-energy gate condition applied, the spectra in blue with the time-energy gate condition. The measured γ-ray energies are from the de-excitation of the first 2^+ excited states with in the projectiles and agree with the energies measured by Ibbotson *et al.* [17] (for $^{34-38}$Si) and Campbell *et al.* [18, 19, 20] (for ^{40}Si).

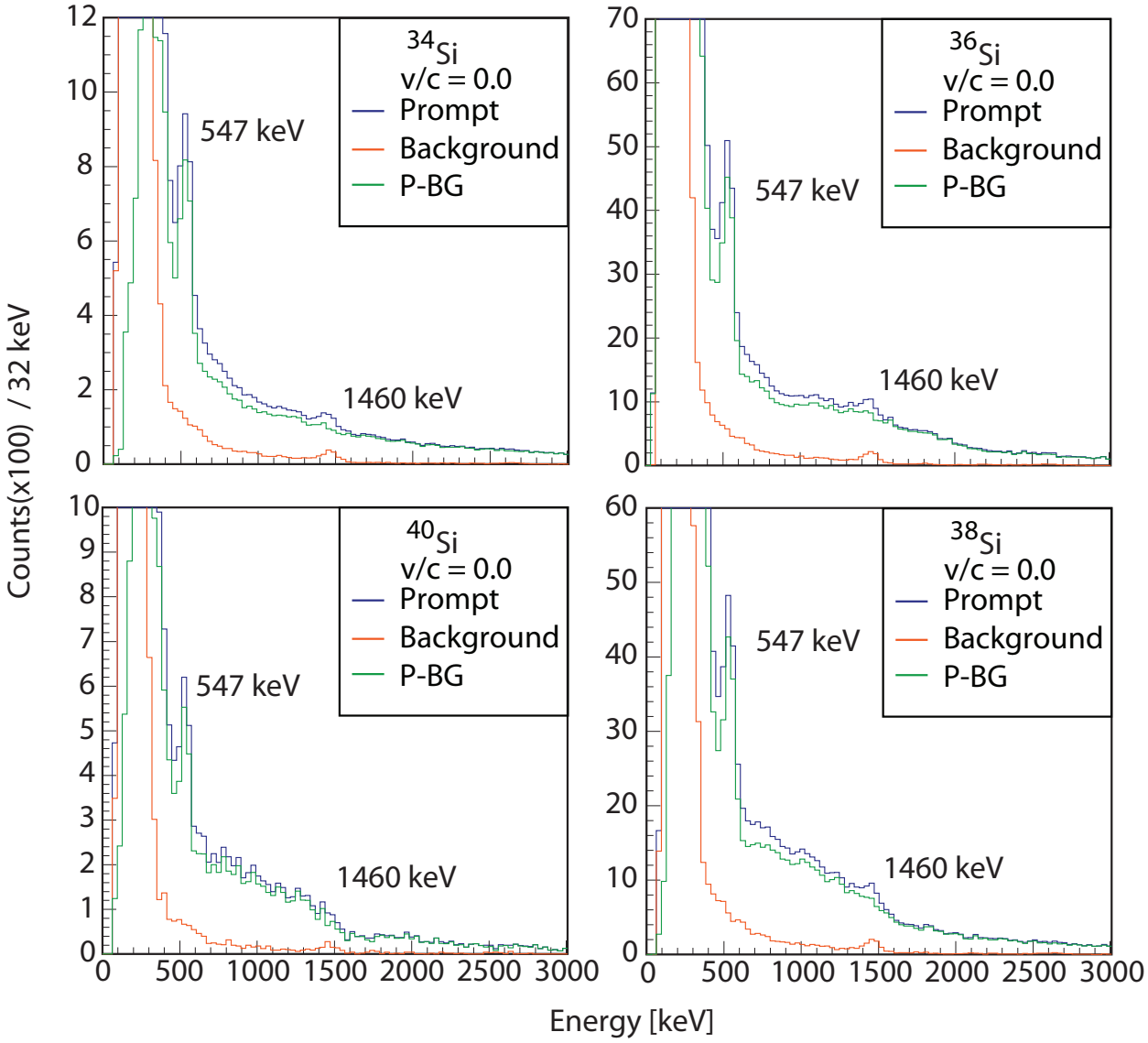

Figure 4.15: Measured γ-ray spectra from the intermediate-energy Coulomb excitation of $^{34-40}$Si, analyzed with the nearest neighbor addback routine and without a Doppler correction applied. The spectra in shown in blue were analyzed with prompt time-energy gate condition applied, the spectra in orange were analyzed with the background time-energy gate condition applied. The spectra shown in green are the result of the subtraction of the background spectra from the prompt spectra.

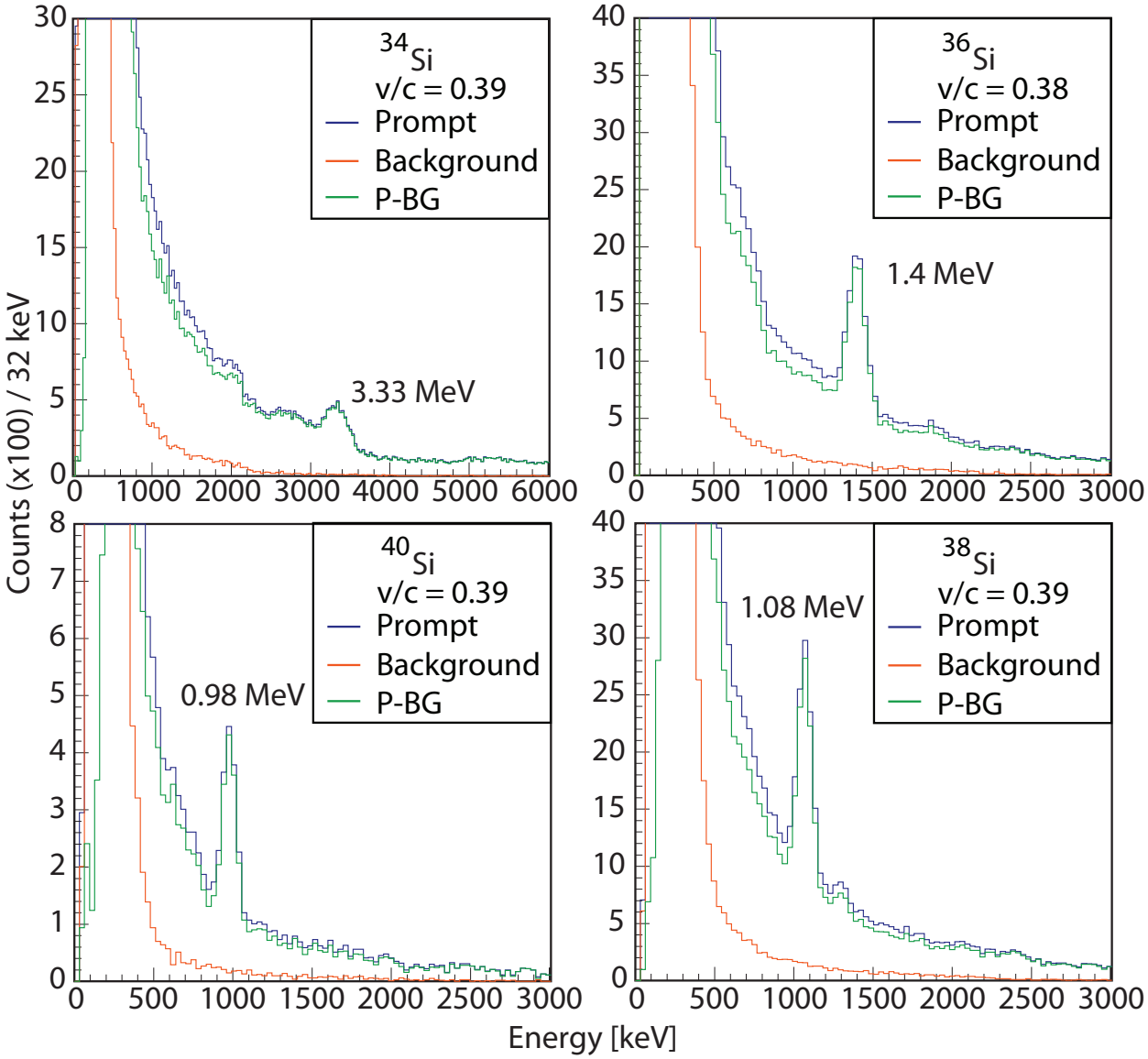

Figure 4.16: Measured γ-ray spectra from the intermediate-energy Coulomb excitation of $^{34-40}$Si, analyzed with the nearest neighbor addback routine and with a Doppler correction applied. The spectra in shown in blue were analyzed with prompt time-energy gate condition applied. The spectra in orange were analyzed with the background time-energy gate condition applied. The spectra shown in green are the result of the subtraction of the background spectra from the prompt spectra.

the first excited state is 27.5(14) e^2 fm^4 [71], so the expected intermediate-energy Coulomb excitation cross section is less than 1 mb for this case. Since this cross section is two orders of magnitude smaller than the expected intermediate-energy Coulomb excitation cross section for ^{42}Si, the number of de-excitation γ rays emitted from the excited state in the target are not expected to significantly contribute to the measured γ-ray spectrum.

The ^{209}Bi target was chosen in order to ensure that no γ rays emitted at rest from the target would be shifted to the expected energy of the de-excitation γ ray from the projectile (measured to be 770(19) keV by Bastin *et al.* [21]) by the application of the Doppler correction. Gamma-ray spectra measured during this experiment, analyzed with a Doppler correction applied and with and without the two-dimensional time-energy gate applied are shown in Fig. 4.17. The expected transition at $\simeq$ 770 keV [21] is clearly visible.

4.0.6.2 Fit of the Experimental Spectra with the GEANT4 Simulation

In order to determine the cross section for the intermediate-energy Coulomb excitation of a nucleus, the number of de-excitation γ rays emitted by the state excited in this reaction must be determined.

The γ-ray spectra measured in-beam have characteristic features. The spectra analyzed without the application of a Doppler correction (c.f. Fig. 4.15) show evidence of the de-excitation of the $7/2^+$ excited state in the ^{197}Au target; a peak at 547 keV. This peak from the de-excitation of a target nucleus is convoluted with a peak at 511 keV, which is attributed to pair production and subsequent positron annihilation in CAESAR. The spectra analyzed with the application of a Doppler correction (c.f. Fig. 4.16) have a peak at the expected energy of the de-excitation γ ray emitted from the first 2^+ excited state in the projectile. The γ ray spectra produced by γ rays emitted in the de-excitation of excited states in the

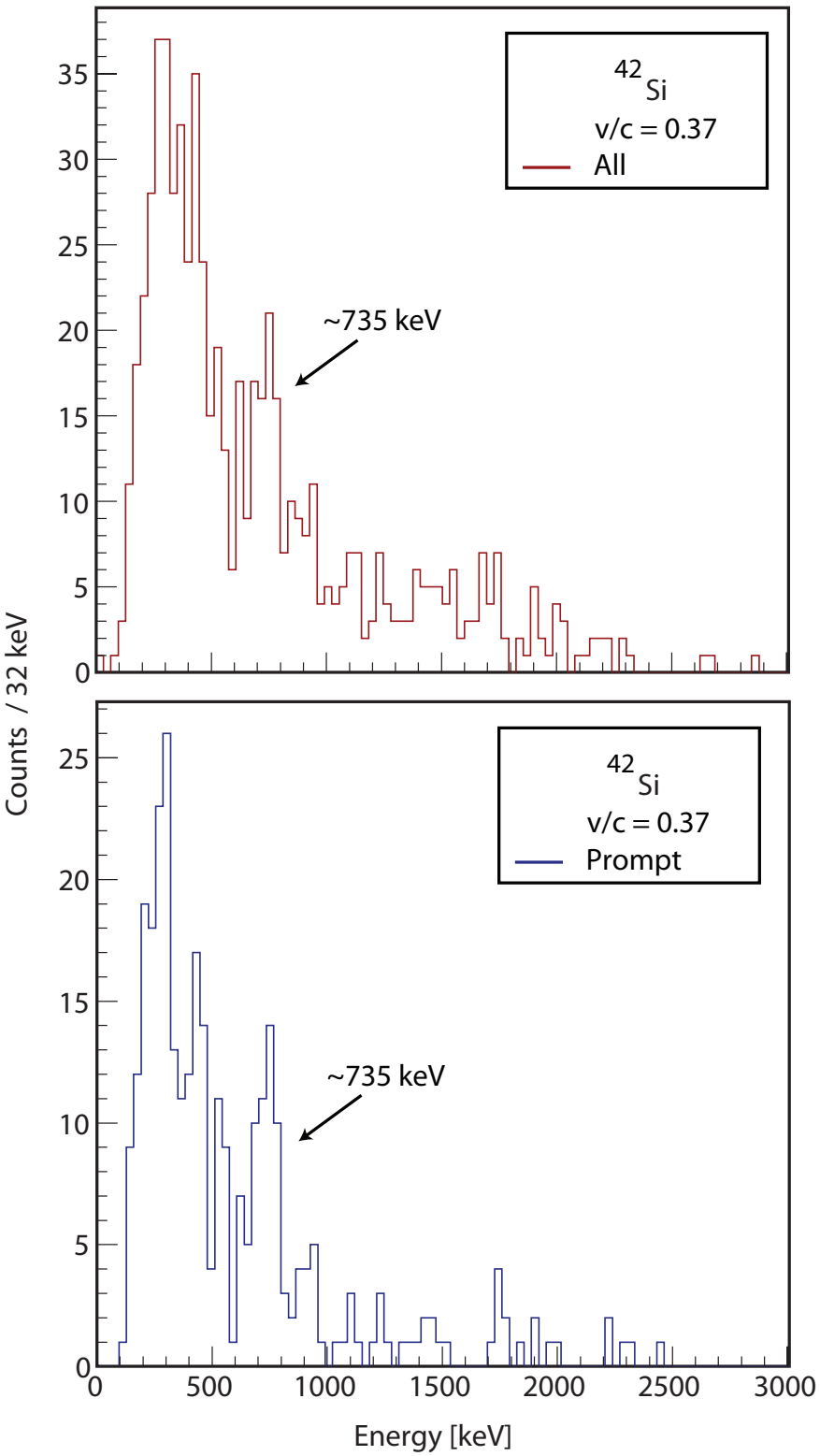

Figure 4.17: Measured γ-ray spectra from the intermediate-energy Coulomb excitation of ^{42}Si, analyzed with the nearest neighbor addback routine and with a Doppler correction (with v/c = 0.37) applied. The spectrum shown in blue was analyzed with prompt time-energy gate condition applied, the spectrum in red was analyzed without this condition.

target or projectile, as well as the γ ray spectrum of the 511 keV γ ray, are simulated by the GEANT simulation. Although the 511 keV γ rays are likely created by pair production and positron annihilation events in the CsI(Na) crystals composing CAESAR, they are modeled by the GEANT simulation as being single γ rays isotropically emitted from the position of the target, since they are only used to describe the shape of the spectra.

All the γ-ray spectra measured in beam shown in this work have in common a prompt background, attributed mainly to atomic processes [65]. This prompt background is described here by the sum of two exponential functions. This is a common approach to describe the prompt background, see [72, 73, 74].

Gamma-ray spectra produced by the GEANT4 simulation, as well as the double exponential function describing the prompt background, were fit to the measured prompt, background-subtracted γ-ray spectra discussed in the previous section.

In order to determine the number of γ rays emitted from the excitation of the ^{197}Au target by the projectiles, it was first necessary to disentangle the contribution to γ-ray spectra of the 547 keV γ ray and the of 511 keV γ ray. This was done by applying two gate conditions to the γ-ray spectra. The first gate condition (which this work will call the "hit 1 condition") was satisfied by events in which only one detector in CAESAR registered an event which met the two-dimensional energy-time gate condition discussed in the previous section. The second gate condition (which this work will call the "not hit 1 condition") was satisfied by events in which more than one detector registered events meeting the two-dimensional energy-time gate condition. These spectra were analyzed with the addback procedure applied. The efficiency of CAESAR at the energy of interest is similar for singles and addback, as Fig. 4.10 shows, so this choice is justified.

The spectra analyzed with these gate conditions applied for the intermediate-energy

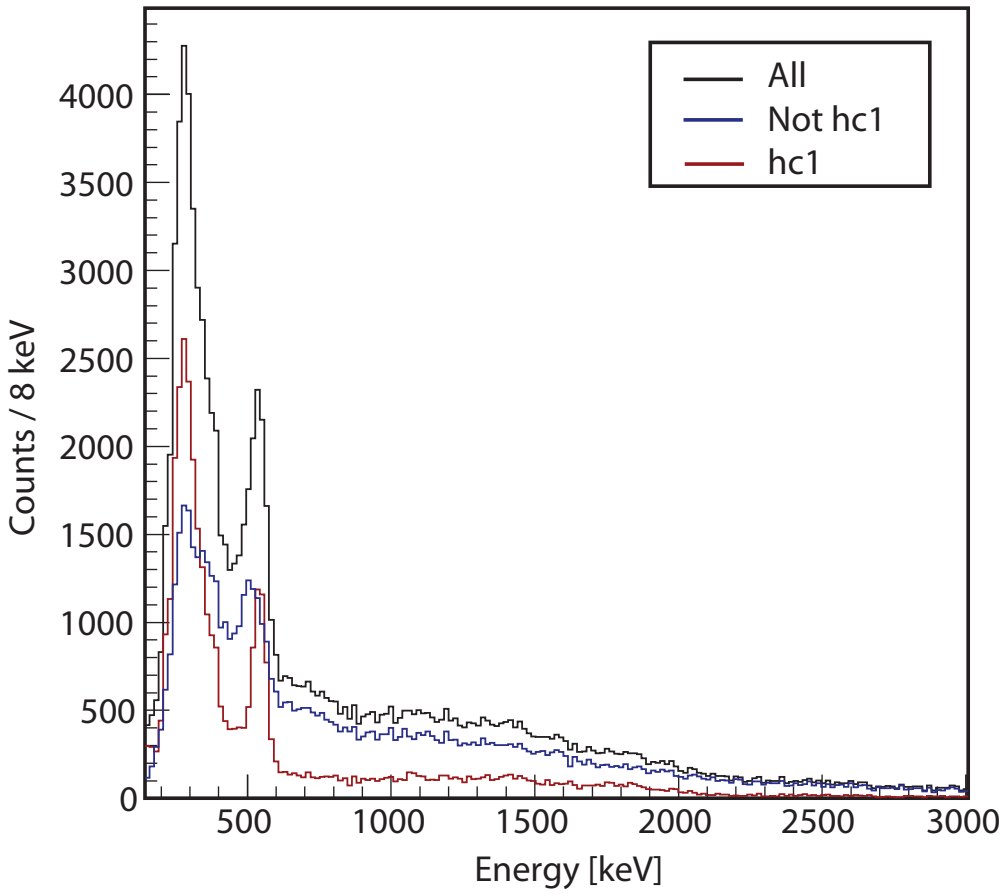

Figure 4.18: Measured prompt, background-subtracted γ-ray spectra, analyzed without the application of a Doppler correction and with the addback procedure, from the intermediate-energy Coulomb excitation of ^{36}Si. The spectrum analyzed with the "hit 1 condition" applied is shown in red (labeled "hc1"), the spectrum analyzed with the "not hit 1 condition" applied is shown in blue (labeled "not hc1"), and the spectrum analyzed without either condition applied is shown in black.

Coulomb excitation of ^{36}Si are shown in Fig. 4.18. As this Fig. shows, most of the events corresponding to the detection of 547 keV γ rays satisfied the "hit 1 condition", with a small number of these events satisfying the "not hit 1 condition", while virtually none of the events corresponding to the detection of a 511 keV γ ray satisfied the "hit one condition". This is expected, as the 511 keV γ rays are a result of processes in which more than one γ ray is emitted and the efficiency of CAESAR for detecting 511 keV γ rays is high (as demonstrated in Fig. 4.10).

The function used to fit the spectra analyzed with the "hit 1 condition" applied was the sum of the double exponential function used to describe the prompt background, the simulated full-energy spectrum of the 547 keV γ rays and the simulated full-energy spectrum of the Doppler-shifted γ rays emitted from the projectile:

$$f(x) = p_1 \cdot e^{-p_0 \cdot x} + p_3 \cdot e^{-p_2 \cdot x} + p_4 \cdot S_{Au}(x) + p_5 \cdot S_{Si}(x) \ . \tag{4.6}$$

Where p_i are the fit parameters, the 547 keV γ ray was simulated as being emitted at rest (S_{Au}), and the γ ray resulting from the de-excitation of the first 2^+ state in the projectile (S_{Si}) was simulated as being emitted in flight. The spectra of the 511 and 547 keV γ rays are nearly identical after Doppler-reconstruction and are only used to describe the background. The resulting fit is shown for the intermediate-energy Coulomb excitation of ^{36}Si in the upper panel of 4.19. The simulations of the full-energy spectra of the of the γ rays emitted at rest and in flight included both the energy-dependent energy resolution calibration discussed in Sec. 3.2.1.4 and the effects of the energy thresholds discussed in Sec. 4.0.5.2.

The function used to fit the spectra analyzed with the "not hit 1 condition" applied was the sum of the double exponential function used to describe the prompt background, the

simulated full-energy spectrum of the 511 keV γ rays, the simulated full-energy spectrum of the 547 keV γ rays and the simulated full-energy spectrum of the Doppler-shifted γ rays emitted from the projectile:

$$f(x) = p_1 e^{-p_0 \cdot x} + p_3 e^{-p_2 \cdot x} + p_4 \cdot S_{511}(x) + p_5 \cdot S_{Au}(x) + p_6 \cdot S_{Si}(x) \ . \tag{4.7}$$

Where the 547 keV and 511 γ rays were simulated as being emitted at rest (S_{Au}, S_{511}) and the γ ray resulting from the de-excitation of the first 2^+ state in the projectile was simulated as being emitted in flight (S_{Si}). The resulting fit is shown for the intermediate-energy Coulomb excitation of ^{36}Si in the lower panel of 4.19. The total number of 547 keV γ rays emitted from the target is determined from the sum of the number of 547 keV γ rays in the spectra analyzed with the "hit 1" and "not hit 1" conditions applied.

The function used to fit the Doppler-corrected spectra from the intermediate-energy Coulomb excitation of $^{34-40}$Si was the sum of the double exponential function describing the prompt background, the simulated Doppler-corrected full energy spectra of the 511 and 547 keV γ rays, and the simulated Doppler-corrected spectrum of the γ rays emitted from the projectile:

$$f(x) = p_1 \cdot e^{-p_0 \cdot x} + p_3 \cdot e^{-p_2 \cdot x} + p_4 \cdot \big(S_{511}(x) + S_{Au}(x)\big) + p_5 \cdot S_{Si}(x) \ . \tag{4.8}$$

Where p_i are fit parameters and $S_{511,\ \mathrm{Au}}(x)$ are the simulated 511 keV and 547 keV γ-ray spectra. These γ rays were simulated to be emitted at rest and Doppler-corrected with the velocity of the projectile. These two γ rays are separated in energy by 36 keV and their Doppler-corrected energy spectra are nearly identical. The function used to fit the measured

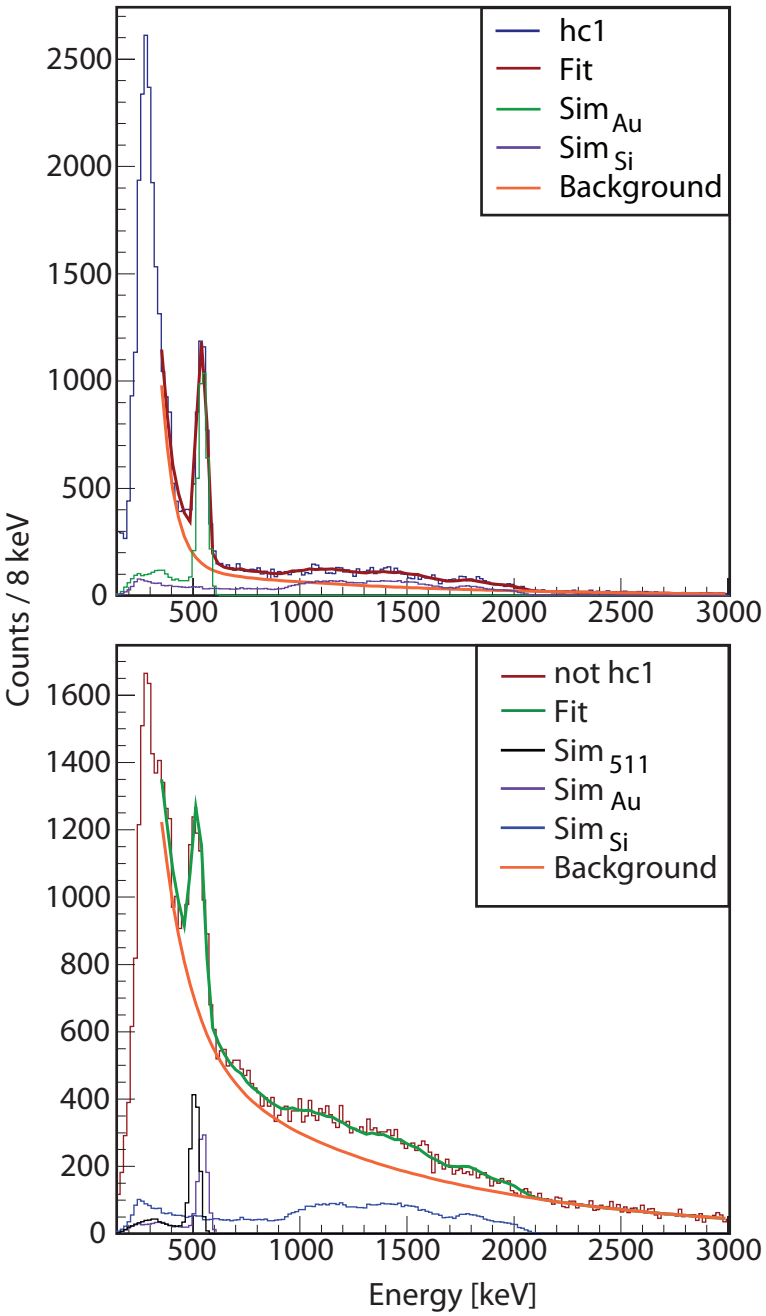

Figure 4.19: Measured prompt, background-subtracted γ-ray spectra, analyzed without the application of a Doppler correction and with the addback procedure, from the intermediate-energy Coulomb excitation of ^{36}Si and the fit of γ ray spectra produced GEANT4 simulation to these data. Top: the result of analysis with the "hit 1 condition" applied (labeled "hc1") and the fit function (equation 4.6) discussed in the text applied. Bottom: the result of analysis with the "not hit 1 condition" applied (labeled "not hc1") and the fit function (equation 4.7) discussed in the text applied.

spectra included their contribution as the sum of the two simulated spectra. $S_{\mathrm{Si}}(x)$ is the simulated γ-ray spectrum resulting from the de-excitation of the the first 2^+ excited state in the projectile. These γ rays were simulated to be emitted at the velocity of the projectile were Doppler-corrected to the energy of emission in the projectile frame.

The fit region was chosen to include the Doppler-corrected peak emitted by the projectile and the Doppler-shifted γ rays emitted from the target. The fit function included the contribution of the 547 keV γ ray from the ^{197}Au target and 511 keV γ rays (both emitted at rest with respect to CAESAR) from pair-production and positron annihilation (see Sec. 3.3.1) as the sum of their simulated Doppler-shifted energies.

The results of these fits for the γ-ray spectra measured in the intermediate-energy Coulomb excitation of $^{34-40}$Si are shown in Fig. 4.20.

The function used to fit the prompt, Doppler-corrected spectrum from the intermediate-energy Coulomb excitation of ^{42}Si was the sum of the double exponential function describing the prompt background and the simulated Doppler-corrected full-energy spectrum of the γ rays emitted from ^{42}Si in flight:

$$f(x) = p_1 \cdot e^{-p_0 \cdot x} + p_3 \cdot e^{-p_2 \cdot x} + p_4 \cdot S_{Si}(x) \ . \tag{4.9}$$

at the level of statistics present in the γ ray spectra measured in the intermediate-energy Coulomb excitation of ^{42}Si, the contribution to the spectra from 511 keV γ rays produced in pair-production or positron annihilation in the detectors in CAESAR is negligible, so there was no need to include any simulated γ rays besides the de-excitation γ ray from the first 2^+ excited state in ^{42}Si (S_{Si}) in the fit function. The result of the fit to the data is shown in Fig. 4.21.

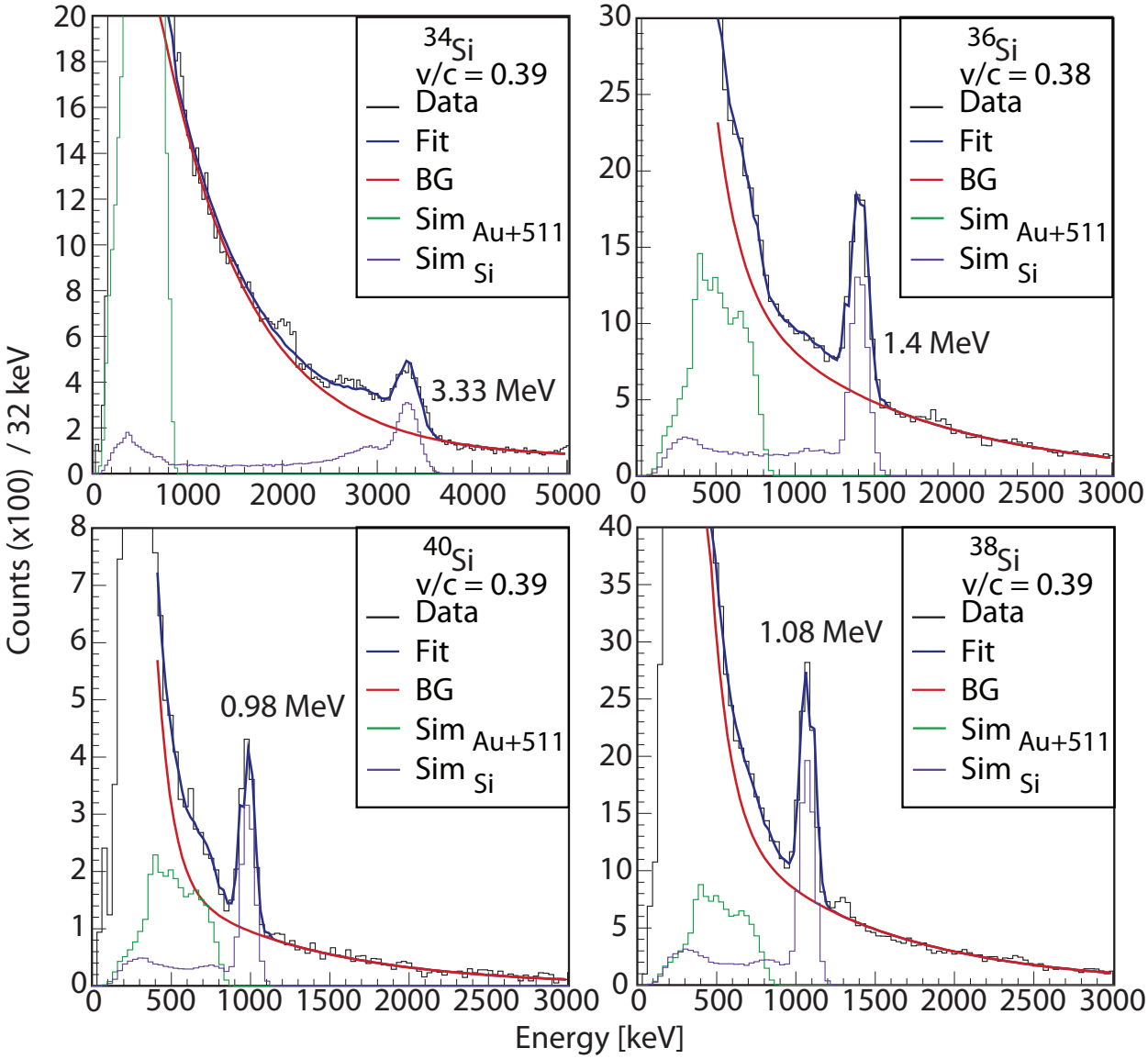

Figure 4.20: Measured prompt, background-subtracted, Doppler-corrected γ-ray spectra from the intermediate-energy Coulomb excitation of $^{34-40}$Si and the fit of the GEANT4 simulation (blue lines) to these data. The simulated spectra shown are from the de-excitation γ ray emitted by the first 2^+ excited state in $^{34-40}$Si (in violet) and the summed Doppler-shifted contribution from the 547 keV γ ray (emitted at rest in the excitation of the ^{197}Au target by the projectile) and from the 511 keV γ ray produced in pair production or position annihilation and emitted at rest (in green).

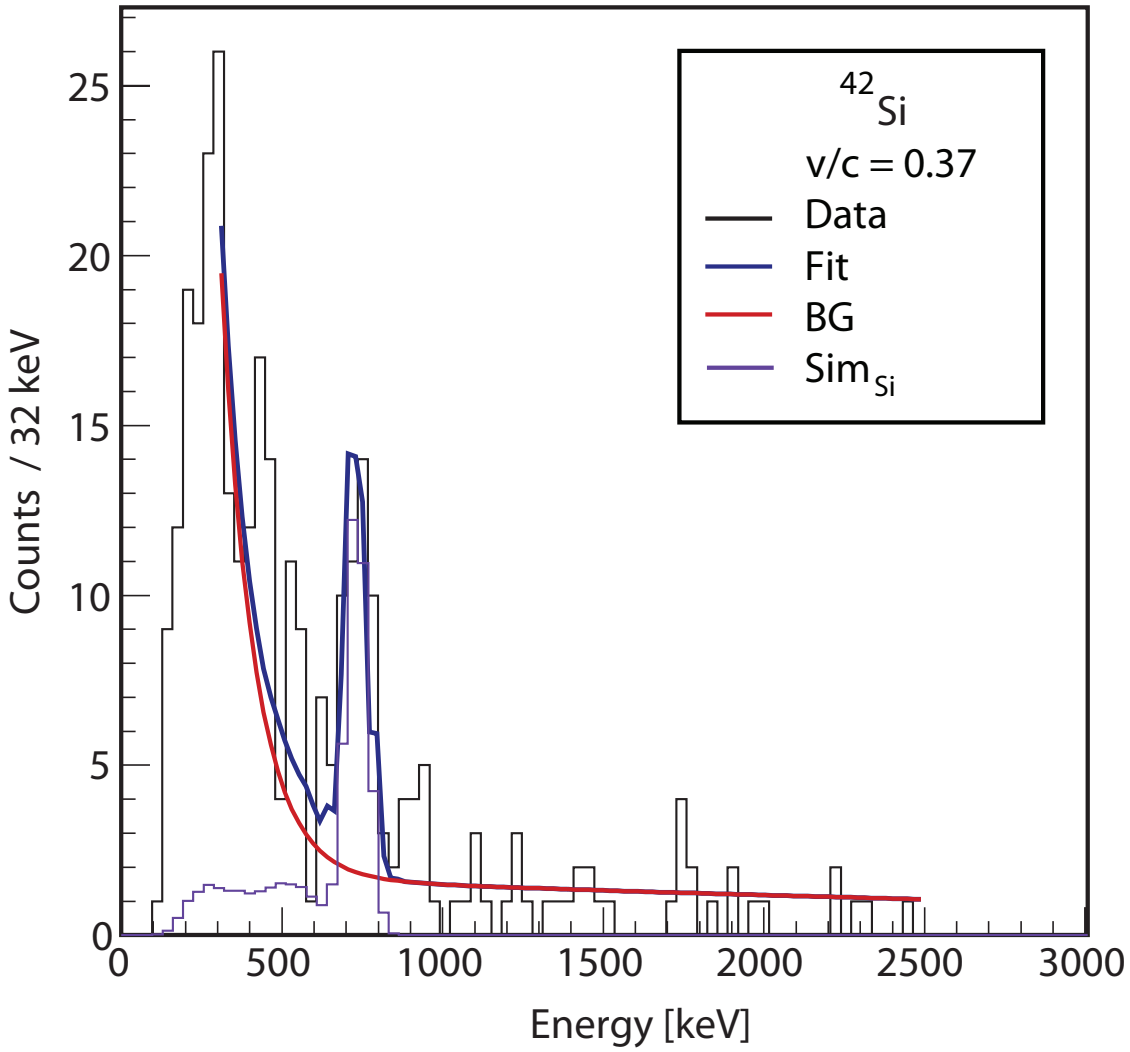

Figure 4.21: Measured prompt γ-ray spectra analyzed with the application of a Doppler correction and the addback procedure from the intermediate-energy Coulomb excitation of ^{42}Si and the fit of the function discussed in the text (blue line - Eq. 4.9) to these data. The simulated spectrum shown is from the de-excitation γ ray emitted by the first 2^+ excited state in ^{42}Si (in violet).

The number of γ rays emitted is extracted from the fit functions by multiplying the number of γ rays simulated by the GEANT4 simulation (which was fixed at 100,000 events for all the simulated full-energy spectra used to fit the cases discussed in this section) by the fit function parameter corresponding to the full-energy spectrum of the the γ ray. The uncertainty of this quantity is given by the uncertainty of the fit parameter (p_i), the uncertainty in the efficiency of the GEANT4 simulation (which was $\delta_{GEANT} = \Delta\epsilon_{GEANT}/\epsilon_{GEANT}$, with $\Delta\epsilon_{GEANT} = 1\%$ as discussed in Sec. 4.0.5.3), and the uncertainty in the accuracy of the calibration of the source used to measure the efficiency of CAESAR ($\delta_{source} = 3\%$):

$$\delta N_\gamma = N_\gamma \sqrt{\delta^2_{source} + \delta^2_{GEANT} + \left(\frac{\delta p_i}{p_i}\right)^2} \tag{4.10}$$

The number of γ rays detected for the de-excitation of the ^{197}Au target together with their associated uncertainty, are given in Tab. 4.9. The final number of γ-rays given in Tab. 4.9 includes a 5.9(4)% correction to account for the decay of the excited state to states other than the ground state [76]. The number of γ rays detected for the de-excitation of the excited states in the silicon nuclei of interest are given in Tab. 4.10. As the efficiency of detection is accurately reproduced by the GEANT4 simulation, the numbers given in the table are the number of γ rays emitted from the projectile or target absent a correction for the livetime of the data acquisition, which will be discussed in the next section. The γ-ray spectra from which these numbers were extracted were analyzed with the gate condition of the safe scattering angle for intermediate energy Coulomb excitation.

isotope	p_{Au}	δ_{GEANT}	N_γ
^{34}Si	0.11794(278)	0.024	12490(566)
^{36}Si	0.06573(202)	0.024	6902(341)
^{38}Si	0.06083(194)	0.024	6442(323)
^{40}Si	0.00735(77)	0.024	772(86)

Table 4.9: The number of γ rays corresponding to the de-excitation of the excited state in the ^{197}Au target, extracted following the procedure outlined in the text from the measured spectra analyzed subject to the condition of scattering $\theta \leq \theta^{max}$, where θ^{max} is the safe angle for intermediate-energy Coulomb excitation.

isotope	p_{Si}	δ_{GEANT}	N_γ
^{34}Si	0.08807(277)	0.108	8807(1028)
^{36}Si	0.11132(250)	0.037	11132(588)
^{38}Si	0.12086(246)	0.030	12086(571)
^{40}Si	0.01724(88)	0.030	1724(115)
^{42}Si	0.00057(14)	0.026	57(14)

Table 4.10: The number of γ rays corresponding to the de-excitation of the excited state in the projectile, extracted following the procedure outlined in the text from the measured spectra analyzed subject to the condition of scattering $\theta \leq \theta^{max}$, where θ^{max} is the safe angle for intermediate-energy Coulomb excitation.

4.1 Intermediate-Energy Coulomb Excitation Cross Sections

The excitation cross sections for intermediate-energy Coulomb excitation are used to deduce the $B(E2\uparrow)$ transition strength between the ground state, with spin and parity $J^{\pi} = 0^{+}$ and the first excited state with spin-parity 2^{+} in the projectile. If the the ^{197}Au target was used, the cross section for the excitation from the $3/2^{+}$ ground state to $7/2^{+}$ excited state the was used to extract the $B(E2\uparrow)$ transition strength. The deduced $B(E2\uparrow)$ transition strengths from ^{197}Au were then compared to the adopted value in order to check the accuracy of the measurement.

The experimental cross section, as given in Eq. 4.1, is determined by the measuring the number of γ rays emitted in the reaction of interest, the number of projectiles which can cause the reaction and the density of the target.

4.1.1 The Live-time of the S800 Particle-Singles and the Gamma-Particle Coincidence Triggers

The experimental cross section measured in intermediate-energy Coulomb excitation is given by:

$$\sigma_{2^{+}\rightarrow 0^{+}} = \frac{N_{\gamma}}{N_{B} N_{T}} \tag{4.11}$$

where N_{γ} is the number of γ rays emitted, N_{B} is the number of projectiles incident on the target, and N_{T} is the density of the target (given in Eq. 4.2).

The number of projectiles is given by:

$$N_B = \frac{N_{Si} \cdot DS_{S800}}{LT_{S800}} \tag{4.12}$$

here, N_{Si} is the number of silicon isotopes of interest detected in the S800 focal plane, DS_{S800} is the downscaling factor (discussed in 3.2.1.4) applied to the S800 singles trigger and LT_{S800} is the livetime of the data acquisition for the S800 singles trigger.

A livetime correction is applied to the measured number of events corresponding to a trigger condition to correct for the amount of time the data acquisition system is busy and cannot record events. This correction is calculated by dividing the number of events the data acquisition system recorded by the total number of events meeting the trigger condition recorded by a scaler module, which is not affected if the data acquisition system is busy. The number of triggers recorded by the data acquisition are put into a "trigbit spectrum" in a bin location depending on the trigger. The counts in 0^{th} bin of the spectrum corresponded to the number of S800 singles triggers recorded by the data acquisition and the 1^{st} bin corresponded to the number of particle-γ coincidence triggers recorded by the data acquisition. The calculation of the livetime of the S800 singles trigger is given below:

$$LT_{s800} = \frac{N_{TB0}}{N_{s800.trigger}} \ , \tag{4.13}$$

where N_{TB0} is the number of counts in the 0^{th} bin in the trigbit spectrum and $N_{s800.trigger}$ is the number of counts recorded by the scaler module for events meeting the s800 singles trigger condition. The uncertainty of this quantity is statistical.

isotope	N_{TB0}	δN_{TB0}	DS_{S800}	LT_{S800} (%)	LT_{Coinc} (%)
^{34}Si	5,497,850	2345	50	83(1)	72(1)
^{36}Si	3,080,700	1755	50	90(1)	79(1)
^{38}Si	2,864,400	1692	50	92(1)	82(1)
^{40}Si	4,318,700	2780	4	95(1)	90(1)
^{42}Si	360,200	600	1	100(1)	100(2)

Table 4.11: Number of particles, downscaling factors and livetimes of the S800 singles trigger and of the particle-γ coincidence trigger for the intermediate-energy Coulomb excitation experiments discussed in this work.

The livetime of the coincidence trigger is calculated in much the same way:

$$LT_{coinc} = \frac{N_{TB1}}{N_{coinc.trigger}} \ . \tag{4.14}$$

Here, N_{TB1} is the number of counts in bin 1 of the trigbit spectrum and $N_{coinc.trigger}$ is the number of counts recorded by the scaler module for events meeting the particle-γ coincidence trigger condition. The uncertainty of the quantity is also statistical.

The number of particles of interest detected in the S800 focal plane (N_{Si} in Eq. 4.12) were obtained by gating the trigbit spectrum on the particle of interest in the particle identification matrix (see Fig. 4.2) and taking the resulting number of counts in the 0^{th} bin of the spectrum. The uncertainty on this number is also statistical. The downscaling factors and livetimes of the S800 singles trigger and particle-γ coincidence trigger, together with the associated uncertainties, for the measurements discussed in this work are given in Tab. 4.11.

The number of γ rays emitted (N_γ in Eq. 4.1) in the de-excitation of an excited state

produced in an inelastic reaction between the projectile and target is:

$$N_\gamma = \frac{N_\gamma^{obs}}{\epsilon(Egamma) \cdot LT_{Coinc}} \ . \tag{4.15}$$

Here, N_γ^{obs} is the number of γ rays detected, ϵ the efficiency of the detector, and LT_{Coinc} is the livetime of the data acquisition for the particle-γ coincidence trigger. The livetimes of the coincidence trigger for the intermediate-energy Coulomb excitation experiments discussed in this work are given in Tab. 4.11. As discussed in the previous section, the number γ rays emitted by the de-excitation of the excited states produced due to the inelastic reaction between the projectile and the target is extracted by fitting the measured γ ray spectra with a function describing the prompt background and the simulated full-energy spectra of the γ rays of emitted. The number of γ rays emitted is then the number simulated (which was constant, at $N_\gamma^{sim} = 100,000$ events), for each of the full-energy spectra simulated multiplied by the fit parameter (p_i). The number extracted from this procedure is the efficiency-corrected number of γ rays emitted:

$$N_\gamma^{sim} = p_i \cdot N_{evts}^{sim} \ . \tag{4.16}$$

The total number of γ rays emitted is obtained by dividing N_γ^{sim} by the livetime of the particle-γ coincidence trigger:

$$N_\gamma = \frac{N_\gamma^{sim}}{LT_{coinc}} \ . \tag{4.17}$$

Therefore, the experimental cross section for intermediate-energy Coulomb excitation is given by (see Eq. 4.1):

$$\sigma_{2^+ \rightarrow 0^+} = \frac{N_\gamma^{sim}}{LT_{coinc}} \cdot \frac{LT_{S800}}{N_{TB} \cdot DS_{S800}} \cdot \frac{1}{N_T} \ . \tag{4.18}$$

isotope	$\sigma^{Si}_{2^+\rightarrow 0^+}$ (mb)	$\sigma^{Au}_{2^+\rightarrow 0^+}$	$\theta_{lab} \leq \theta^{max}_{lab}$ (mrad)
^{34}Si	23(3)	33(2)	46(2)
^{36}Si	52(3)	32(2)	43(2)
^{38}Si	60(3)	32(2)	39(2)
^{40}Si	66(4)	30(3)	37(2)
^{42}Si	112(28)		39(2)

Table 4.12: Measured cross sections obtained following the procedure discussed in the text for the intermediate-energy Coulomb excitation of $^{34-42}$Si.

The measured cross sections for the intermediate-energy Coulomb excitation of $^{34-42}$Si were extracted from of γ ray spectra analyzed subject to the condition of the safe scattering angle, following the procedure discussed in the next section.

4.1.2 Scattering Angle Cuts

As discussed in Sec. 2.2.3, in order to exclude nuclear contributions to the excitation process, the analysis is restricted to events at small scattering angles corresponding to impact parameters 2 fm larger than the sum of the radii of the projectile and the target. To accomplish this, the γ ray spectra measured in the intermediate-energy Coulomb excitation experiments discussed in this work were analyzed subject to gate conditions of several different scattering angle ranges. The accuracy of the reconstructed scattering angle in laboratory frame is assumed to be 2 mrad (0.12°) [55]. The uncertainty in the reconstruction was included in the deduction of the $B(E2\uparrow)$ values by assigning an uncertainty to the angle-integrated cross section for intermediate-energy Coulomb excitation calculated following the theory of Alder and Winther (see Sec. 2.30 and [40]) corresponding to the values of the angle-integrated cross section at calculated with $\theta^{max}_{lab} \pm 2$ mrad in the laboratory frame.

The number of γ rays emitted by events scattering with an angle $\theta \leq \theta^{max}$ was extracted

by fitting the γ ray spectra analyzed subject to the gate conditions of the scattering angle cuts (in addition to the gate conditions previously discussed). The γ-ray yield was extracted following the procedure outlined in Sec. 4.0.6. A representative sampling of the γ-ray spectra analyzed with a Doppler correction applied and subject to the gate conditions discussed in this section and in the previous sections is shown in Fig. 4.22 for the intermediate-energy Coulomb excitation of $^{34-40}$Si and in Fig. 4.23 for the intermediate-energy Coulomb excitation of ^{42}Si.

4.1.3 Measured Cross Sections and Extracted $B(E2)$ Values

The number of particles incident on the target and the number of de-excitation γ rays emitted from excited states in the projectiles or from an excited state in the ^{197}Au target were determined following the procedure discussed in the previous sections. The experimental cross sections (equation 4.18) determined for the intermediate-energy Coulomb excitation of the ^{197}Au target by the projectiles are shown as a function of the scattering angle in Fig. 4.24, while the cross sections determined for the intermediate-energy Coulomb excitation of $^{34-42}$Si are shown in Fig. 4.25.

4.2 B(E2) Values

The $B(E2\uparrow)$ excitation strengths were extracted by comparing the theoretical cross section for intermediate-energy Coulomb excitation (discussed in Sec. 2.2.3 and given in Eq. 2.30) to the measured cross section given in Eq. 4.18 and discussed in this chapter. The cross sections extracted in this work for the intermediate-energy Coulomb excitation of ^{197}Au are shown in Fig. 4.26. The deduced $B(E2\uparrow)$ excitation strength for the transition between

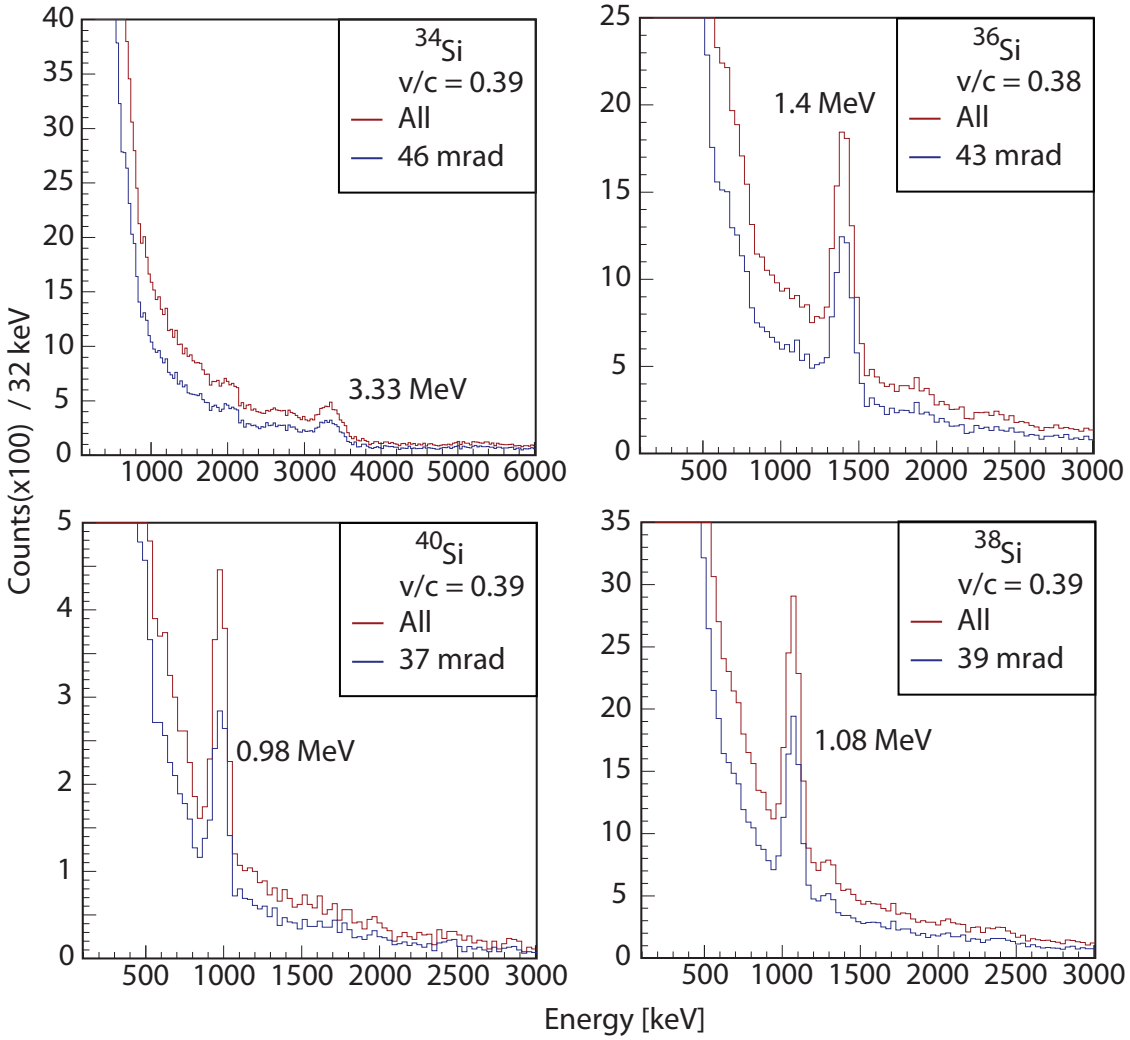

Figure 4.22: Background subtracted γ ray spectra measured in the intermediate-energy Coulomb excitation of $^{34-40}$Si, analyzed with a Doppler correction applied and subject to the two-dimensional time-energy gate condition. The red spectra are analyzed without a scattering angle gate condition, the blue spectra are analyzed subject to the gate condition that the coincident particles have scattering angles between 0 and the safe angle in the laboratory frame. This gate condition reduces the number of measured $2^+ \rightarrow 0^+$ γ rays by $\approx 32\%$ for $^{34-40}$Si, but ensures that there are no nuclear contributions to the excitation cross section.

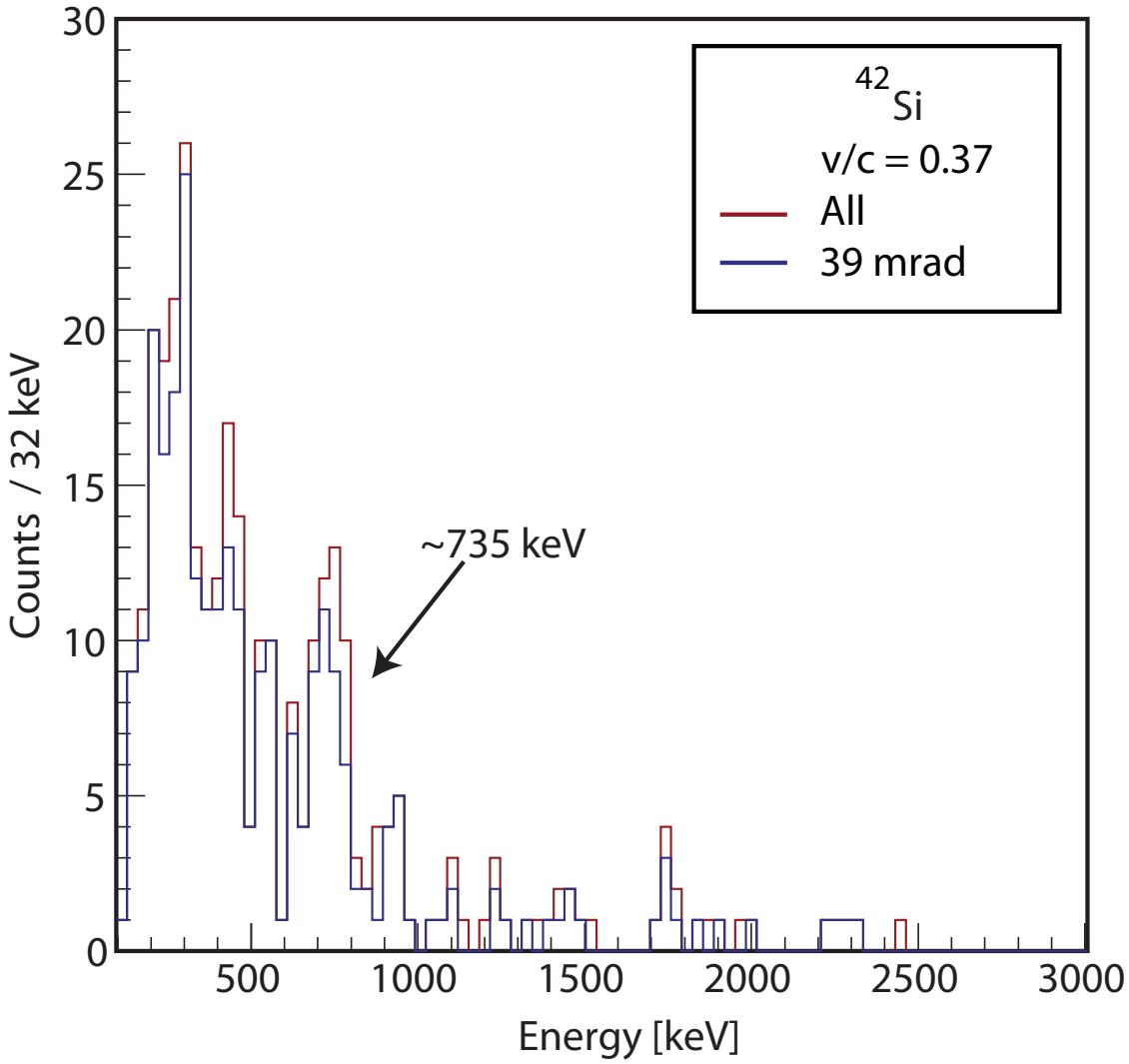

Figure 4.23: The γ ray spectrum measured in the intermediate-energy Coulomb excitation of ^{42}Si, analyzed with a Doppler correction applied and with the two-dimensional time-energy gate condition. The red spectrum is analyzed without a scattering angle gate condition, the blue spectrum is analyzed subject to the gate condition that the coincident particles have scattering angles between 0 and 39 milliradians (which is the safe angle for this case) in the laboratory frame. This gate condition reduces the number of measured $2^+ \rightarrow 0^+$ γ rays by $\approx 20\%$.

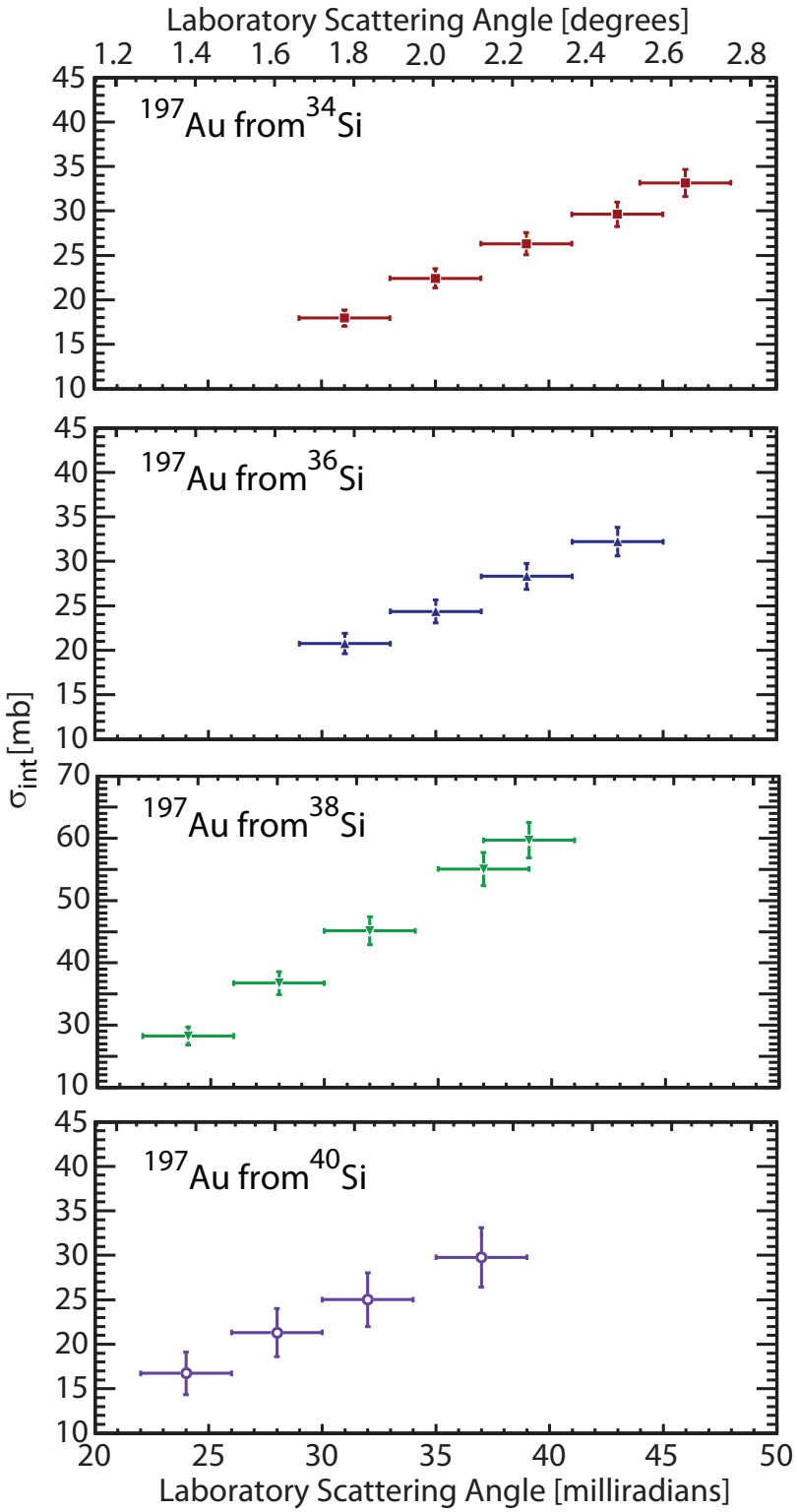

Figure 4.24: Angle-integrated cross sections determined for the intermediate-energy Coulomb excitation of ^{197}Au plotted versus the laboratory scattering angle. The relative uncertainty decreases as a function of the scattering angle due to the increase in statistics.

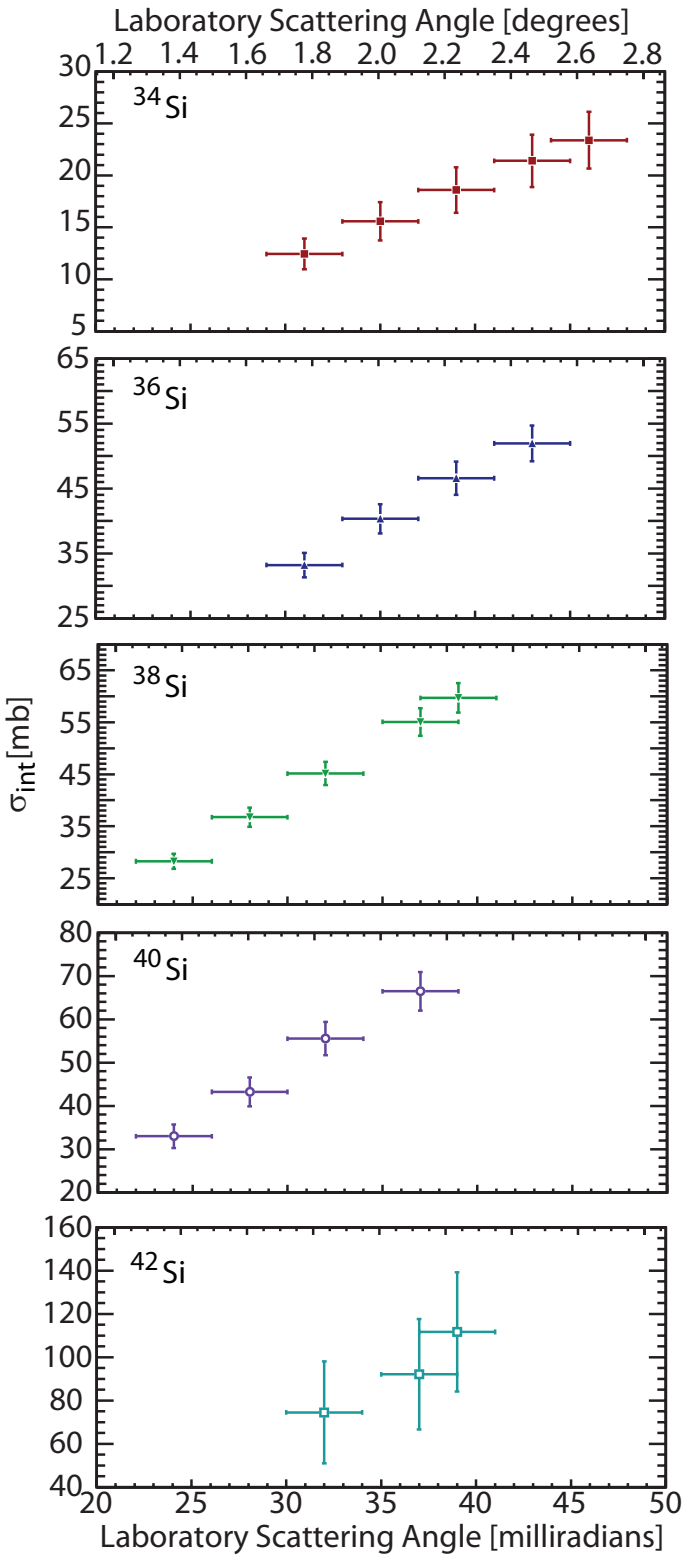

Figure 4.25: Angle-integrated cross sections determined for the intermediate-energy Coulomb excitation of $^{34-42}$Si plotted versus the laboratory scattering angle. The relative uncertainty decreases as a function of the scattering angle due to the increase in statistics.

isotope	^{197}Au $B(E2\uparrow)$ value (e^2 fm^4)
^{34}Si	4150^{+398}_{-386}
^{36}Si	4102^{+423}_{-411}
^{38}Si	4129^{+463}_{-447}
^{40}Si	3899^{+611}_{-599}
Adopted	4494(409)

Table 4.13: $B(E2\uparrow) = B(E2; 3/2^+ \rightarrow 7/2^+)$ values (in units of e^2 fm^4) deduced in this work for the ^{197}Au target used in the intermediate-energy Coulomb excitation of $^{34-42}$Si.

the $3/2^+$ ground state and the $7/2^+$ excited state in ^{197}Au for all of these measurements agrees with the adopted value of $B(E2\uparrow) = 4494(409)$ e^{2}fm^4 [76], as shown in Tab. 4.13. The $B(E2\uparrow)$ excitation strengths deduced following this method are shown as a function of the laboratory scattering angle for $^{34-42}$Si in Fig. 4.27.

The $B(E2; 0^+ \rightarrow 2_1^+)$ transition strength is a property of the structure of the nucleus and cannot depend on the reaction kinematics. However, as seen for ^{197}Au in Fig. 4.26 and for $^{34-40}$Si in Fig. 4.27, there is a correlation between the $B(E2\uparrow)$ value and the scattering angle, possibly due to angle-acceptance losses or beam emittance issues. Nevertheless, the kinematics for the intermediate-energy of the projectile by the target or of the target by the projectile are the same, so this correlation can be removed by normalizing the deduced $B(E2\uparrow)$ value for ^{197}Au on the adopted value:

$$S = \frac{B(E2\uparrow)^{Au}_{exp}}{B(E2\uparrow)^{Au}_{adopted}}. \tag{4.19}$$

The deduced $B(E2)$ value for the silicon isotopes can then be scaled by S:

$$B(E2;\uparrow)^{Si}_{exp.scal} = \frac{B(E2\uparrow)^{Si}_{exp}}{S} \ . \tag{4.20}$$

The scaling factors obtained by normalizing the deduced $B(E2\uparrow)$ value for ^{197}Au on the adopted value are shown in Fig. 4.28. The $B(E2\uparrow)$ value deduced for ^{42}Si was not normalized in this way, because the values shown in Fig. 4.27 do not exhibit a slope. However, if the $B(E2)$ value for ^{42}Si were to be scaled, the result would be a $\simeq 8\%$ increase in the value.

The deduced $B(E2; 0^+ \rightarrow 2^+)$ excitation strengths shown for $^{34-40}$Si in Fig. 4.27 were divided by the scaling factors shown in Fig. 4.28, resulting in the corrected $B(E2; 0^+ \rightarrow 2^+)$ excitations strengths shown in Fig. 4.29. This correction to the $B(E2)$ values deduced for the intermediate-energy Coulomb excitation of $^{34-40}$Si removes the non-physical correlation with the scattering angle and results in values that agree with the previous measurement [17].

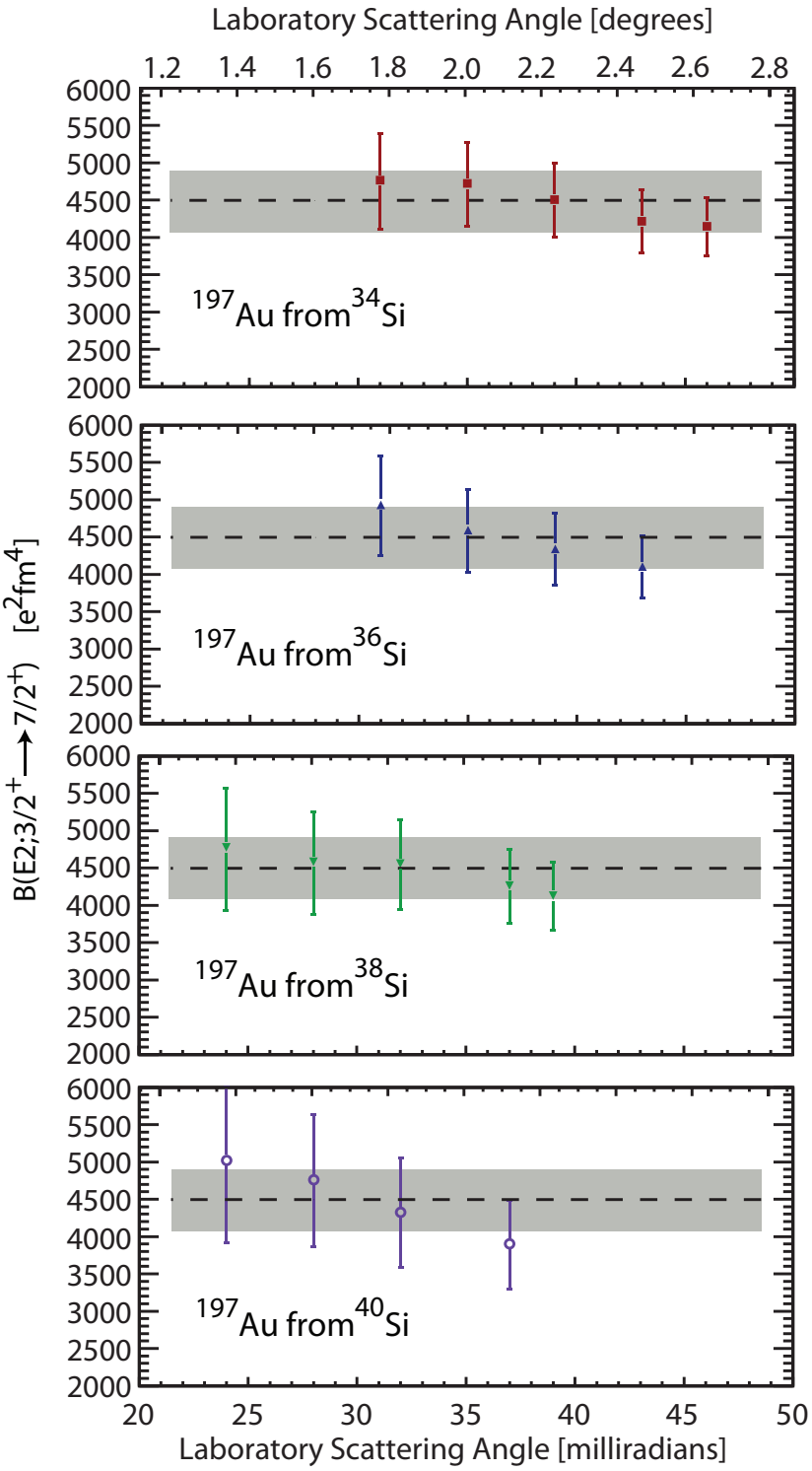

Figure 4.26: $B(E2\uparrow)$ excitation strengths extracted from the measurement of the intermediate-energy Coulomb excitation of ^{197}Au. The adopted value for the $B(E2\uparrow)$ excitation strength is indicated by the gray box.

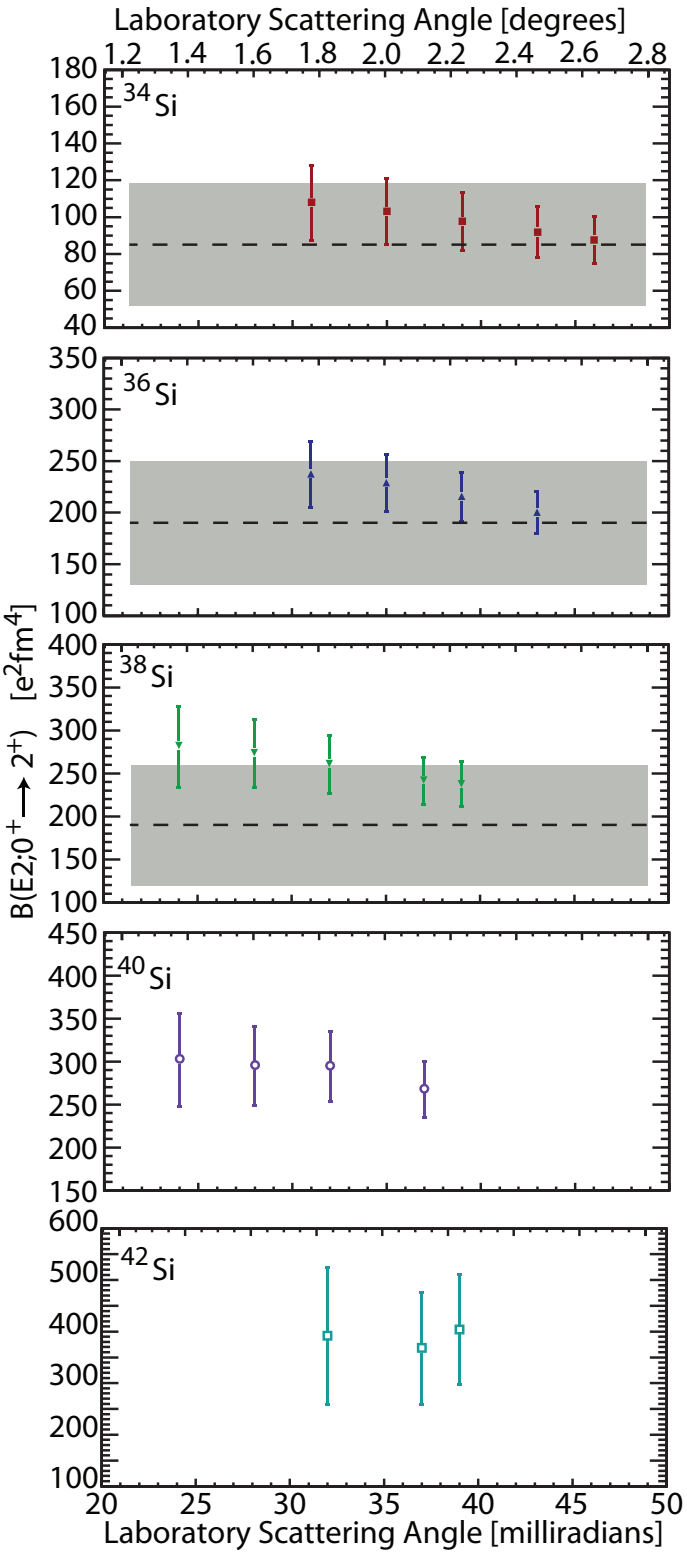

Figure 4.27: $B(E2\uparrow)$ excitation strengths extracted from the measurement of the intermediate-energy Coulomb excitation of $^{34-42}$Si. The adopted value for the $B(E2\uparrow)$ excitation strengths for ^{34,36,38}Si are indicated by the gray boxes.

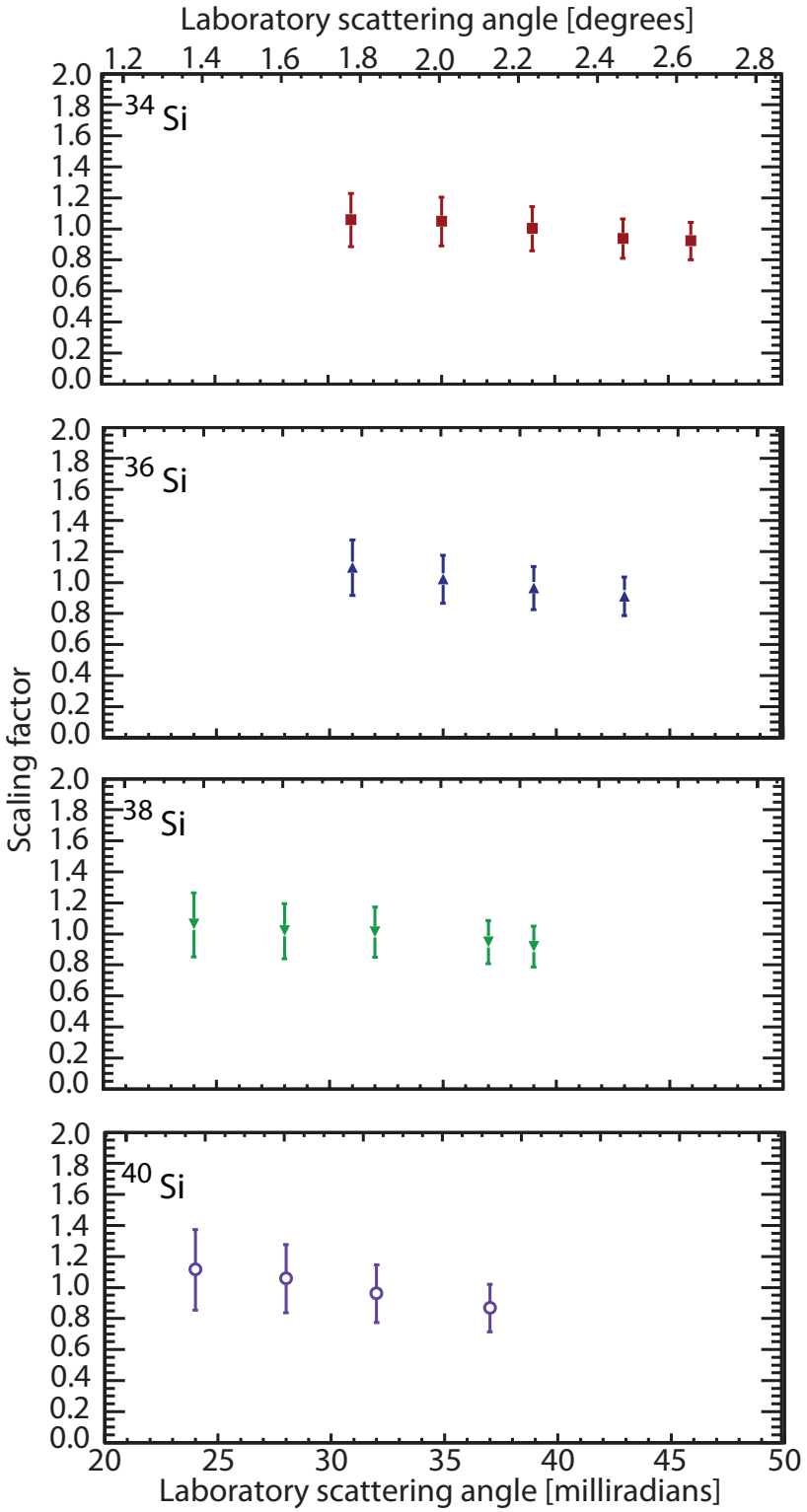

Figure 4.28: Scaling factors plotted as a function of the laboratory scattering angle obtained for the intermediate-energy Coulomb excitation of $^{34-40}$Si by normalizing the deduced $B(E2; 3/2^+ \rightarrow 7/2^+)$ transition strength for the ^{197}Au target on the adopted value.

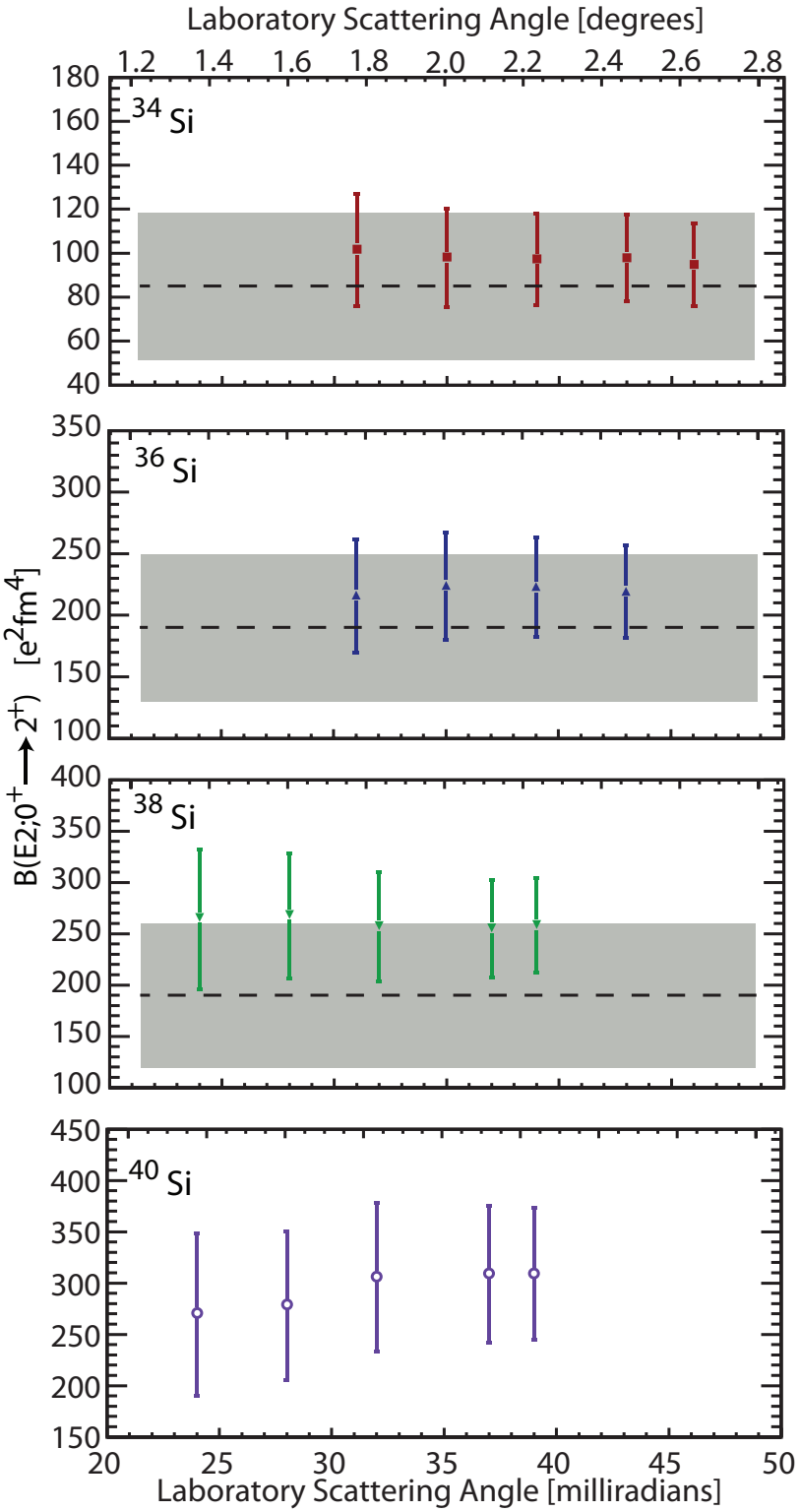

Figure 4.29: Scaled $B(E2\uparrow)$ excitation strengths extracted from the measurement of the intermediate-energy Coulomb excitation of $^{34-40}$Si. The adopted value for the $B(E2\uparrow)$ excitation strengths for ^{34,36,38}Si are indicated by the gray boxes. The scaling of the $B(E2)$ excitation strengths is discussed in the text.

Chapter 5

Results and Summary

The intermediate-energy Coulomb excitation of $^{34-42}$Si was performed in order to determine the strength of the electric quadrupole transition matrix element between the ground state and the first excited state with spin-parity 2^+ for even-even nuclei in this isotopic chain. The intermediate-energy Coulomb excitation of $^{34-40}$Si was performed using a ^{197}Au target, while the intermediate-energy Coulomb excitation of ^{42}Si was performed using a ^{209}Bi target. The de-excitation γ rays were detected in the high-efficiency CAEsium Iodide Scintillator ARray (CAESAR), which was placed around the target, in coincidence with inelastically scattered particles detected in the focal plane of the S800 spectrograph.

The $B(E2; 0^+ \rightarrow 2^+)$ values deduced in this work are given in Tab. 4.12, together with the adopted values for the previously measured silicon isotopes ($^{34-38}$Si) and a theoretical predictions from the effective interactions SDPF-M [11, 12], SDPF-U and SDPF-NR [13], and EPQQM [80]. The effective charges used for the calculation of the $B(E2\uparrow)$ values are given in Tab. 5.3.

The effective interaction SDPF-U proposed by Nowacki and Poves [13] predicts $B(E2\uparrow)$ values best describing the measured results, which cannot entirely exclude the result pre-

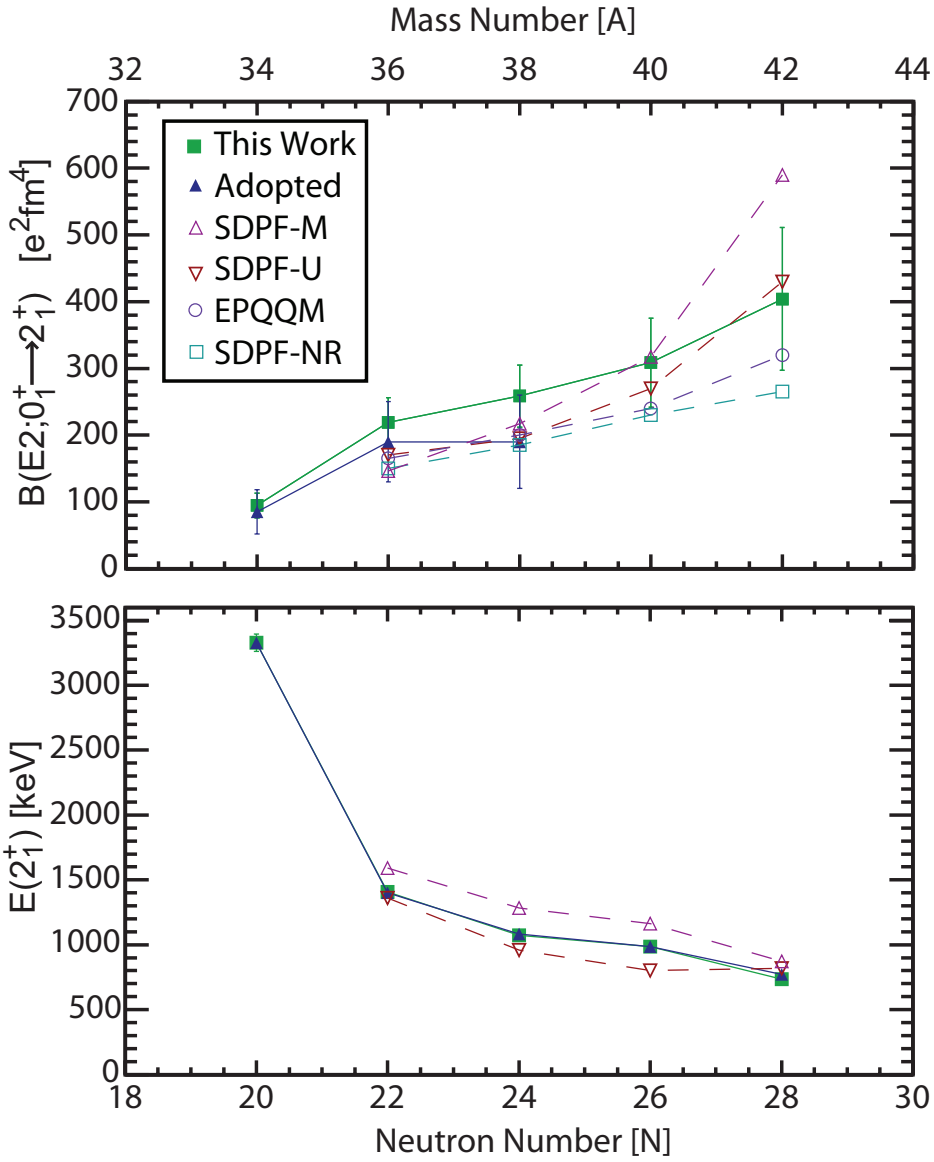

Figure 5.1: Upper panel: the $B(E2\uparrow)$ transition strength for the even-even silicon isotopic chain with $20 \leq N \leq 28$ plotted as a function of the neutron number and compared to several shell model calculations (discussed in text). The collapse of the $N = 28$ shell closure is clearly seen by the large $B(E2\uparrow)$ value for ^{42}Si. Lower panel: the first 2^+ excited state energies for the isotopes in the upper plot. The values measured in this work are compared to the previously measured values and the values predicted by theory (discussed in text).

isotope	this work	adopted	SDPF-U	SDPF-NR	SDPF-M	EPQQM
^{34}Si	95^{+19}_{-18}	85(33)				
^{36}Si	219^{+38}_{-37}	193(59)	170	150	146	165
^{38}Si	259^{+47}_{-46}	193(71)	195	185	217	200
^{40}Si	309^{+67}_{-66}		270	230	317	240
^{42}Si	404(107)		430	265	590	320

Table 5.1: $B(E2\uparrow)$ values (in units of e^2 fm^4) deduced in this work for $^{34-42}$Si compared to the adopted values (from the previous intermediate-energy Coulomb excitation measurement performed by Ibbotson *et al.*[17]) and theoretical calculations (discussed in text).

isotope	this work	adopted	SDPF-U	SDPF-M
^{34}Si	3328(106)	3327.5(5)		
^{36}Si	1406(14)	1399(25)	1360	1590
^{38}Si	1074(14)	1084(20)	960	1285
^{40}Si	986(10)	986(5)	800	1162
^{42}Si	735(40)	770(19)	820	872

Table 5.2: First 2^+ excited state energy measured in this work for $^{34-42}$Si are compared to adopted values [17, 21] and to theoretical calculations (discussed in text).

dicted by the EPQQM effective interaction [13]. The predictions of the SPDF-M and SPDF-NR effective interactions of the $B(E2\uparrow)$ value of ^{42}Si are too high and too low, respectively.

More work is needed to completely understand the mechanisms driving the changes in structure in this region. Two experiments have been proposed and accepted at NSCL to study the structure of the silicon isotopic chain, one to study the single-particle structure

model	e_π	e_ν
SDPF-U	1.35	0.35
SDPF-NR	1.35	0.35
EPQQM	1.15	0.15
SDPF-M	1.2	0.45

Table 5.3: Effective charges used in the shell model calculations discussed in text.

of $^{36-40}$Si [78] and one to extract the deformation parameter of ^{42}Si via proton inelastic scattering [79]. The results from the latter experiment, together with the $B(E2)$ values deduced in this work, and the results of the previous proton inelastic scattering measurement [18, 19, 20] can be used to extract the contribution of the protons and neutrons to the deformation in this isotopic chain out to ^{42}Si.

The cross sections for intermediate-energy Coulomb excitation of $^{34-42}$Si were measured and the $B(E2; 0^+_{g.s.} \rightarrow 2^+_1)$ values for these nuclei were deduced. This measurement comprises the first quantification of the electric quadrupole collectivity of ^{40,42}Si and provides a coherant picture of the evolution of the quadrupole collectivity between the conventionally magic neutron numbers of $N = 20$ and $N = 28$ along the $Z = 14$ sub-shell gap, showing that the $N = 28$ shell closure collapses for $Z = 14$.

BIBLIOGRAPHY

BIBLIOGRAPHY

[1] "Isotope Science Facility at Michigan State University, Upgrade of the NSCL rare isotope research capabilities", White paper, Michigan State University, East Lansing, MI, 2006.

[2] B. A. Brown, *Lecture Notes in Nuclear Structure Physics*, Lecture Notes, National Superconducting Cyclotron Laboratory and Michigan State University, East Lansing, MI. (2009).

[3] R. F. Casten, *Nuclear Structure from a Simple Perspective*, (Oxford Science Publications, 1999, 2nd edition).

[4] M. G. Mayer, *Phys. Rev.* **74**, 235 (1948).

[5] O. Haxel, J. H. D. Jensen and H. E. Suess *Phys. Rev.* **75**, 1766 (1949).

[6] B. A. Brown, *Progress in Particle and Nuclear Physics* **47**, 517 (2001).

[7] D.-C. Dinca, R. V. F. Janssens, A. Gade, D. Bazin, R. Broda, B. A. Brown, C. M. Campbell, M. P. Carpenter, P. Chowdhury, J. M. Cook, A. N. Deacon, B. Fornal, S. J. Freeman, T .Glasmacher, M .Honma, F. G. Kondev, J.-L. Lecouey, S. N. Liddick, P. F. Mantica, W. F. Mueller, H. Olliver, T. Otsuka, J. R. Terry, B. A. Tomlin, and K. Yoneda *Phys.Rev.* **C71**, 041302 (2005).

[8] T. Otsuka, R. Fujimoto, Y. Utsuno, B. A. Brown, M. Honma, and T. Mizusaki, *Phys. Rev. Lett.* **87**, 082502 (2001).

[9] T. Otsuka, T. Suzuki, R. Fujimoto, H. Grawe, and Y. Akaishi *Phys. Rev. Lett.* **95**, 232502 (2005).

[10] Y. Utsuno, T. Otsuka, T. Mizusaki and M. Honma *Phys. Rev. C* **60** 054315 (1999).

[11] Y. Utsuno *private communication* (2010).

[12] Y. Utsuno, "Shell Evolution of Exotic Nuclei Beyond N=28 Described by the Universal Monopole Picture.", Perspectives on the Modern Shell Model and Related Experimental Topics, National Superconducting Cyclotron Laboratory. Michigan State University, Lansing, MI. 5 Feb. 2010.

[13] F. Nowacki and A. Poves, *Phys. Rev. C* **79**, 014310 (2009).

[14] National Nuclear Data Center, Brookhaven National Lab, 2011. `http://www.nndc.bnl.gov`

[15] S. Raman, C.W. Nestor Jr., P. Tikkanen *Atomic Data and Nucl. Data Tables* **78**, 1 (2001).

[16] B. Pritychenko, J. Choquette, M. Horoi, B. Karamy, and B. Singh *arXiv:1102.3365v1* **nucl-th** (2011).

[17] R. W. Ibbotson, T. Glasmacher, B. A. Brown, L. Chen, M. J. Chromik, P.D. Cottle, M. Fauerbach, K. W. Kemper, D. J. Morrissey, H. Scheit, and M. Thoennessen, *Phys. Rev. Lett.* **80**, 2081 (1998).

[18] C. M. Campbell, Quadrupole collectivity measurements in even-even, neutron-rich silicon and sulfur isotopes approaching N = 28, Ph.D. dissertation, Michigan State University, East Lansing, MI, 2007.

[19] C. M. Campbell, N. Aoi, D. Bazin, M. D. Bowen, B. A. Brown, J. M. Cook, D.-C. Dinca, A. Gade, T. Glasmacher, M. Horoi, S. Kanno, T. Motobayashi, W. F. Mueller, H. Sakurai, K. Starosta, H. Suzuki, S. Takeuchi, J. R. Terry, K. Yoneda, and H. Zwahlen, *Phys. Rev. Lett.* **97**, 112501 (2006).

[20] C. M. Campbell, N. Aoi, D. Bazin, M. D. Bowen, b, B. A. Brown, J. M. Cook, D.-C. Dinca, A. Gade, T. Glasmacher, M. Horoi, S. Kanno, T. Motobayashi, L. A. Riley, H. Sagawa, H. Sakurai, K. Starosta, H. Suzuki, S. Takeuchi, J. R. Terry, K. Yoneda, and H. Zwahlen, *Phys. Lett.* **B652**, 169 (2007).

[21] B. Bastin, S. Grèvy, D. Sohler, O. Sorlin, Zs. Dombrádi, N. L. Achouri, J. C. Angélique, F. Azaiez, D. Baiborodin, R. Borcea, C. Bourgeois, A. Buta, A. Bürger, R. Chapman, J. C. Dalouzy, Z. Dlouhy, A. Drouard, Z. Elekes, S. Franchoo, S. Iacob, B. Laurent, M. Lazar, X. Liang, E. Liénard, J. Mrazek, L. Nalpas, F. Negoita, N. A. Orr, Y. Penionzhkevich, Zs. Podolyák, F. Pougheon, P. Roussel-Chomaz, M. G. Saint-Laurent, M. Stanoiu, and I. Stefan, and F. Nowacki, and A. Poves, *Phys. Rev. Lett.* **99**, 022503 (2007).

[22] J. Fridmann, I. Wiedenhöver, A. Gade, L. T. Baby, D. Bazin, B. A. Brown, C. M. Campbell, J. M. Cook, P. D. Cottle, E. Diffenderfer, D.-C. Dinca, T. Glasmacher, P. G. Hansen, K. W. Kemper, J. L. Lecouey, W. F. Mueller, H. Olliver, E. Rodriguez-Vieitez, J. R. Terry, J. A. Tostevin and K. Yoneda, *Nature* (London) **435**, 922 (2005).

[23] J. Fridmann, I. Wiedenhöver, A. Gade, L. T. Baby, D. Bazin, B. A. Brown, C. M. Campbell, J. M. Cook, P. D. Cottle, E. Diffenderfer, D.-C. Dinca, T. Glasmacher, P. G. Hansen, K. W. Kemper, J. L. Lecouey, W. F. Mueller, E. Rodriguez-Vieitez, J. R. Terry, J. A. Tostevin, K. Yoneda, and H. Zwahlen, *Phys. Rev. C* **74**, 034313 (2006).

[24] B. A. Brown and B. H. Wildenthal *Phys. Rev.* **C21** 2107 (1980).

[25] K. Krane, "Introductory Nuclear Physics", (John Wiley and Sons, 1988).

[26] P. J. Voss, "Recoil Distance Method Lifetime Measurements Via Gamma-Ray and Charged Particle Spectrscopy at NSCL, Ph.D. dissertation, Michigan State University, East Lansing, MI, 2011.

[27] A. M. Bernstein, V. R. Brown, and V. A. Madsen, *Phys. Lett.* **103B** (1981).

[28] P. D. Cottle, *Nuclear Physics* **A682** 124c-130c (2001).

[29] A. Bohr and B. R. Mottelson, *Nuclear Structure, Volumes 1 and 2*, (World Scientific, 1998).

[30] P. Ring and P. Schuck, *The Nuclear Many-Body Problem* (Springer-Verlag, 1980).

[31] S. Raman, C. H. Malarkey, W. T. Milner, C. W. Nestor, JR. and P. H. Stelson *Atomic Data and Nucl. Data Tables* **36**, 1 (1987).

[32] I. J. Thompson and F. M. Nunes, *Nuclear Reactions for Astrophysics: Princlpes, Calculation and Applications of Low-Energy Reactions*, (Cambridge University Press 2009).

[33] P. E. Hodgson, *Nuclear Reactions and Nuclear Structure* (Clarendon Press, Oxford 1971).

[34] A. J. Koning and J. P. Delaroche, *Nuclear Physics* **A713**, 231 (2003).

[35] I. Thompson, Computer Code FRESCO, `http://www.fresco.org.uk`

[36] J. Raynal *Notes on ECIS94*, (Note CEA-N-2772 1994).

[37] J. Raynal, Computer Code ECIS97, unpublished.

[38] T. Glasmacher, *Ann. Rev. Nucl. Part. Sci.* **48** 1 (1998).

[39] A. N. F. Aleixo and C. A. Bertulani *Nucl. Phys.* **A505** 448 (1989).

[40] A. Winther and K. Alder, *Nuclear Physics* **A319**, 518 (1979).

[41] H. Scheit,"Low-Lying Collective Excitations in Neutron-Rich Even-Even Sulfur and Argon Isotopes Studied via Intermediate-Energy Coulomb Excitation and Proton Scattering, Ph.D. dissertation, Michigan State University, East Lansing, MI, 2007.

[42] H. Esbensen *Phys. Rev. C* **78**, 024608 (2008).

[43] A. Gade, D. Bazin, C. M. Campbell, J. A. Church, D. C. Dinca, J. Enders, T. Glasmacher, Z. Hu, K. W. Kemper, W. F. Mueller, H. Olliver, B. C. Perry, L. A. Riley, B. T. Roeder, B. M. Sherrill, and J. R. Terry, *Phys.Rev.* **C68**, 014302 (2003).

[44] E. Warburton, J. Becker and B. A. Brown *Phys. Rev. C* **41**, 1147 (1990).

[45] C. A. Bertulani, G. Cardella, M. De Napoli, G. Raciti, and E. Rapisarda, *Phys. Lett.* **B650** 233 (2007).

[46] Heiko Scheit, Alexandra Gade, Thomas Glasmacher, and Tohru Motobayashi, *Phys. Lett.* **B659** 515 (2008).

[47] R. Kumar, R. Kharab, and H. C. Sharma, *Chin. Phys. Lett.* **27** 032502 (2010).

[48] J. M. Cook, T. Glasmacher and A. Gade, *Phys. Rev. C.* **73**, 024315 (2006).

[49] H. Geissel and G. Münzenberg *Ann. Rev. Nucl. Part. Sci.* **45** 164 (1995).

[50] D. J. Morrissey *Nucl. Phys.* **A616** 45 (1997).

[51] D. J. Morrissey and NSCL staff *Nucl. Instrum. Meth.* **B126** 316 (1997).

[52] D.J. Morrissey, B.M. Sherrill, M. Steiner, A. Stolz and I. Wiedenhöver *Nucl. Instrum. Meth.* **B204** 90 (2003).

[53] D. Bazin, J. A. Caggiano, B. M. Sherrill, J. Yurkon and A. Zeller *Nucl. Instr. Meth.* **B204** 629 (2003).

[54] D. Weisshaar, A. Gade, T. Glasmacher, G.F. Grinyer, D. Bazin, P. Adrich, T. Baugher, J.M. Cook, C. Aa. Diget, S. McDaniel, A. Ratkiewicz, K.P. Siwek and K.A. Walsh *Nucl. Instr. Meth.* **A624** 615 (2010).

[55] J. Yurkon, D. Bazin, W. Benenson, D. J. Morrissey, B. M. Sherrill, D. Swan and R. Swanson *Nucl. Instr. Meth.* **A422** 291 (1999).

[56] O. B. Tarasov and D. Bazin, *Nucl. Instr. Meth.* **B266**, 4657 (2008).

[57] T. Ginter *A1900 Fragment Separator and High-Energy Beamline Service Level Description* NSCL internal document, (2007).

[58] G. F. Knoll *Radiation Detection and Measurement* (John Wiley & Sons, 2000).

[59] C. Guess *private communication* 2009.

[60] D. Bazin *S800 Spectrometer Service Level Description* NSCL internal document, 2007.

[61] S. McDaniel *private communication* 2011.

[62] J. Caggiano, "Spectroscopy of Exotic Nuclei with the S800 Spectrograph", Ph.D. dissertation, Michigan State University, East Lansing, MI, 1999.

[63] M. Berz, K. Joh, J. A. Nolen, B. M. Sherrill and A. Zeller *Phys. Rev.* **C47** 537 (1993).

[64] R. D. Evans *The Atomic Nucleus* (McGraw-Hill, Inc., 1972, 14th ed.).

[65] H. J. Wollersheim *et al. Nucl. Instr. Meth.* **A537** 637 (2005).

[66] W. R. Leo *Techniques for Nuclear and Particle Physics Experiments: A How-to Approach* (Springer-Verlag, 1994, 2nd Ed).

[67] W. F. Mueller, J. A. Church, T. Glasmacher, D. Gutknecht, G. Hackman, P.G. Hansen, Z. Hu, K. L. Miller, and P. Quirin, *Nucl. Instr. Meth.* **A466** 492 (2001).

[68] S. Agostinelli and the GEANT4 Collaboration *Nucl. Instr. Meth.* **A506** 250 (2003).

[69] H. Zwahlen,"Angular Distributions of Gamma Rays with Intermediate-Energy Beams and Spectroscopy of ^{32}Mg", Ph.D. dissertation, Michigan State University, East Lansing, MI, 2005.

[70] T. Baugher *et al.*, to be published.

[71] W. Kratschmer, H. V. Klapdor, and E. Grosse *Nuclear Physics*, **A201** 179, (1973).

[72] L. A. Riley, P. Adrich, T. Baugher, D. Bazin, B. A. Brown, J. M. Cook, P. D. Cottle, C. Aa. Diget, A. Gade, D. Garland, T. Glasmacher, K. Hosier, K. W. Kemper, T. Otsuka, W. D. M. Rae, A. Ratkiewicz, K. P. Siwek, J. A. Tostevin, Y. Utsuno, and D. Weisshaar *Phys. Rev.* **C78**, 011303(R) (2008)

[73] L. A. Riley, P. Adrich, T. Baugher, D. Bazin, B. A. Brown, J. M. Cook, P. D. Cottle, C. Aa. Diget, A. Gade, D. A. Garland, T. Glasmacher, K. E. Hosier, K. W. Kemper, A. Ratkiewicz, K. P. Siwek, J. A. Tostevin, and D. Weisshaar *Phys. Rev.* **C80**, 037305 (2009)

[74] K. L. Miller, "Nuclear Structure Near N=Z=28: Study of Neutron-Deficient Nickle Isotopes via One-Neutron Knockout and Intermediate-Energy Coulomb Excitation" Ph.D. dissertation, Michigan State University, East Lansing, MI, 2003.

[75] H. Olliver, T. Glasmacher and A. E. Stuchberry *Phys. Rev.* **C68** 044312 (2003).

[76] H. Xiaolong and Z. Chunmei *Nuclear Data Sheets* **104**, 283 (2005). Data extracted from the ENSDF database version of June 7, 2011.

[77] C. Zhou, *Nucl. Data Sheets* **76**, 399 (1995).

[78] R. Stroberg *et. al Single-Particle Structure of Neutron-Rich Si Isotopes*, unpublished.

[79] L. Riley *et. al Collective excitations in the vicinity of Z = 14*, unpublished.

[80] K. Kaneko, Y. Sun, T. Mizusaki and M. Hasegawa *Phys. Rev. C83*, 014320 (2011).